# Radiation Induces Prompt Live-Cell Metabolic Fluxes: an In-Vitro Demonstration

by

David Daniel Campos

A dissertation submitted in partial fulfillment of
the requirements for the degree of

Doctor of Philosophy

(Medical Physics)

at the

University of Wisconsin-Madison

2017

Date of final oral examination: 5/2/17

This dissertation is approved by the following members of the Final Oral Committee:
Michael W. Kissick, Assistant Professor, Medical Physics
Bryan P. Bednarz, Associate Professor, Medical Physics
Kevin W. Eliceiri, Senior Scientist, Biomedical Engineering and Medical Physics
Edward F. Jackson, Professor, Medical Physics
Randall J. Kimple, Assistant Professor, Human Oncology

© David Daniel Campos 2017

All Rights Reserved

# Acknowledgements

I would like to dedicate this work to everybody that has helped me to reach this point along the way. From an early age, my parents Daniel and Margaret instilled in me the value of curiosity and a thirst for knowledge that laid the foundation for my drive to be a scientist. Their high level of academic and professional achievement served as inspiration for the success I've enjoyed in my academic career. It has been particularly gratifying to forge a career path in medical physics that is a sort of marriage between the careers that my parents chose to pursue.

My research at the University of Wisconsin has been filled with challenges to overcome and triumphs to savor. I want to thank my advisor, Dr. Michael Kissick for bringing me into the Medical Physics department at UW. We started off with common ground having both done work in plasma physics, albeit for very different applications. The relentlessly positive attitude Michael displayed was extremely helpful during the challenging parts of getting this work off the ground. I don't think either of us ever envisioned moving so far away from so-called "traditional" medical physics and delving into the realm of radiobiology; however, we both believe that the future of radiation therapy lies here. Being on the frontier of new knowledge has been intellectually challenging and immensely gratifying.

I'd also like to thank the great scientists at LOCI who helped introduce me to the complexities of biological systems. In particular, I'd like to thank Dr. Kevin Eliceiri, who allowed me to use the facilities at LOCI to explore changes in cellular metabolism, but also borrowed from the Rock Mackie school of wisdom and encouraged me to ask for forgiveness rather than permission (within reason) when it came to trying new experiments, or searching for new veins of experimental knowledge to mine. Drs Pam Young (Go Hoosiers!) and Brian

Burkel were also instrumental in this project because they showed me the principles to obtain and analyze lifetime images, but took care to let me develop my own methods.

Finally, and most importantly, I'd like to thank my wife Julia for her patience during this journey. My academic career has taken us inexorably northward into colder and more bitter winters. Her love and support during the struggles of finding my own research path was immeasurably helpful and necessary. Julz, thank you for sticking it out as the winters and the feet of snow have piled up; hopefully, California will be more to your liking.

# Abstract

Radiation therapy is a very important component of cancer treatments. Considerable advancements in radiotherapy technology have allowed for more uniform dose distributions, as well as improved the ability to avoid organs at risk. These important innovations have led to reductions in normal tissue toxicities resultant from treatments. While improved dose-delivery methods have allowed for dose-boosting and spatial dose-painting, these improvements do not address the fundamental biological impact that radiation creates through the creation of free radicals and reactive oxygen species. This dissertation aims to quantify prompt changes in metabolic signature and to investigate HIF-1 signaling following radiation on the cellular level *in vitro*. Moreover, we evaluate changes in mitochondrial behavior in response to radiation *in vitro.* An understanding of how metabolic fluxes may create interplay between radiation therapy and radiosensitivity may improve cancer treatment efficacy in the future.

For this study, metabolic fluxes in two cell lines, a cancerous urothelial carcinoma cell line (T24) and a comparable normal cell line, Normal Oral Keratinocytes (NOK) were assessed by fluorescence lifetime imaging microscopy (FLIM) of the reduced form of Nicotinamide Adenosine Dinucleotide (NADH). Using FLIM we demonstrated that the cancerous T24 cells showed a strong shift in metabolic signature toward free NADH following irradiation of 10 Gy. In contrast, no such shift in metabolic signature was observed for NOK cells following irradiation. These changes occurred within 30 minutes, which is well ahead of the time-frame of any cell-death related changes. Free NADH is created when glucose is cleaved into pyruvate in the process of glycolysis. During oxidative phosphorylation (oxphos), NADH is bound to the electron transport chain (ETC) and oxidized. This shift toward free NADH in the cancer cells is evidence for increased aerobic glycolysis.

To link changes in metabolism with the local tumor microenvironment, we also assessed expression of transcription factor subunit HIF-1α via immunofluorescence staining for both cell lines. The HIF-1 complex serves as a transcription factor for several processes including glucose transport enzymes, glycolytic enzymes, and stimulates angiogenesis and erythropoiesis. It was found that following irradiation the T24 showed a three-fold increase in HIF-1α expression. However, in the case of the NOK cells, HIF-1α expression was actually found to slightly decrease by about 35%. Clonogenic survival assays found that T24 cells are approximately 100 times more radioresistant than NOK cells for high dose (>8 Gy) assays.

Because cellular mitochondria play a major role in cellular metabolism through oxidative phosphorylation (oxphos) and oxphos-generated reactive oxygen species (ROS), we quantified cellular ROS and mitochondrial membrane polarization (MMP) in each cell line following irradiation. ROS measurements were conducted using DCFDA (dichlorofluorescein diacetate) dye which reacts with peroxyl radicals in solution to activate its fluorescent potential. MMP measurements were conducted using TMRE (tetramethylrhodamine ester) dye. TMRE dye is sequestered by polarized mitochondria; however, in cells with depolarized mitochondria the TMRE dye is washed away. ROS levels were significantly heightened following irradiation in NOK cells, whereas for T24 cells ROS levels remained almost constant. MMP levels also slightly decreased following irradiation but remained above mitochondrial control levels. In contrast, T24 cells' MMP remained constant at mitochondrial control levels for both irradiation and no irradiation. These data indicate that NOK mitochondria are producing potentially cytotoxic ROS following irradiation not present in the T24 cells.

Because of the potential link between HIF-1, radioprotection and metabolism, expression of Hexokinase II (HK-II), a transcription target of HIF-1, was quantified using the Western Blot gel electrophoresis technique. Hexokinase is a unique isoform of the glycolytic, hexokinase family and is mediated by the HIF-1 complex. HK-II has been found to be over expressed in many cancer types. It was found that T24 cells had a higher concentration of HK-II than NOK cells. HKII has been demonstrated to have significant cellular protective effects against apoptotic and necrotic cell death as well as damage to organelles from ROS.

Together, these data indicate that following irradiation T24 cells have a capacity to increase levels of glycolysis as compared to NOK cells. We hypothesize that this capability may be driven by T24 cells' expression of HIF-1 to transcribe HK-II which has the highest capacity for glucose throughput. These metabolic fluxes resulting from radiation likely drive the interplay between radiation and radiosensitivity; moreover, these data show that the timescale of these fluxes may take place *during* a hypofraction. A thorough understanding of how these effects manifest in different cancer types as well as in higher order systems may unlock a new potential avenue for steering adaptive radiation therapy treatment.

# Table of Contents

## Chapter 4: Radiation affects cancer cell metabolism via ROS production and interaction with mitochondria *in vitro* ... 85

# List of Figures and Tables

# Chapter 1: Introduction and Specific Aims

## 1.1 Introduction

Radiation therapy is a key component in most therapeutic regimens for cancer. Oftentimes, radiation is deployed in tandem with surgery and systemic therapies. Radiation induces the creation of a large population of free radicals and reactive oxygen species which cause single-strand and double-strand breaks in deoxyribonucleic acid (DNA) molecules. However, radiation also induces changes in the tumor microenvironment such as changes in cell signaling, extracellular matrix, and metabolism. It is widely-known that oxygen concentration, which is affected by metabolism, plays a key role in radiosensitivity, and also affects cellular transcription factor hypoxia-inducible factor 1 (HIF-1). Among a multitude of functions, HIF-1 regulates glucose transporters, glycolytic enzymes downstream which are key players in metabolism. By developing a deeper understanding of how radiation impacts the tumor microenvironment fundamentally, deployment of radiation therapy may be improved to be adaptive and more patient specific.

## 1.2 Central hypothesis and specific aims

**Our central hypothesis is that radiation may affect the tumor microenvironment in a quantifiable manner through changes in metabolism mediated by the expression of proteins related to the metabolic cascade.** Our rationale is that previous studies have demonstrated that radiation perturbs oxygenation and perfusion in tumor models, and changes in oxygenation should have significant impacts on metabolism as well as radiosensitivity. Because radiation itself may impact radiosensitivity through metabolic reprogramming, it is important to gain a deeper mechanistic understanding of how these changes manifest themselves.

**Specific Aim 1: to quantify prompt changes in metabolic signature and to investigate HIF-1 signaling following radiation on the cellular level *in vitro.*** To quantify changes in metabolism following radiation fluorescence lifetime imaging microscopy of cellular NADH were used in a radiosensitive cell line versus a comparatively radioresistant cell line. Furthermore, quantification of HIF-1α expression and cellular oxygen consumption helped shed light on the nature of these metabolic changes.

**Specific Aim 2: Evaluate changes in mitochondrial behavior in response to radiation *in vitro*.** To evaluate changes in mitochondrial behavior, fluorescence of cellular ROS production and mitochondrial membrane polarization were quantified glycolytic enzyme Hexokinase-II expression may give further insight as to the exact nature of these metabolic changes.

This series of studies was designed to elucidate some of the mechanistic underpinnings of how radiation impacts cells in addition to the initial surge of free radicals and ROS creating single-strand and double-strand DNA breaks. **The contribution of this work is that we demonstrated not only that radiation creates prompt metabolic changes in cells, but also that these changes manifest differently in different cell types. Radiosensitive cells showed little to no metabolic response, whereas radioresistant cells showed shifts in metabolic signature and protein expression consistent with increased aerobic glycolysis.**

# Chapter 2: Radiation therapy and its interaction with the tumor microenvironment: outlook and perspective

## 2.1 Introduction

According to the American Cancer Society facts and figures, almost 1.7 million new cancer cases were diagnosed in the 2016 calendar year (*1*). The causes of cancer are wide-ranging, from elevated risks caused by behaviors such as smoking (lung) and poor diet (gastrointestinal) to inherited genetic mutations and/or predispositions such as retinoblastoma, BRCA, etc. The sites at which cancers may occur are equally diverse and can vary greatly in levels of aggression and lethality. It has thus been necessary to develop a wide and equally varied arsenal of treatments to combat cancer including chemotherapeutic drugs, immunotherapy agents and a multitude of different forms of radiation therapy. These regimens are typically deployed concomitantly to achieve greater therapeutic gains.

Some form of radiation therapy is typically prescribed for a large proportion of overall treatment regimens because of its therapeutic versatility. In addition to curative applications, radiation therapy is sometimes deployed for palliative purposes, for example, sites such as brain lesions, and bone metastases to relieve spinal pressure (*2*, *3*). Advancements in radiotherapy technology have improved the ability for physicians to escalate doses and theoretical biological effective doses while decreasing normal tissue damage. These advancements include improvements to spatial distributions as well as changes in fractionation regimens, respectively (*4*-*7*).

The implementation of multiple beams with optimized modulation within each field from external beam radiation therapy (EBRT) introduces the ability to directly spare tissues from escalated doses by bringing beams from multiple angles optimized to decrease dose build-up for intervening tissue between the beam source and the target volume. One can also perform subvolume boosting (*8-10*) with modern forms of intensity-modulated radiation therapy (IMRT) treatments such as TomoTherapy (*11, 12*) among several other examples (*13*). Brachytherapy is an alternative to EBRT approaches where radioactive seeds are implanted directly into the tumor tissue to deliver a highly localized dose distribution at either low dose or high dose rates. Brachytherapy has seen many applications such as gynecological (*14, 15*), prostate (*15-18*) and breast (*15, 19*) cases.

A further innovation in radiation therapy delivery has come from alterations in dose scheduling. Historically, typical radiotherapy regimens are delivered in 2 Gy "fractions" five days per week over a certain, pre-specified number of weeks (*7*). Traditional fractionation schemes were devised to overcome challenges presented by hypoxia and repopulation which will be further discussed below (*20, 21*). "Hypofractionated" describes treatments that deliver a prescribed dose over fewer fractions of doses over 2 Gy, whereas "hyperfractionated" describes treatments that deliver a prescribed dose over more fractions of doses less than 2 Gy. Hypofractionated and stereotactic strategies have shown significant promise in treatment success and have become more and more prevalent (*4-6*).

Radiation effects of cells have been typically described by the linear-quadratic model which is an empirical model based on fits to cell survival curves. The model's theoretical assumptions are simple. Cells are killed initially by DNA damage due to “hits” from radiation: the charged particles or radicals created by the ionizing radiation that damages DNA. The single-hit events (said to be represented by the $\alpha$ term) are proportional to dose, and multi-hit events (represented by $\beta$) are proportional to the square of the dose. The surviving fraction, S, as a function of dose, D, is as follows:

$$S = exp(-\alpha D - \beta D^2). \tag{2.1.1}$$

This model does not address the complexity of the interactions of radiation with the microenvironment, which is a highly complex biological system with a multitude of regulatory signals. Moreover, this model does not address how radiation therapy itself may perturb the biological system (*22-25*), even within the time scale of a treatment fraction (*26*).

The tumor microenvironment is a multi-scale, multi-faceted and still evolving concept (*27-30*). It spans spatial scales from intracellular, molecular interactions (*26, 31, 32*) at the protein level to vascular architecture at the tissue level (*33-36*). The microenvironment is also subject to temporal changes which impact cellular dynamics (*37, 38*). The implications of interactions between these scales are manifold and wide-ranging, dictating signals for growth and angiogenesis (*33, 39-41*). The tumor microenvironment consists of both cellular non-cellular, stromal components. Cancer-associated fibroblasts are a major player in the tumor microenvironment as well as mesenchymal stem cells and endothelial cells which may be stimulated to create new blood vessels to feed tumors' voracious appetites (*42, 43*).

In normal tissues, fibroblasts are largely responsible for the shaping and remodeling of tissues. Fibroblasts play a key role in regulating wound healing. The extracellular matrix (ECM) is the major stromal component of the tumor microenvironment. The ECM is comprised of cell-surface proteins that may serve as signal receptors or transducers, and collagen fibers which provide structural integrity among other functions. Chemotherapeutic regimens that target the interactions between tumor cells, the various cellular components, and the ECM structure have gained popularity in recent years (*42-47*).

A particular example of tumor microenvironment-targeted therapy that has seen wide application in clinical trials is the use of anti-angiogenic vascular endothelial growth factor (VEGF) inhibitors coupled to traditional treatment regimens. This has seen wide application in various cancer sites such as colorectal, breast and lung cancers, with only modest gains in patient survival (*48*). Sustained inflammation from immune response is also a well-known promoter of carcinogenesis due to hyperactive DNA repair and cell proliferation (*49*). Sustained expression nuclear factor light-chain-enhancer of activated B cells (NF-κB) has been shown to reduce the efficacy of both radiotherapy and chemotherapy, and thus modulation of this signaling pathway may be a key target for therapeutic improvement. However, outright suppression may actually prove detrimental as FAS, a target gene of NF-κB, is implicated in mediating apoptosis.

The ECM also plays a significant role in the progression and evolution of cancers. A high degree of collagen alignment in breast cancer has been shown to facilitate tumor metastasis. Aligned collagen fibers may penetrate basement membranes allow cancer cells to invade other tissues. Alignment of collagen in this manner has been quantified and correlated with poor patient prognosis (*50, 51*). Moreover, ECM stiffness can have great impact on tumor development; indeed, breast density has been shown to have a strong correlation to incidence of breast cancers (*52-54*). ECM properties such as stiffness and vascularity also contribute to difficulties with drug delivery of macromolecular agents not only by insufficient blood supply but also with increased interstitial fluid pressures which conspire to limit perfusion (*35, 55*). Studies have found that the family of collagen cross-linkage transcription factors lysyl oxidase (LOX) has been implicated and tumor progression via downstream transcription targets (*56, 57*). While work with nanoparticle drug delivery has shown some promise to overcome these obstacles (*58-61*), the complexity of these signaling pathways and their interactions with drug delivery will remain. Herein lies a tremendous advantage for radiotherapy: ionizing radiation is not subject to the perfusion and transport limitations that limit the delivery and efficacy of chemotherapeutic agents. This rings especially true with the technological advances in radiotherapy delivery techniques listed previously.

## 2.2 The 4 R's of Radiobiology(62)

Radiation therapy is a critical component in many therapeutic regimens and has classically been discussed within the traditional "4 Rs of radiobiology:" repair, reassortment or redistribution, repopulation and reoxygenation. It should be noted that these processes occur on varying time scales from hours to days. Considerable effort has been made to expand our knowledge about mechanistic causes of radiation injury to cells. It is now accepted that there is a 5th “R” representing inherent radiosensitivity. This last “R” has the potential to provide more personalized and adaptive treatments. Radiosensitivity, too, could be occurring on a variety of temporal and spatial scales.

Radiation therapy's effect has been traditionally attributed to cell death caused by acute cellular DNA damage, which leads to replicative failure over the course of a few cell divisions. This process has been usefully characterized by the traditional four R's of radiobiology listed above. Sublethal damage repair, one of the “R’s,” is a vital component to cellular radiation response; this repair provides the contrast between normal and cancer cells' DNA repair mechanisms. Fractionated strategies are able to work well for treating tumors with radiation because the cancer cells tend to integrate genomic damage. Cancerous cells typically possess inefficient DNA repair mechanisms but possess the ability to circumvent apoptosis which allows for radiation-induced genetic mutations to take hold propagate.

Redistribution describes the fact that cells exhibit contrast in radiosensitivity based on their progression through the cell cycle. Cells in S-phase are least sensitive to radiation because cells must go through a requisite checkpoint before activating DNA replication machinery. Before progressing to cell division, cells in S-phase would be more likely to have the needed time to activate their DNA-repair apparatus and thus correct any DNA defects introduced by radiation. By contrast, cells undergoing mitosis are the most sensitive to radiation damage, because there are no checkpoints to arrest the cell cycle once division has begun.

Repopulation occurs after repair of sublethal DNA damage and successful survival of bystander effects. Cells begin to proliferate and tumor regrowth ensues. The reoxygenation R is of vital importance because of oxygen as a modulator of the efficacy of radiation-induced DNA damage and subsequent cell killing. This chapter will focus primarily on interactions between radiation therapy and the tumor microenvironment that may be potential targets for improvement of radiation therapy, particularly metabolic reprogramming and microenvironment oxygenation changes that can occur faster than cell death.

## 2.3 Radiation induces ROS production

Ionizing radiation creates biological effects by the excitations and ionizations from either the secondary charged particles resulting from photon interactions or from primary charged particle beams and secondary charges along the paths that these beams traverse into tissue. The amount of total energy deposited by a 60 Gy (J/kg) prescription into a tumor with a mass of 2 grams is very small – just 0.12 J. That amount of energy is very small – too small in fact to attribute the biological effects to thermal mechanisms. Radiation interacts with deoxyribonucleic acid (DNA) molecules in two ways: through direct action and indirect action.

In direct action, photons (or charged particles) interact with and ionize atoms in DNA molecules themselves. For low-linear energy transfer, radiation such as electrons, and photons, the majority of radiation interactions are with water molecules which are the major component of cells. The ionization of water molecules (radiolysis) liberates secondary electrons, which are free to create a multitude of reactive intermediates, such as free electrons (*e*-), hydrogen radicals ($H^{\cdot}$), hydrogen gas ($H_2$) and hydrogen peroxide ($H_2O_2$). Free electrons have kinetic energy imparted on them by the ionization event and may create lesions in DNA molecules or cellular proteins. With molecular oxygen in solution, these free electrons and $H^{\cdot}$ very quickly equilibrate between superoxide and perhydroxyl ($O_2^{\cdot}$-/$HO_2^{\cdot}$) conjugate acid/base pairs. Organic radicals ($R^{\cdot}$) also form readily from ionizations and excitations that take place close to biomolecules and result in peroxyl radicals ($RO_2^{\cdot}$) following interaction with molecular $O_2$ present in solution (*24, 62*). In addition to creating damage in genetic information, ROS also create oxidative stresses in other organelles that can result in drastic changes in cellular behavior (*63*).

## 2.4 Oxygen and the Tumor Microenvironment

Molecular oxygen present in solution is a vital ingredient for radiosensitivity because it allows the formation of the higher-order ROS like peroxyl radicals and superoxide anions. These ROS can create permanent DNA damage through chemical interactions at sites where energetic electrons ejected from atoms in water molecules by photon interactions have interacted with DNA strands. Studies have demonstrated that well-oxygenated cells are approximately three times as likely to be killed by radiation as are hypoxic cells. This observation, known as the oxygen enhancement effect, has long been a target for radiation therapy improvement (*64, 65*).

Moreover, availability of oxygen is a key, mediating factor in metabolic homeostasis, because it acts as the final electron acceptor in the electron transport chain. Because of this key role, available oxygen plays a critical role in allowing the 16-fold more efficient oxidative phosphorylation versus glycolytic pathways for the generation of cellular adenosine triphosphate (ATP). Mitochondrial respiration results in ROS production under normal physiological conditions and cellular ROS are a vital component to cellular redox state (*66-68*). Oxygen also plays a key role in the mediation of hypoxia-inducible factor (HIF) protein complexes (*30, 69-72*). Finally, lack of available oxygen (hypoxia) exerts stresses on cells that encourage the decoupling of glycolysis from respiration such that it can become the primary energy supply (*73*).

## 2.5 Radiation and HIF-1

Oxygen and ROS concentration also has a profound effect on HIF-1α concentration and thus the formation of the HIF-1 complex. HIF-1 is a heterodimeric protein consisting of an alpha and a beta subunit. The aryl hydrocarbon nuclear translocator (ARNT), or HIF-1β concentration, is not dependent upon oxygen concentration; however, under normoxic conditions, the HIF-1α subunit is hydroxylated, sequestered by the von Hippel-Lindau tumor suppressor protein and subsequently degraded. Under hypoxic conditions, HIF-1α is not hydroxylated and thus is able to complex with the HIF-1β subunit and form the HIF-1 heterodimer. This pathway is a key mechanism for cellular oxygen sensing. HIF-1 is responsible for regulating several processes downstream as shown in figure 2.5.1, particularly those related to coping with hypoxia-induced stresses whose effects are realized at multiple scales, both spatial and temporal.

It has also been demonstrated that free radicals and ROS generated from ionization events in cellular (radiolysis) water can have a stabilizing effect on the HIF-1α subunit (*74*).

This ability of the cell to react to ROS transients has profound implications on metabolic function because of its aforementioned role in sensing oxygen concentration. Indeed, a large dose of radiation has been demonstrated to induce a strong metabolic shift toward glycolytic

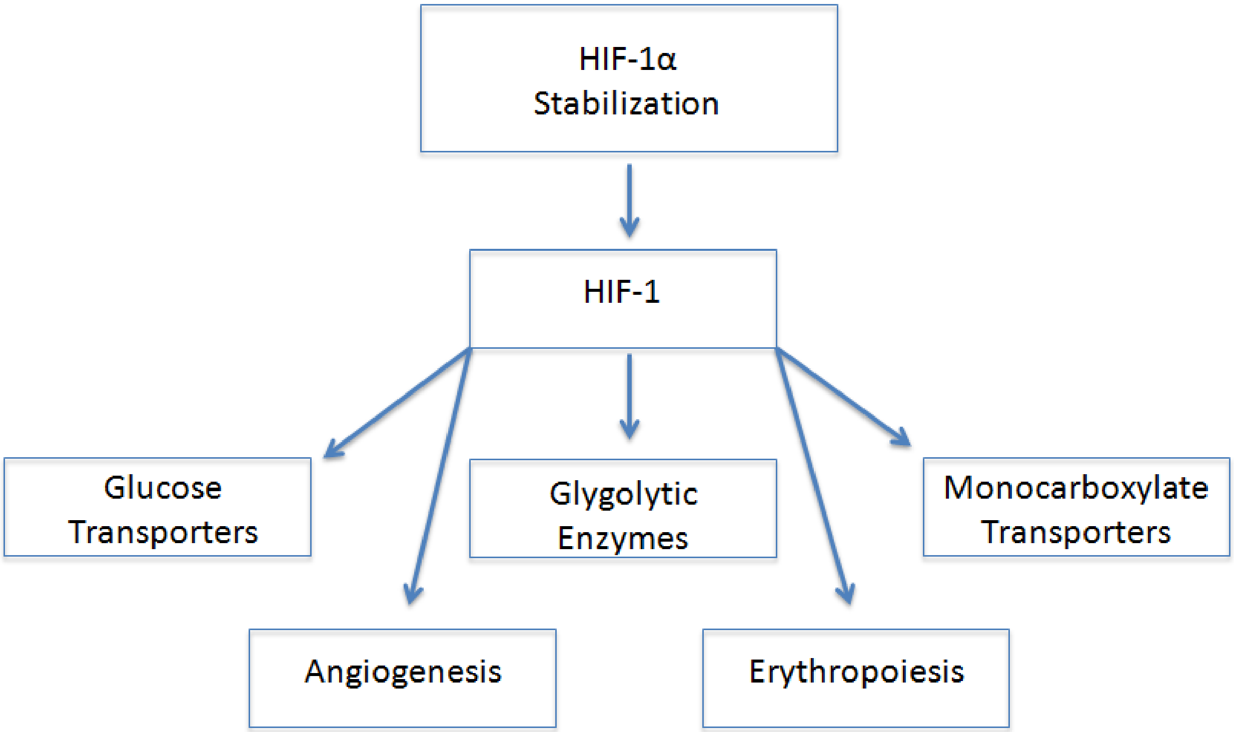

**Figure 2.5.1: Transcriptional consequences of HIF-1α upregulation**. This stabilization may occur through a multitude of mechanisms, such as loss of function of the Von Hippel-Lindau protein, hypoxia or excess ROS.

pathways with a concomitant increase in HIF-1α expression in cancerous, radioresistant cells *in vitro*. Comparatively radiosensitive, non-cancerous cells that were subjected to the same treatment were found to have little metabolic shift and no increase in HIF-1α expression (*26*). This observation suggests that radiation responses may differ across cell types. While the causes of HIF-1 overexpression is not limited to excess ROS or hypoxia, the downstream implications remain (*75*). Indeed, these findings suggest that cells responding differently to ionizing radiation may also be related to a so-called 5th R or radiobiology: intrinsic radiosensitivity.

## 2.6 Metabolic reprogramming can alter radiosensitivity

Radiation potentially results in aberrant metabolism in several ways. There are multiple, key adaptations necessary for cancers to develop and thrive: one is to circumvent the regulatory checks of cell proliferation; another is to satisfy their voracious energy and biomass needs to sustain unfettered proliferation. This runaway proliferation also results in more opportunities for selection of cells possessing resistive mechanisms to environments found in tumors which, would normally be toxic to cells such as acidosis and hypoxia.

Because radiation has been observed to stabilize HIF-1α, it allows for the HIF-1 complex to form in excess and thus regulate critical metabolic processes downstream as diagrammed in figure 2.6.1. HIF-1 activates transcription of glucose transporters such as GLUT1 (Glucose Transporter 1) and GLUT3 (*76*), and glycolytic enzymes hexokinases I and II (HK-I and II) as well as phosphofructo-1-kinase (PFK-1). Moreover, HIF-1 transcribes critical enzymes for lactate and proton extrusion, lactate dehydrogenase A(LDH-A), pyruvate dehydrogenase kinase-1 (PDK1) and monocarboxylate transporter 4 (MCT4) (*76*, *77*). A representative schematic is shown in figure 1.10.2 Upregulation of these proteins contribute to the Warburg effect in cancers - an increase in glycolysis regardless of the availability of oxygen or lack thereof (*78*).

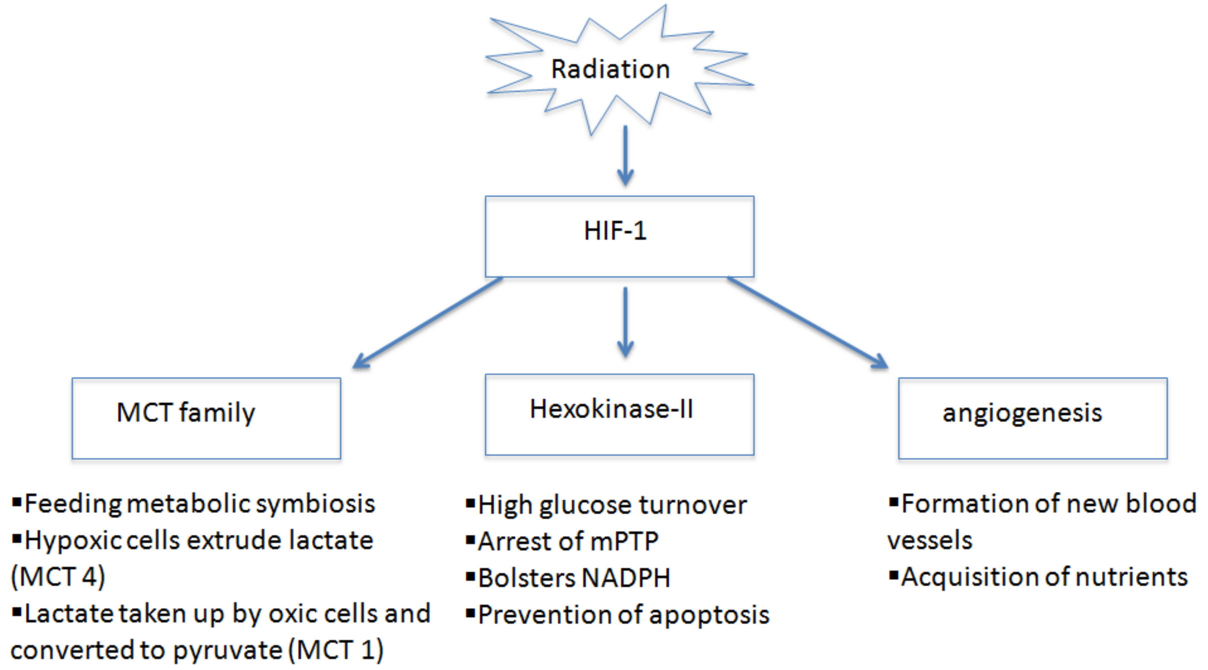

**Figure 2.6.1: HIF-1-induced metabolic reprogramming**. Monocarboxylate transferases help feed metabolic symbiosis, while HK-II helps increase the rate of glucose metabolism, as well as bolstering antioxidant defenses via NADPH. Moreover, HK-II helps prevent apoptotic cell death. HIF-1 also regulates angiogenesis to create new blood vessels.

LDH-A converts pyruvate to lactate, which removes the primary reactant for the Krebs cycle, and thus, prevents oxidative metabolism. Interestingly, it has been demonstrated that differential HIF-1 concentration in hypoxic and normoxic cells may result in symbiotic metabolic behavior in cancers which has enabled adaptation to antiangiogenic therapies (*79-81*). This symbiosis is driven by differences in HIF-1 which leads to changes in lactate transport mediated by MCT-1 and MCT-4. MCT-1 is found in the oxygenated regions of the tumors and stimulates the uptake of lactate into the cells. In the cell, the lactate is then converted to pyruvate by LDH-B and is free for utilization by the tricarboxylic (TCA)/Krebs cycle. In this way, normoxic cancer cells are able to bypass their need for glucose.

Meanwhile, in hypoxic cells, elevated levels of GLUT1, LDH-A, and MCT4 transcribed by HIF-1 result in the opposite metabolic behavior. GLUT1 increases glucose uptake into cells, which is metabolized into pyruvate and ATP. The pyruvate is then converted to lactate by LDH-A and expelled from the cell in a proton-coupled manner by MCT-4. Hypoxic cells are therefore able to satisfy their energy demand while ridding themselves of excess protons thus preventing acidification. This lactate that has been extruded may be taken up by normoxic cells thus establishing symbiotic feedback. This may last until the hypoxic cells consume the supply of glucose and are no longer able to generate energy via glycolysis (*73*), which results in massive cell death and an opportunity for natural selection of more aggressive cell phenotypes.

## 2.7 Radiation alters mitochondria

As stated previously, $O_2$ and ROS concentrations are crucial mediators in the regulation of metabolic function. Because mitochondria comprise a significant volumetric component of cells (4-25%), the flood of free radicals and ROS resultant from ionizing radiation has a potentially tremendous impact *in vitro* (*82*). Mitochondria serve as the main source for ROS production in healthy cells through the natural products of the TCA or Krebs cycle, the electron transport chain (ETC) and oxidative phosphorylation (oxphos). Like nuclear DNA, Mitochondrial DNA is susceptible to ROS-induced, oxidative damage from irradiation (*83*). Indeed, previous studies have shown that mitochondrial DNA is more sensitive to oxidative damage from ionizing radiation than nuclear DNA both promptly and hours after the insult from radiation (*84, 85*). ROS not only create damage to DNA molecules in mitochondria but also impact biomolecules involved in proper function of the ETC for example, the peroxidation of inner mitochondrial membrane protein cardiolipin which impairs the functions of mitochondrial complexes I and III (*86, 87*).

Oxidative stress from excess ROS also plays an important role in inducing permeability changes in the mitochondrial membranes. The mitochondrial permeability transition pore (mPTP) has been shown to be sensitive to the concentration of cellular ROS (*23*). The opening of the pore results in the degradation of mitochondrial proton gradients that are normally maintained to create the polarization necessary to sustain ATP synthase activity. When opened in normal cells, the mPTP also serves an important role in mediating cell death through both apoptosis and necrosis. Prolonged periods of depolarization and permeability result in elevated $Ca^{2+}$ concentrations, which in turn may depolarize other mitochondria and cause subsequent pore opening. This greatly increases the cellular concentration of cytochrome c which participates in the formation of the apoptosome (cell death protein) by interaction with procaspase and activates the so-called cellular "wheel of death" and ultimately results in apoptotic cell death. However, the formation of the apoptosome requires energy in the form of ATP that is supplied by functional, respiring mitochondria. If a critical mass of mitochondrial function has been compromised by permeability transition, insufficient ATP levels will result in necrotic death due to metabolic starvation.  How these mechanisms differ across cell types and to cancer cells is less well known.

Hexokinase II (HK-II) is an interesting factor in tumor adaptation because hexokinases are the family of enzymes that initiate glucose metabolism.  HK-II is unique because it is the isoform of hexokinase that is primarily expressed in cancerous cells, perhaps in part because it is a transcription target of the HIF-1 complex.  Moreover, HK-II has two active glucose binding sites, which gives these cells a greater ability to metabolize glucose and compensate for the energy inefficiency of glycolytic pathways.  HK-II has been observed to prevent the opening of the mPTP and thus may play a role in preventing necrotic and apoptotic cell death thus affecting treatment efficacy.

Excess ROS have also been implicated in inducing further ROS release.  Zorov *et al.* observed that ROS exposure resulted in depolarization of mitochondria in isolated cardiac myocytes.  The mitochondrial permeability transition resulted in release of further ROS, a process called ROS-induced ROS release (RIRR) (*88*).  Leach et al observed that radiation could trigger this mitochondrial permeability transition and leads to bursts of ROS and reactive nitrogen species (*82*).

## 2.8 Oxygen delivery and availability

At its largest scale, the microenvironment is organized at the tissue level.  This consists of a multitude of cell types, such as vascular infrastructure, adipose cells, or collagen fibers. However, this scale is not simply limited to different cell types.  Vasculature is a particularly important therapeutic target because it has been demonstrated that anti-angiogenic agents deployed in tandem with traditional therapies have shown promise for improving curative success, interference from metabolic symbiosis notwithstanding (*79, 89, 90*).

The physiology of tumors is unique and different from that of their normal tissue counterparts. The normal tissue microenvironment is designed to have orderly blood vessels and flow to deliver nutrients and oxygen homogenously. Conversely, a tumor is comprised of highly tortuous and irregular microvessels, which sometimes lack basement membrane causing them to be relatively more permeable to fluids (*91, 92*). This increased permeability creates a very hypertensive microenvironment for the tumor compared to normal tissues. The microvessels in a tumor are sometimes comprised of shunt vessels and other times have blind ends, causing irregular blood flow and hence the heterogeneous distribution of oxygen and nutrients. The heterogeneous distribution of oxygen ranges from regions of chronic hypoxia to intermediate and often acute hypoxia to well-oxygenated regions. Chronic hypoxia results from a complete lack of oxygen available to cells beyond the diffusion distance for respiration. This condition is usually permanent and often referred to diffusion-limited hypoxia. On the other hand, acute hypoxia results from spatiotemporal variations in oxygen that are sometimes intermittent or cyclic (*93*). This turns out to occur in areas of intermediate oxygen availability. Oxygen availability at the time of radiation is critical to the outcome of treatment (*94*). In fact, for hypofractionated treatments that are becoming more popular, oxygen becomes a dominant concern for 5 or fewer fractions (*38, 95*). The dynamics of cancer cells at intermediate oxygen levels have been found to play a very important role in radiotherapy success as they have been associated with radiation resistance and metastasis through accumulation and stabilization of HIF-1α (*96*).

Tumor oxygen partial pressures in acute hypoxia vary on timescales between minutes, tens of minutes, or even hours to days (*30, 37, 97, 98*). The phenomenon of acute hypoxia is not well understood. In fact, no correlations have been found between hemodynamics and partial oxygen pressures in perivascular spaces (*99*). Correlations have however been found between oxygen partial pressure with red cell flux in tissue (*100*) and perivascular spaces (*97*) in acute hypoxia.

Another school of thought has been that fluctuations of oxygen in a tumor is due to a consumption mechanism rather than a supply one. Calculations done by Secomb *et al.* (*101*) show that changes in oxygen content will be largely dictated by a consumption mechanism rather than a supply one. Che Fru *et al.* (*37*) have measured frequencies above pink noise that indicate regular oscillations in addition to random fluctuations in a tumor, using blood oxygen level-dependent magnetic resonance imaging. In this study, fluctuations with regular frequencies occurred in patches heterogeneously distributed throughout the tumor. They posited that regular oscillations in tumor oxygen partial pressures are due to the well-established nonlinear metabolic mechanism of the glycolytic oscillator, which has been well studied in yeast (*102*) and exhibit frequencies similar to those observed.

The effects of radiation on the frequencies observed in acute hypoxia in tumors have not yet been researched. However, Olive *et al.* observed a global decrease in oxygen consumption following a perturbation of murine tumors with radiation, accompanied by an overall increase in tumor perfusion (*103*). Similarly, Bussink *et al.* found that hypoxia decreased significantly as measured by pimonidazole staining in murine tumors in-vivo just hours following irradiation (*104*).

## 2.9 Perspective

Radiation therapy is an important component of many cancer therapeutic regimens that has seen considerable improvement since it was first implemented for skin tumors a century ago. The crude skin applicators have been replaced by linear accelerators with multiple energies and multiple modalities which greatly increase the accessibility of targets both deep and shallow. Different strategies of dose modulation, such as volumetric modulated arc therapy (*13*) and TomoTherapy (*11*, *12*), have increased physicians' ability to escalate dose prescriptions. This is made possible because advanced dose delivery strategies and planning systems have allowed for improved normal tissue sparing and dose shaping to provide conformal avoidance of sensitive structures and to shape the dose within the planning tumor volume, even provide for subvolume boosting.

Radiation therapy is treated in many ways as a solved problem because of these technological advances, and the many carefully conducted studies of radiobiological phenomena that helped develop the formalism of the 4 R's over the course of a century. What is now needed is a way to exploit a fifth 'R', radiosensitivity, clinically for more adaptive treatments adjusted per patient. However, it is important to note that these effects take place over different time scales. DNA repair and cell cycle redistribution can occur as quickly as within hours of radiation damage. The classical radiobiology effects of repopulation and reoxygenation occur a day following whereas reoxygenation can take several hours to days. Repopulation may take place over several weeks. However, metabolic effects following radiation have been observed within *minutes* of radiation injury *in vitro*, and metabolic reprogramming due to radiation-induced signaling may influence radiosensitivity between or even *during* radiotherapy fractions. Radiation effects on cells, both prompt and delayed, are more complex.

Part of cancer's metabolic reprogramming lies in the HIF-1 complex which systemically affects cancer treatment including radiation. Studies have shown that radiation may stabilize the HIF-1α subunit thus allowing the HIF-1 complex to form. HIF-1 has been implicated in poorer prognosis in breast and kidney cancer because of its role in promoting angiogenesis and radioprotection of vascular endothelia. Moreover, HIF-1 is implicated in metastatic signaling. This makes HIF-1 an important target for improving all therapeutic regimens, particularly radiation therapy. HIF-1's role in the aforementioned metabolic program is important because those changes in metabolism are quantifiable.

Metabolic profiling may be a useful tool for advancing radiation therapy on a biological level as opposed to a technological level because it could allow the monitoring of intrafraction dynamics. These types of improvements of radiation therapy are important because they potentially allow for adaptive treatment schemes for patient-specific treatments. Attempts to improve biological effect have already taken shape in the form of differing fractionation schemes. However, as hypofractionated schedules become more popular, consideration of potential intrafraction dynamics increases in importance. Radiation affects both perfusion and metabolism, which are key factors in oxygen availability; as a result, radiation may also affect radiosensitivity itself. With more treatments in hypofractionated schedules, radiosensitivity contrast is a real concern for maximizing treatment efficacy. These advances are critical because drug-delivery challenges will remain for the foreseeable future, and radiation therapy is not shackled by such limitations.

## 2.10 References

1. Society AC, Cancer Facts & Figures 2016. Place American Cancer Society: American Cancer Society; 2016.
2. Lutz ST, Jones J, Chow E, Role of Radiation Therapy in Palliative Care of the Patient With Cancer. Journal of Clinical Oncology 2014; 32, 2913-19.
3. Hartsell WF, Scott CB, Bruner DW, Scarantino CW, Ivker RA, Roach M, et al., Randomized trial of short-versus long-course radiotherapy for palliation of painful bone metastases. Journal of the National Cancer Institute 2005; 97, 798-804.
4. Alongi F, Scorsetti M, Hypofractionation in current clinical practice: a flash forward to the near future of radiation oncology? Tumori 2012; 98, 395-97.
5. Harnett A, Fewer fractions of adjuvant external beam radiotherapy for early breast cancer are safe and effective and can now be the standard of care. Breast 2010; 19, 159-62.
6. Schoenfeld JD, Harris JR, Abbreviated course of radiotherapy (RT) for breast cancer. Breast 2011; 20, S116-S27.
7. Shaikh M, Burmeister J, Joiner M, Pandya S, Zhao B, Liu Q, Biological effect of different IMRT delivery techniques: SMLC, DMLC, and helical tomotherapy. Medical Physics 2010; 37, 762-70.
8. Bentzen SM, Theragnostic imaging for radiation oncology: dose-painting by numbers. Lancet Oncology 2005; 6, 112-17.
9. Flynn RT, Bowen SR, Bentzen SM, Mackie TR, Jeraj R, Intensity-modulated x-ray (IMXT) versus proton (IMPT) therapy for theragnostic hypoxia-based dose painting. Physics in Medicine and Biology 2008; 53, 4153-67.

*10*. Ling CC, Humm J, Larson S, Amols H, Fuks Z, Leibel S, et al., Towards multidimensional radiotherapy (MD-CRT): Biological imaging and biological conformality. Int J Radiat Oncol Biol Phys 2000; 47, 551-60.

*11*. Mackie TR, Holmes T, Swerdloff S, Reckwerdt P, Deasy JO, Yang J, et al., Tomotherapy - A New Concept for the Delivery of Dynamice Conformal Radiotherapy. Medical Physics 1993; 20, 1709-19.

*12*. Mackie TR, Holmes TW, Reckwerdt PJ, Yang J, Tomotherapy - Optimized Planning and Delivery of Radiation-Therapy. Int J Imaging Syst Technol 1995; 6, 43-55.

*13*. Otto K, Volumetric modulated arc therapy: IMRT in a single gantry arc. Medical Physics 2008; 35, 310-17.

*14*. Solhjem MC, Petersen IA, Haddock MG, Vaginal brachytherapy alone is sufficient adjuvant treatment of surgical Stage I endometrial cancer. Int J Radiat Oncol Biol Phys 2005; 62, 1379-84.

*15*. Lee CD, Recent developments and best practice in brachytherapy treatment planning. British Journal of Radiology 2014; 87.

*16*. Demanes DJ, Ghilezan MI, High-dose-rate brachytherapy as monotherapy for prostate cancer. Brachytherapy 2014; 13, 529-41.

*17*. Hoskin P, Rojas A, Ostler P, Hughes R, Alonzi R, Lowe G, et al., High-dose-rate brachytherapy with two or three fractions as monotherapy in the treatment of locally advanced prostate cancer. Radiotherapy and Oncology 2014; 112, 63-67.

*18*. Chao MWT, Grimm P, Yaxley J, Jagavkar R, Ng M, Lawrentschuk N, Brachytherapy: state-of-the-art radiotherapy in prostate cancer. Bju International 2015; 116, 80-88.

*19.* Njeh CF, Saunders MW, Langton CM, Accelerated Partial Breast Irradiation (APBI): A review of available techniques. Radiation Oncology 2010; 5.

*20.* Gray LH, Conger AD, Ebert M, Hornsey S, Scott OCA, The concentration of oxygen dissolved in tissues at the time of irradiation as a factor in radiotherapy. Brit Jour Radiol 1953; 26, 638-48.

*21.* Thomlinson RH, Gray LH, The histological structure of some human lung cancers and the possible implications for radiotherapy. British journal of cancer 1955; 9, 539-49.

*22.* Alexandrou AT, Li JJ, Cell Cycle Regulators Guide Mitochondrial Activity in Radiation-Induced Adaptive Response. Antioxid Redox Signal 2014; 20, 1463-80.

*23.* Assaly R, d'Anglemont de Tassigny A, Paradis S, Jacquin S, Berdeaux A, Morin D, Oxidative stress, mitochondrial permeability transition pore opening and cell death during hypoxia-reoxygenation in adult cardiomyocytes. European Journal of Pharmacology 2012; 675, 6-14.

*24.* Azzam EI, Jay-Gerin JP, Pain D, Ionizing radiation-induced metabolic oxidative stress and prolonged cell injury. Cancer Lett 2012; 327, 48-60.

*25.* Kirkpatrick JP, Brenner DJ, Orton CG, The linear-quadratic model is inappropriate to model high dose per fraction effects in radiosurgery. Medical Physics 2009; 36, 3381-84.

*26.* Campos D, Peeters W, Nickel K, Burkel B, Bussink J, Kimple RJ, et al., Radiation Promptly Alters Cancer Live Cell Metabolic Fluxes: An In Vitro Demonstration. Radiation Research 2016; 185, 496-504.

*27.* Balkwill FR, Capasso M, Hagemann T, The tumor microenvironment at a glance. Journal of Cell Science 2012; 125, 5591-96.

*28*. Jing DH, Wobus M, Poitz DM, Bornhauser M, Ehninger G, Ordemann R, Oxygen tension plays a critical role in the hematopoietic microenvironment in vitro. Haematologica-the Hematology Journal 2012; 97, 331-39.

*29*. Yaromina A, Kroeber T, Meinzer A, Boeke S, Thames H, Baumann M, et al., Exploratory Study of the Prognostic Value of Microenvironmental Parameters During Fractionated Irradiation in Human Squamous Cell Carcinoma Xenografts. Int J Radiat Oncol Biol Phys 2011; 80, 1205-13.

*30*. Dewhirst MW, Relationships between Cycling Hypoxia, HIF-1, Angiogenesis and Oxidative Stress. Radiation Research 2009; 172, 653-65.

*31*. Chandel NS, McClintock DS, Feliciano CE, Wood TM, Melendez JA, Rodriguez AM, et al., Reactive oxygen species generated at mitochondrial complex III stabilize hypoxia-inducible factor-1 alpha during hypoxia - A mechanism of O-2 sensing. Journal of Biological Chemistry 2000; 275, 25130-38.

*32*. Hernansanz-Agustin P, Izquierdo-Alvarez A, Sanchez-Gomez FJ, Ramos E, Villa-Pina T, Lamas S, et al., Acute hypoxia produces a superoxide burst in cells. Free Radic Biol Med 2014; 71, 146-56.

*33*. Fenton BM, Lord EM, Paoni SF, Effects of radiation on tumor intravascular oxygenation, vascular configuration, development of hypoxia, and clonogenic survival. Radiation Research 2001; 155, 360-68.

*34*. Li YQ, Chen P, Jain V, Reilly RM, Wong CS, Early radiation-induced endothelial cell loss and blood-spinal cord barrier breakdown in the rat spinal cord. Radiation Research 2004; 161, 143-52.

35. Multhoff G, Vaupel P, Radiation-induced changes in microcirculation and interstitial fluid pressure affecting the delivery of macromolecules and nanotherapeutics to tumors. Frontiers in oncology 2012; 2, 165-65.

36. Park HJ, Griffin RJ, Hui S, Levitt SH, Song CW, Radiation-Induced Vascular Damage in Tumors: Implications of Vascular Damage in Ablative Hypofractionated Radiotherapy (SBRT and SRS). Radiation Research 2012; 177, 311-27.

37. Che Fru L, Adamson EB, Campos DD, Fain SB, Jacques SL, van der Kogel AJ, et al., Potential role of the glycolytic oscillator in acute hypoxia in tumors. Physics in Medicine and Biology 2015; 60, 9215-25.

38. Kissick MW, Campos D, Van Der Kogel A, Kimple RJ, On the importance of prompt oxygen changes for hypofractionated radiation treatments. Physics of Medicine and Biology 2013; 58, N279-85.

39. Lyubimova N, Hopewell JW, Experimental evidence to support the hypothesis that damage to vascular endothelium plays the primary role in the development of late radiation-induced CNS injury. British Journal of Radiology 2004; 77, 488-92.

40. Nguyen V, Gaber MW, Sontag MR, Kiani MF, Late effects of ionizing radiation on the microvascular networks in normal tissue. Radiation Research 2000; 154, 531-36.

41. Roth NM, Sontag MR, Kiani MF, Early effects of ionizing radiation on the microvascular networks in normal tissue. Radiation Research 1999; 151, 270-77.

42. Sun Y, Translational Horizons in the Tumor Microenvironment: Harnessing Breakthroughs and Targeting Cures. Medicinal Research Reviews 2015; 35, 408-36.

43. Sounni NE, Noel A, Targeting the Tumor Microenvironment for Cancer Therapy. Clinical Chemistry 2013; 59, 85-93.

*44*. Suh DH, Kim HS, Kim B, Song YS, Metabolic orchestration between cancer cells and tumor microenvironment as a co-evolutionary source of chemoresistance in ovarian cancer: A therapeutic implication. Biochemical Pharmacology 2014; 92, 43-54.

*45*. Haldar K, Gaitskell K, Bryant A, Nicum S, Kehoe S, Morrison J, Epidermal growth factor receptor blockers for the treatment of ovarian cancer. Cochrane Database Syst Rev 2011, 36.

*46*. Hensley P, Mishra M, Kyprianou N, Targeting caspases in cancer therapeutics. Biol Chem 2013; 394, 831-43.

*47*. Orlowski K, Rohrer Bley C, Zimmermann M, Vuong V, Hug D, Soltermann A, et al., Dynamics of tumor hypoxia in response to patupilone and ionizing radiation. PloS one 2012; 7, e51476-e76.

*48*. Ebos JML, Kerbel RS, Antiangiogenic therapy: impact on invasion, disease progression, and metastasis. Nature Reviews Clinical Oncology 2011; 8, 210-21.

*49*. Hanahan D, Coussens LM, Accessories to the Crime: Functions of Cells Recruited to the Tumor Microenvironment. Cancer Cell 2012; 21, 309-22.

*50*. Bredfeldt JS, Liu Y, Conklin MW, Keely PJ, Mackie TR, Eliceiri KW, Automated quantification of aligned collagen for human breast carcinoma prognosis. Journal of pathology informatics 2014; 5, 28-28.

*51*. Conklin MW, Eickhoff JC, Riching KM, Pehlke CA, Eliceiri KW, Provenzano PP, et al., Aligned Collagen Is a Prognostic Signature for Survival in Human Breast Carcinoma. American Journal of Pathology 2011; 178, 1221-32.

*52*. Gierach GL, Ichikawa L, Kerlikowske K, Brinton LA, Farhat GN, Vacek PM, et al., Relationship Between Mammographic Density and Breast Cancer Death in the Breast

Cancer Surveillance Consortium. Journal of the National Cancer Institute 2012; 104, 1218-27.

53. McCormack VA, Silva IDS, Breast density and parenchymal patterns as markers of breast cancer risk: A meta-analysis. Cancer Epidemiology Biomarkers & Prevention 2006; 15, 1159-69.

54. Boyd NF, Lockwood GA, Byng JW, Tritchler DL, Yaffe MJ, Mammographic densities and breast cancer risk. Cancer Epidemiology Biomarkers & Prevention 1998; 7, 1133-44.

55. Vaupel P, Pathophysiological and Vascular Characteristics of Solid Tumors in Relation to Drug Delivery. Drug Delivery in Oncology: From Basic Research to Cancer Therapy, Vols 1-3 2012, 33-64.

56. Boufraqech M, Zhang L, Nilubol N, Sadowski SM, Kotian S, Quezado M, et al., Lysyl Oxidase (LOX) Transcriptionally Regulates SNAI2 Expression and TIMP4 Secretion in Human Cancers. Clinical Cancer Research 2016; 22, 4491-504.

57. Kumar R, Singh AK, Kumar M, Shekhar S, Rai N, Kaur P, et al., Serum 5-LOX: a progressive protein marker for breast cancer and new approach for therapeutic target. Carcinogenesis 2016; 37, 912-17.

58. Hao Y, Yasmin-Karim S, Moreau M, Sinha N, Sajo E, Ngwa W, Enhancing radiotherapy for lung cancer using immunoadjuvants delivered in situ from new design radiotherapy biomaterials: a preclinical study. Physics in Medicine and Biology 2016; 61.

59. Hao Y, Altundal Y, Moreau M, Sajo E, Kumar R, Ngwa W, Potential for enhancing external beam radiotherapy for lung cancer using high-Z nanoparticles administered via inhalation. Physics in Medicine and Biology 2015; 60, 7035-43.

*60*. Ngwa W, Makrigiorgos GM, Berbeco RI, Applying gold nanoparticles as tumor-vascular disrupting agents during brachytherapy: estimation of endothelial dose enhancement. Physics in Medicine and Biology 2010; 55, 6533-48.

*61*. Ngwa W, Makrigiorgos GM, Berbeco RI, Gold nanoparticle-aided brachytherapy with vascular dose painting: Estimation of dose enhancement to the tumor endothelial cell nucleus. Medical Physics 2012; 39, 392-98.

*62*. Hall EJ, Giaccia AJ, *Radiobiology for the Radiologist*. 7th ed. Philadelphia, PA: Wolters Kluwer Health; 2012.

*63*. Cadenas E, Davies KJA, Mitochondrial free radical generation, oxidative stress, and aging. Free Radic Biol Med 2000; 29, 222-30.

*64*. Thanh-Trang C-P, Ly-Binh-An T, Colliez F, Joudiou N, El Bachiri S, Gregoire V, et al., Monitoring Tumor Response to Carbogen Breathing by Oxygen-Sensitive Magnetic Resonance Parameters to Predict the Outcome of Radiation Therapy: A Preclinical Study. Int J Radiat Oncol Biol Phys 2016; 96, 149-60.

*65*. Tran LBA, Bol A, Labar D, Karroum O, Bol V, Jordan B, et al., Potential role of hypoxia imaging using F-18-FAZA PET to guide hypoxia-driven interventions (carbogen breathing or dose escalation) in radiation therapy. Radiotherapy and Oncology 2014; 113, 204-09.

*66*. Hervouet E, Cizkova A, Demont J, Vojtiskova A, Pecina P, Hal N, et al., HIF and reactive oxygen species regulate oxidative phosphorylation in cancer. Carcinogenesis 2008; 29, 1528-37.

*67*. Acharya A, Das I, Chandhok D, Saha T, Redox regulation in cancer A double-edged sword with therapeutic potential. Oxidative Med Cell Longev 2010; 3, 23-34.

*68.* Ray PD, Huang B-W, Tsuji Y, Reactive oxygen species (ROS) homeostasis and redox regulation in cellular signaling. Cellular Signalling 2012; 24, 981-90.

*69.* Han Z-B, Ren H, Zhao H, Chi Y, Chen K, Zhou B, et al., Hypoxia-inducible factor (HIF)-1 alpha directly enhances the transcriptional activity of stem cell factor (SCF) in response to hypoxia and epidermal growth factor (EGF). Carcinogenesis 2008; 29, 1853-61.

*70.* Heddleston JM, Li Z, Lathia JD, Bao S, Hjelmeland AB, Rich JN, Hypoxia inducible factors in cancer stem cells. British Journal of Cancer 2010; 102, 789-95.

*71.* Semenza GL, HIF-1 and tumor progression: pathophysiology and therapeutics. Trends Mol Med 2002; 8, S62-S67.

*72.* Semenza GL, HIF-1 mediates the Warburg effect in clear cell renal carcinoma. Journal of Bioenergetics and Biomembranes 2007; 39, 231-34.

*73.* Sonveaux P, Vegran F, Schroeder T, Wergin MC, Verrax J, Rabbani ZN, et al., Targeting lactate-fueled respiration selectively kills hypoxic tumor cells in mice. J Clin Invest 2008; 118, 3930-42.

*74.* Moeller BJ, Cao YT, Li CY, Dewhirst MW, Radiation activates HIF-1 to regulate vascular radiosensitivity in tumors: Role of reoxygenation, free radicals, and stress granules. Cancer Cell 2004; 5, 429-41.

*75.* Semenza GL, HIF-1: upstream and downstream of cancer metabolism. Current Opinion in Genetics & Development 2010; 20, 51-56.

*76.* Iyer NV, Kotch LE, Agani F, Leung SW, Laughner E, Wenger RH, et al., Cellular and developmental control of O-2 homeostasis by hypoxia-inducible factor 1 alpha. Genes Dev 1998; 12, 149-62.

*77*. Zancan P, Sola-Penna M, Furtado CM, Da Silva D, Differential expression of phosphofructokinase-1 isoforms correlates with the glycolytic efficiency of breast cancer cells. Mol Genet Metab 2010; 100, 372-78.

*78*. Warburg O, On the origin of cancer cells. Science 1956; 123, 309-14.

*79*. Romero-Garcia S, Lopez-Gonzalez JS, Baez-Viveros JL, Aguilar-Cazares D, Prado-Garcia H, Tumor cell metabolism An integral view. Cancer Biol Ther 2011; 12, 939-48.

*80*. Allen E, Mieville P, Warren CM, Saghafinia S, Li L, Peng MW, et al., Metabolic Symbiosis Enables Adaptive Resistance to Anti-angiogenic Therapy that Is Dependent on mTOR Signaling. Cell Reports 2016; 15, 1144-60.

*81*. Pisarsky L, Bill R, Fagiani E, Dimeloe S, Goosen RW, Hagmann J, et al., Targeting Metabolic Symbiosis to Overcome Resistance to Anti-angiogenic Therapy. Cell Reports 2016; 15, 1161-74.

*82*. Leach JK, Van Tuyle G, Lin PS, Schmidt-Ullrich R, Mikkelsen RB, Ionizing radiation-induced, mitochondria-dependent generation of reactive oxygen/nitrogen. Cancer Research 2001; 61, 3894-901.

*83*. Morales A, Miranda M, Sanchez-Reyes A, Biete A, Fernandez-Checa JC, Oxidative damage of mitochondrial and nuclear DNA induced by ionizing radiation in human hepatoblastoma cells. Int J Radiat Oncol Biol Phys 1998; 42, 191-203.

*84*. Yakes FM, VanHouten B, Mitochondrial DNA damage is more extensive and persists longer than nuclear DNA damage in human cells following oxidative stress. Proceedings of the National Academy of Sciences of the United States of America 1997; 94, 514-19.

*85*. Yoshida T, Goto S, Kawakatsu M, Urata Y, Li T-S, Mitochondrial dysfunction, a probable cause of persistent oxidative stress after exposure to ionizing radiation. Free Radical Research 2012; 46, 147-53.

*86*. Chicco AJ, Sparagna GC, Role of cardiolipin alterations in mitochondrial dysfunction and disease. Am J Physiol-Cell Physiol 2007; 292, C33-C44.

*87*. Fry M, Green DE, Cardiolipin requirement for electron-transfer in complex-I and complex-III of the mitochondrial respiratory chain. Journal of Biological Chemistry 1981; 256, 1874-80.

*88*. Zorov DB, Filburn CR, Klotz LO, Zweier JL, Sollott SJ, Reactive oxygen species (ROS)-induced ROS release: A new phenomenon accompanying induction of the mitochondrial permeability transition in cardiac myocytes. Journal of Experimental Medicine 2000; 192, 1001-14.

*89*. Du Y, Peyser ND, Grandis JR, Integration of molecular targeted therapy with radiation in head and neck cancer. Pharmacology & Therapeutics 2014; 142, 88-98.

*90*. Hsu HW, Wall NR, Hsueh CT, Kim S, Ferris RL, Chen CS, et al., Combination antiangiogenic therapy and radiation in head and neck cancers. Oral Oncol 2014; 50, 19-26.

*91*. Brown JM, Giaccia AJ, The Unique Physiology of Solid Tumors: Opportunities (and Problems) for Concer Therapy. Cancer Res 1998; 58 1408-16.

*92*. Vaupel P, Tumor microenvironmental physiology and its implications for radiation oncology. Seminars in radiation oncology 2004; 14, 198-206.

*93*. Dewhirst MW, Cao Y, Moeller B, Cycling hypoxia and free radicals regulate angiogenesis and radiotherapy response. Nat Rev Cancer 2008; 8, 425-37.

*94*. Gray LH, Conger AD, Ebert M, Hornsey S, Scott OCA, The Concentration of Oxygen Dissolved in Tissues at the Time of Irradiation as a Factor in Radiotherapy. The British Journal of Radiology 1953; 26, 638-48.

*95*. Carlson DJ, Keall PJ, Loo BW, Jr., Chen ZJ, Brown JM, Hypofractionation Results in Reduced Tumor Cell Kill Compared to Conventional Fractionation for Tumors with Regions of Hypoxia. Int J Radiat Oncol Biol Phys 2011; 79, 1188-95.

*96*. Martinive P, Defresne F, Quaghebeur E, Daneau G, Crokart N, Grégoire V, et al., Impact of cyclic hypoxia on HIF-1α regulation in endothelial cells – new insights for anti-tumor treatments. FEBS Journal 2009; 276, 509-18.

*97*. Kimura H, Braun RD, Ong ET, Hsu R, Secomb TW, Papahadjopoulos D, et al., Fluctuations in Red Cell Flux in Tumor Microvessels Can Lead to Transient Hypoxia and Reoxygenation in Tumor Parenchyma. Cancer Research 1996; 56, 5522-28.

*98*. Cairns RA, Kalliomaki T, Hill RP, Acute (Cyclic) Hypoxia Enhances Spontaneous Metastasis of KHT Murine Tumors. Cancer Research 2001; 61, 8903-08.

*99*. Helmlinger G, Yuan F, Dellian M, Jain RK, Interstitial pH and pO2 gradients in solid tumors in vivo: High-resolution measurements reveal a lack of correlation. Nat Med 1997; 3, 177-82.

*100*. Lanzen J, Braun RD, Klitzman B, Brizel D, Secomb TW, Dewhirst MW, Direct Demonstration of Instabilities in Oxygen Concentrations within the Extravascular Compartment of an Experimental Tumor. Cancer Research 2006; 66, 2219.

*101*. Secomb TW, Hsu R, Ong ET, Gross JF, Dewhirst MW, Analysis of the Effects of Oxygen Supply and Demand on Hypoxic Fraction in Tumors. Acta Oncologica 1995; 34, 313-16.

*102*. Sel'Kov EE, Self-Oscillations in Glycolysis: 1. A Simple Kinetic Model. European Journal of Biochemistry 1968; 4, 79-86.

*103*. Olive PL, Radiation-Induced Reoxygenation in the SCCVII Murine Tumor- Evidence for a Decrease in Oxygen-Consumption and an Increase in Tumor Perfusion. Radiotherapy and Oncology 1994; 32, 37-46.

*104*. Bussink J, Kaanders J, Rijken P, Raleigh JA, Van der Kogel AJ, Changes in blood perfusion and hypoxia after irradiation of a human squamous cell carcinoma xenograft tumor line. Radiation Research 2000; 153, 398-404.

# Chapter 3: Radiation promptly alters cancer live cell metabolic fluxes: an *in vitro* demonstration

## 3.1 Introduction

Typical clinical radiotherapy regimens schedule daily “fractions,” which are delivered over minutes to tens of minutes (*1*). Tissue oxygenation is a proven key modulator in the effectiveness of radiation therapy (*2*), and several studies have shown that radiation itself impacts oxygen consumption (*3-5*). It is important to continue to improve radiation therapy as a large fraction of cancer patients receive some form of radiation therapy either as their primary form of treatment or concomitant with other treatment modalities. Metabolism and oxygen are intrinsically linked (*6, 7*); therefore, prompt changes in metabolism could cause changes in the tumor microenvironment such as available oxygen.

Usually, under aerobic conditions, cells produce energy via oxidative phosphorylation as it is considerably more efficient (36 adenosine triphosphate, or ATP, per glucose molecule) than glycolytic pathways (2 ATP per glucose molecule); however, many types of cancers utilize glycolysis as their primary source of energy production, even under aerobic conditions. This unique metabolic behavior of tumor cells is known as the "Warburg effect" (*8-11*). In addition to previously reported metabolic states such as the Warburg effect, it is thought that cancer cells may respond differently metabolically to microenvironment perturbations (*12-14*). We hypothesized that, following radiation, there might be detectable and quantifiable changes in metabolism from the physical effects of the radiation itself, and that these may occur very quickly. The hypothesis is based on the observation that *in vivo*, the oxygen level is seen to quickly change from large doses of radiation, well ahead of any cell death (*4*).

Nicotinamide Adenosine Dinucleotide (NADH) is an intrinsically fluorescent intermediate metabolite that has been utilized in a number of studies (*15-22*). Its fluorescent lifetime (the measured amount of time in the excited state) depends greatly upon its chemical state (*23, 24*). When NADH is bound to a protein complex, its fluorescence lifetime is considerably longer (~2.5 ns) versus its fluorescence lifetime in the free state (~400 ps) (*23, 25*). Therefore, bound NADH utilized in the mitochondrial electron transport chain (ETC) exhibits a considerably longer mean fluorescent lifetime whereas free NADH in the cytosol exhibits a comparatively shorter fluorescent lifetime (*21, 26, 27*).

This intrinsic fluorescent lifetime contrast for NADH was used to monitor cellular metabolism as it allows label-free quantitative assessment of key metabolic changes such as glycolysis (*28*). Not surprisingly, the ability of time-correlated Fluorescence Lifetime Imaging Microscopy (*23, 25*), or “FLIM,” to monitor lifetime with a spatial context has seen a multitude of applications (*29-31*). This has included research therapeutic studies such as the characterization of the metabolic changes of various breast cancer lines in response to chemotherapeutic drugs (*32*). FLIM has also been applied for assessing precancerous lesions in the head and neck region as well as in the breast (*26, 33*). A major reason for the growth in FLIM-based metabolic studies has been its unique ability to non-invasively monitor cellular metabolism with high resolution, its ability to quantitatively discriminate between bound and free NADH forms without being influenced by intensity levels and detection without the mitigating effects of fluorescence variations as seen in traditional fluorescence-based assays (*34*).

As a large portion of cancer patients receive radiation therapy as part of their therapeutic regimen, it is important to continue to understand the biological mechanisms that determine its efficacy. In this study, we demonstrate detectable metabolic fluxes resulting from radiation and live cells as measured by FLIM. We further assess the interplay of these metabolic fluxes with changes in oxygen consumption and HIF-1α signaling.

## 3.2 Methods and Materials

### 3.2.1. Cell culture

Two human cell lines T24, a urothelial carcinoma cell line and Normal Oral Keratinocytes (NOK) were employed in this study to compare a radioresistant and radiosensitive cell line from human cancers. T24 cells were cultured in DMEM with 4.5 g/dl glucose, 10% FBS, 1% hydrocortisone, penicillin (100 units/ml), streptomycin (100 mg/ml)(*35*). NOK cells were a kind gift of Dr. Karl Munger, Tufts University, and cultured in keratinocyte serum-free media supplemented with both EGF and Bovine Pituitary Extract. Cells were maintained as monolayer cultures at 37°C in a humidified atmosphere of 5% $CO_2$.

The dishes are clamped into a LiveCell$^{TM}$ bench top incubator, which fits in the stage of the multiphoton microscope workstation to maintain repeatable conditions (temperature and $CO_2$ gas concentration) for cells to minimize behavioral variance. The incubator assembly and control box are pictured in figure 3.2.1. The LiveCell$^{TM}$ incubator is connected to a control box via an RS-232 cable which allows the adjustment of humidity and $CO_2$ concentration within in the incubator chamber. The humidity and gas assembly is also connected to the controller box via an RS-232 cable and a gas tube which conveys water vapor and $CO_2$ gas to the chamber. The Humidity assembly connects to the incubation chamber via a bypass wye pictured below (figure 3.2.1B). To ensure the specified conditions, it is important to insert the bypass wye firmly into the humidity and gas intake aperture on the chamber lid to avoid leaks.

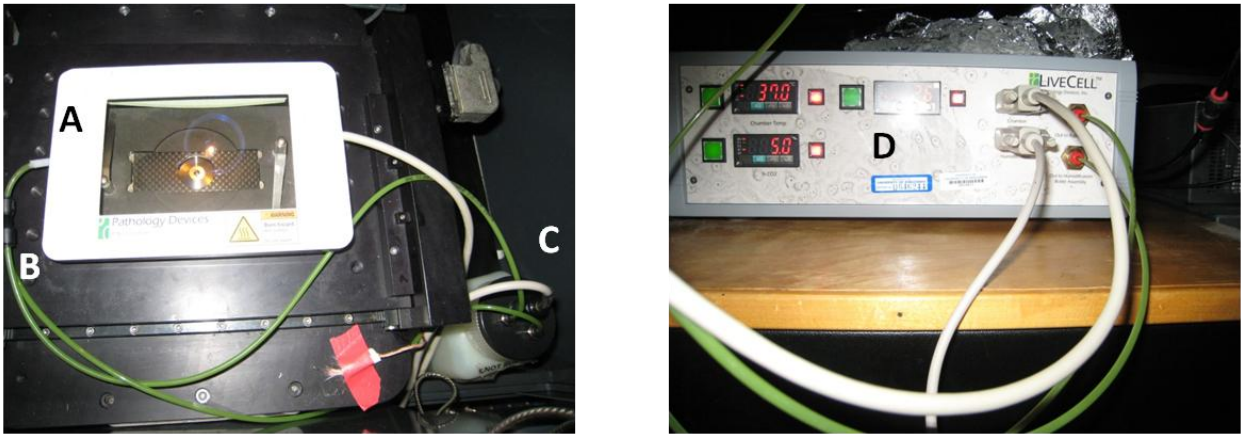

**Figure 3.2.1: LiveCellTM bench top incubator** (left) and the LiveCell$^{\text{TM}}$ control box (right). The incubator itself is labeled A. The bypass wye which the control box and the humidity chamber for water vapor and $CO_2$ use to connect to the chamber is indicated by B. The humidification bottle assembly is labeled C, and the controller is labeled D.

## 3.2.2. Irradiation and treatment with KCN, GSH, and Chrysin

Cells were irradiated to 10 Gy using a 320 kVp small animal and cell culture irradiator XRAD 320 (Precision X-Ray Inc) with a metal-ceramic anode and filtration of 1.5 mm Al + 0.25 mm Cu + 0.75 mm Sn. Cells were plated to approximately 50% confluence in 60 mm glass bottom dishes with 30 mm cover slip wells (In Vitro Scientific, D60-30-1 5-N) in 4 mL of cell media. For controls of both the imaging and cell culture conditions and to show the FLIM method was being sensitive to metabolic flux, 10 mM KCN was administered to untreated cells during imaging to produce a positive control effect (mitochondrial inhibition), and the negative control cells were simply imaged without any treatment (radiation or drug). A small subset of T24 cells was also irradiated in the presence of 10 mM glutathione for free radical scavenging. Similarly, a separate group of NOK and T24 cells were treated with 50 μM HIF-1α inhibitor chrysin (Santa Cruz Biotechnology Inc.) before irradiation.

### 3.2.3. Multiphoton Fluorescence Lifetime Imaging

For this study, a 60x magnification oil objective (CFI Apo Lambda S 60x Oil 1.4 NA) was chosen. Optical coupling between the sample and the objective increases the numerical aperture of the lens and allows for a higher number of photons to be collected. This improves signal which is at times quite low for fluorescence lifetime imaging. A high photon count is particularly important for fluorescence lifetime imaging because proper fitting of the dual exponential decay curve of NADH (bound vs free NADH) requires enough signal to obtain a good fit. For best results, an optimal amount of oil is needed; too much oil results in focal plane drift during imaging and yield unpredictable and poor images. Insufficient oil results in poor coupling between the objective and the sample focal plane. As a rule of thumb, when the sample and objective are brought together, a small "pancake" of oil should be seen (pictured in figure 3.2.2). This also has the benefit of placing the cellular monolayer close to the focal plane; therefore, minimal focal adjustment will be required.

For image collection, it is first necessary to scan the cell plate for an appropriate cluster of cells. To accomplish this, switch the DCC-100 control to H7422 (figure 3.2.3D) and use the continuous imaging button to scan (3.2.3B). When a suitable cluster of cells is found, switch the DCC-100 control to H7422L and set collection time to the desired value. For this series of experiments a 120 second integration time for five regions of interest per dish were imaged 30 minutes following radiation; during imaging, cells were maintained at 37°C and 5% $CO_2$ in the LiveCell™ stage top incubator. A 450/70 nm emission bandpass filter (Semrock) was utilized to isolate the NADH autofluorescence.

**Figure 3.2.2: Proper seating of a sample on the optical workstation**. A 6 cm (30 mm 1.5 glass bottom well) dish properly clamped into the base of the LiveCell$^{TM}$ incubator. The arrow indicates the proper amount of oil. The optimization is a subtle process, and it is preferable to err on the side of too much oil rather than too little. Too much simply results in a 5-10 minute delay while the objective and oil droplet equilibrate to avoid focal plane drift whereas too little oil results in low signal through poor optical coupling.

Fluorescence lifetime imaging microscopy (FLIM) of the intermediate metabolite NADH (Nicotinamide Adenosine Dinucleotide) is a powerful tool for quantitative imaging of cellular metabolism. NADH plays a vital role in metabolic processes and is intrinsically fluorescent. Furthermore, NADH is ubiquitous in living cells at sufficiently high concentrations for visualization. Fluorescence lifetime is defined as the amount of time a fluorophore remains in its excited state before emitting a fluorescence photon. Free (unbound) NADH has a fluorescence lifetime of approximately 400 ps, whereas NADH bound to a protein complex has a fluorescence lifetime of 2-5 ns depending on the protein to which it is bound. By obtaining a weighted average of the contribution to fluorescence of free and bound NADH, it is possible to capture a snapshot of the metabolic profile of a population of cells or even a single cell. This makes FLIM a powerful tool for evaluating metabolic responses to various treatments. In particular, this work studies the metabolic changes in a cancerous and normal cell line elicited by a large dose of radiation that would typify a hypofractionated radiotherapy regimen.

Fluorescence lifetime images of cellular NADH were obtained using multiphoton excitation at a wavelength of 740 nm utilizing a Spectra Physics MaiTai Ti:Sapphire laser. The microscope is driven by the WiscScan software developed in-house at LOCI, which is pictured below in figure 3.2.3, and its control panel is annotated in figure 3.2.5. Laser power levels are first tested by imaging pollen grains at 890 nm excitation with no band-pass filter. First, the Pockel's cell voltage is adjusted to 140 V and once the image is properly focused, the DCC voltage bias is tuned to the threshold of pixel intensity saturation using a slider pictured in figure 3.2.4. In this way, a baseline laser power measurement is obtained.

Once laser power levels are established, it is important to obtain a temporal reference point to adjust the lifetime readout based on the delays introduced by electronics and cables in the image acquisition. To obtain the reference, a non-fluorescent sample is imaged; for this work, urea crystals were employed, but other compounds with Second Harmonic properties also work due to their intrinsic signal and lack of lifetime. The laser is tuned to 740 nm, and a 370/10 nm bandpass filter is put in place to allow the second harmonic excitation of the urea crystals to reach the detector. This temporal reference is used as the Instrument Response Function (IRF) to correct for daily fluctuations in instrumental timing. In this way, the appropriate time delay can be subtracted from the overall delay from the fluorescence photons thus making it possible to obtain more accurate lifetime values.

Time-correlated Fluorescence Lifetime Imaging Microscopy was performed using a custom multiphoton laser-scanning microscope with SPC-830 Becker Hickl FLIM hardware (*22,* *36*) at the Laboratory for Optical and Computational Instrumentation (LOCI), University of Wisconsin – Madison, USA.  Fluorescence of cellular NADH was excited using multiphoton excitation at a wavelength of 740 nm utilizing a Spectra Physics MaiTai Ti:Sapphire laser. FLIM was employed to map the NADH-based metabolism of cell lines *in vitro* subjected to different treatment conditions.  Five regions of interest per dish were imaged 30 minutes following radiation, and during imaging, cells were maintained at 37°C and 5% $CO_2$ in a LiveCell™ stage top incubator.  A 450/70 nm emission bandpass filter (Semrock) was utilized to isolate the NADH autofluorescence.

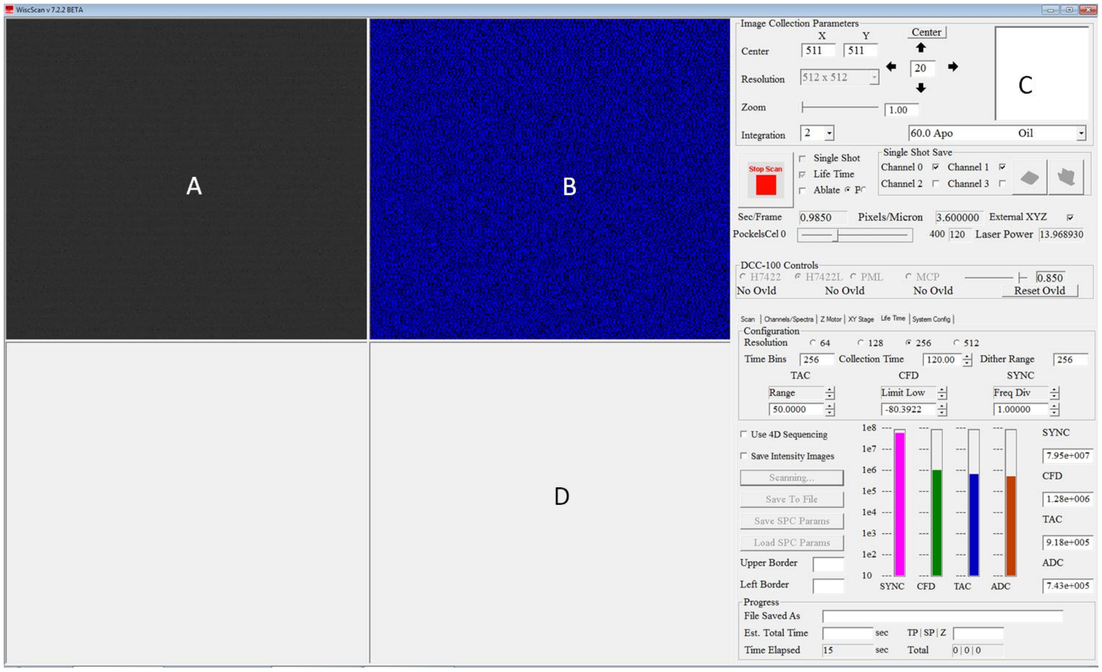

Image Collection Parameters

Center X 511 Y 511

Resolution 512 x 512

Zoom 1.00

Integration 2

20

60.0 Apo Oil

☐ Single Shot
☑ Life Time
☐ Ablate ● PC

Single Shot Save
Channel 0 ☑ Channel 1 ☑
Channel 2 ☐ Channel 3 ☐

Sec/Frame 0.9850 Pixels/Micron 3.600000 External XYZ ☑

PockelsCel 0 400 120 Laser Power 13.968930

DCC-100 Controls
○ H7422 ● H7422L ○ PML ○ MCP 0.850
No Ovld No Ovld No Ovld

Configuration
Resolution ○ 64 ○ 128 ● 256 ○ 512
Time Bins 256 Collection Time 120.00 Dither Range 256

TAC Range 50.0000
CFD Limit Low -80.3922
SYNC Freq Div 1.00000

☐ Use 4D Sequencing
☐ Save Intensity Images

Upper Border
Left Border

SYNC 7.95e+007
CFD 1.28e+006
TAC 9.18e+005
ADC 7.43e+005

Progress
File Saved As
Est. Total Time sec TP | SP | Z
Time Elapsed 15 sec Total 0 | 0 | 0

**Figure 3.2.3: WiscScan software:** A: shows the bright-field image that is refreshed live during imaging. B: shows the fluorescent field detected by the DCC. C: shows the panel which is displayed in more detail in figure 3.2.5. D: shows the lifetime image which is accumulated by the detector over the collection time specified by the use.

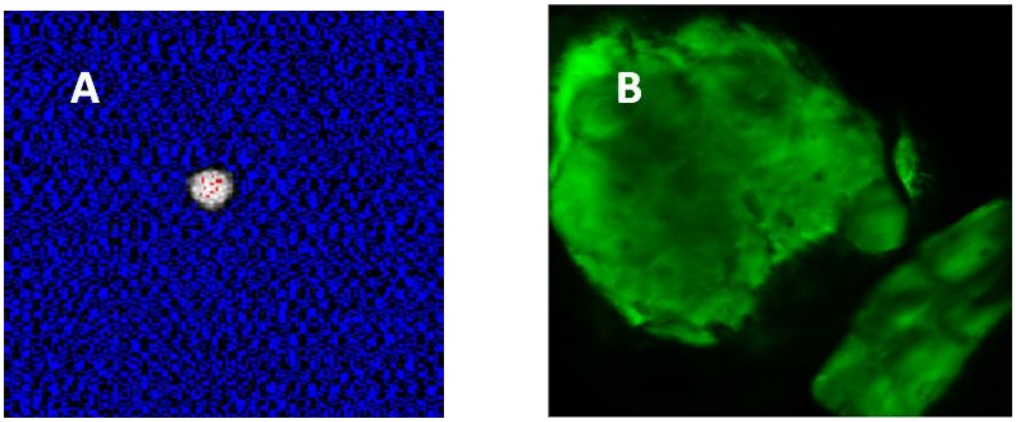

**Figure 3.2.4: Proper power measurement.** show sample images obtained from the live fluorescence channel (3.2.4A) and the lifetime channel (3.2.4B). Figure 3.2.4A in particular shows a pollen grain power calibration image where the detector bias voltage is adjusted to cause a slight intensity saturation in the image.

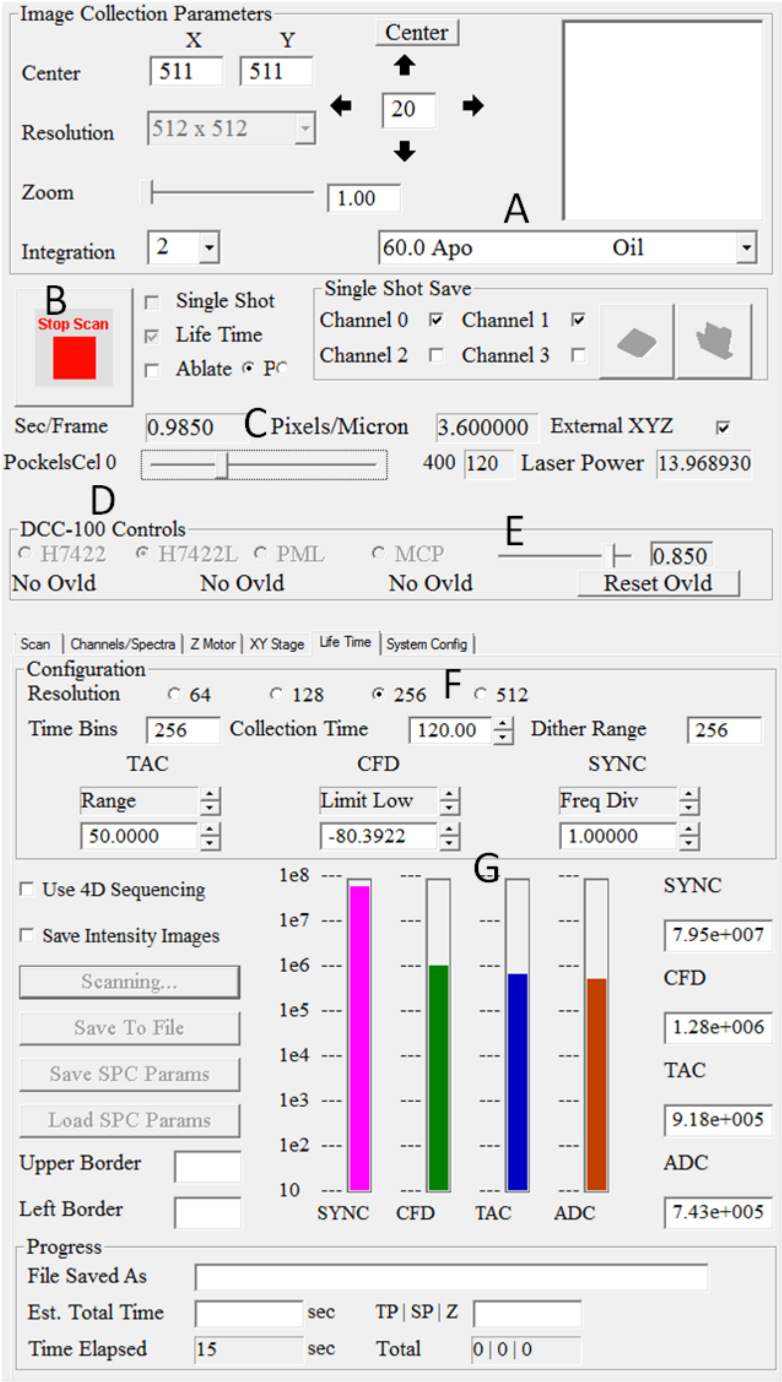

Image Collection Parameters

Center X 511 Y 511

Resolution 512 x 512

Zoom 1.00

Integration 2

20

60.0 Apo Oil

☐ Single Shot

☑ Life Time

☐ Ablate ● PC

Single Shot Save

Channel 0 ☑ Channel 1 ☑

Channel 2 ☐ Channel 3 ☐

Sec/Frame 0.9850 Pixels/Micron 3.600000 External XYZ ☑

PockelsCel 0 400 120 Laser Power 13.968930

DCC-100 Controls

○ H7422 ● H7422L ○ PML ○ MCP 0.850

No Ovld No Ovld No Ovld

Configuration

Resolution ○ 64 ○ 128 ● 256 ○ 512

Time Bins 256 Collection Time 120.00 Dither Range 256

TAC Range 50.0000

CFD Limit Low -80.3922

SYNC Freq Div 1.00000

☐ Use 4D Sequencing

☐ Save Intensity Images

Upper Border

Left Border

SYNC 7.95e+007

CFD 1.28e+006

TAC 9.18e+005

ADC 7.43e+005

Progress

File Saved As

Est. Total Time sec TP | SP | Z

Time Elapsed 15 sec Total 0 | 0 | 0

**Figure 3.2.5: The WiscScan control panel**: A cropped image of the WiscScan image parameter screen. A shows a drop-down menu that allows the selection of different objectives to adjust the pixel scale. B: shows the start and stop continuous scan button. C: shows the voltage slider for adjustment of the Pockel's Cell. D: shows the DCC controls to switch between continuous fluorescence mode versus lifetime imaging mode. E: shows the voltage slider for image detector bias. F: shows the collection time (in seconds) for lifetime imaging. G: shows the indicators for the Constant Fraction Discriminator (green), Time to Amplitude Converter (blue), and Analog to Digital converter (red). These bars should be kept between $10^5$ and $10^6$ for optimal image quality. In this particular example, the Pockel's cell voltage is likely set slightly too high.

### 3.2.4. Analysis of Fluorescence Lifetime Images

For image analysis, Becker and Hickl's SPCImage, depicted below in figure 3.2.6, is employed to calculate fluorescence lifetimes using fits to a two-component exponential decay model as follows in Eq. 3.2.1:

$$I(t) = \alpha_1 \exp\left(-\frac{t}{\tau_1}\right) + \alpha_2 \exp\left(-\frac{t}{\tau_2}\right). \tag{3.2.1}$$

The terms in this model are defined as follows: I(t) is the signal intensity as it decays with time, $\tau_1$ is the fluorescence lifetime for free NADH, and $\tau_2$ is the fluorescence lifetime of protein-bound NADH. The $\alpha_1$, $\alpha_2$ terms fit the intensity of each compartment (free and bound NADH respectively) and can be used to create the mean lifetime for the image $\tau_m$ through the relationship in Eq. 3.2.2:

$$\tau_m = \alpha_1\tau_1 + \alpha_2\tau_2. \tag{3.2.2}$$

In essence, the $\tau_m$ parameter defined in Eq. 3.2.2 is simply the weighted average of fluorescence lifetime of both the short and long components.

Free molecules of NADH are produced in the process of glycolysis which converts a molecule of glucose and two molecules of ATP into two molecules of pyruvate, and two molecules of NADH while phosphorylating four molecules of ADP into ATP in the process. In essence, glycolysis yields not only the necessary reactant for the Tricarboxylic Acid (TCA) or Krebs cycle, but also creates a net of two molecules of ATP. During oxidative phosphorylation (oxphos), NADH is bound by mitochondrial complex proteins, thus giving rise to the long fluorescence lifetime species. Free NADH has a fluorescence lifetime of approximately 400 ps;

conversely, bound NADH has a lifetime ranging between 2-5 ns, which is dependent upon the protein to which the NADH molecule is bound.

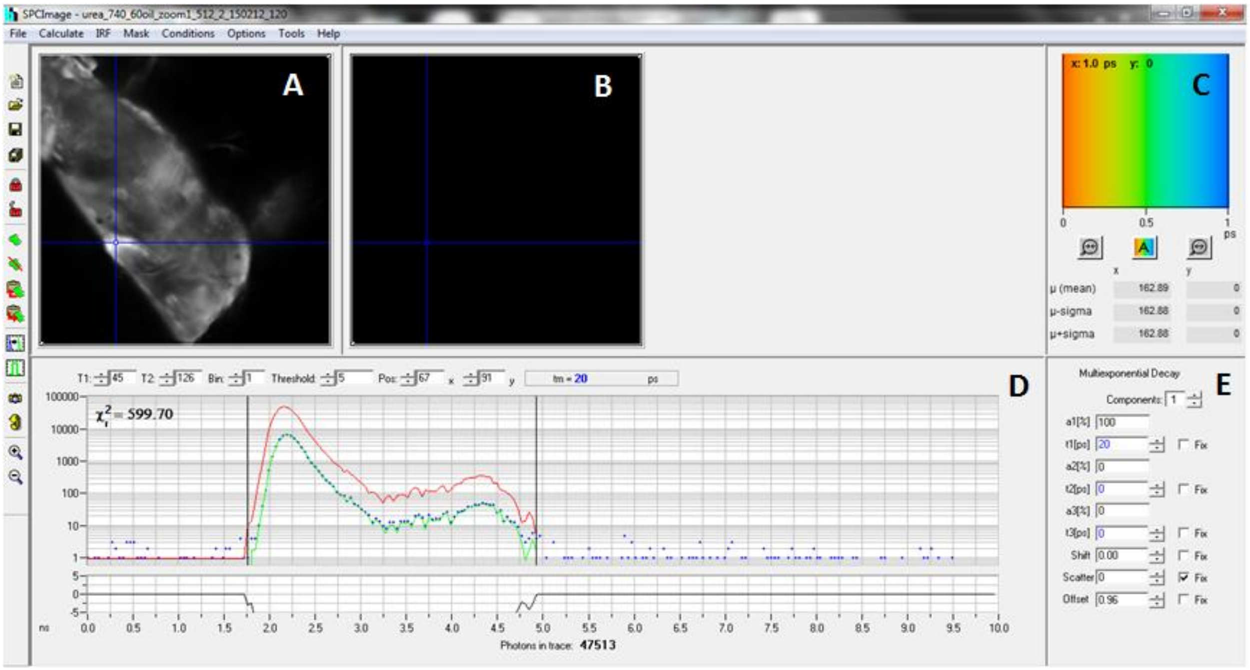

T1: 45 T2: 126 Bin: 1 Threshold: 5 Pos: 67 x 91 y tm = 20 ps

$\chi_r^2 = 599.70$

Photons in trace: 47513

| | x | y |
|---|---|---|
| μ (mean) | 162.89 | 0 |
| μ-sigma | 162.88 | 0 |
| μ+sigma | 162.88 | 0 |

Components: 1
a1[%] 100
t1[ps] 20 ☐ Fix
a2[%] 0
t2[ps] 0 ☐ Fix
a3[%] 0
t3[ps] 0 ☐ Fix
Shift 0.00 ☐ Fix
Scatter 0 ☑ Fix
Offset 0.96 ☐ Fix

**Figure 3.2.6: Becker & Hickl's SPCImage**: Above is a screen capture of the Beckr and Hickl fluorescence lifetime fitting software. The left-hand column provides buttons that can be used for image segmentation or storage of the default conditions among other functions. Panel A is the raw image display; panel B shows the image with a lifetime decay matrix color-mapped on each pixel. Panel C displays a histogram of various parameters not limited to $\tau_1$, $\tau_2$, or $\tau_m$. Panel D shows the raw photon counts in each time bin (blue diamonds), the default conditions (green line) and the decay curve fit (red line) all plotted versus time. E shows the image parameters corresponding to the selected pixels according to the intersection of the blue lines in panel A.

Because glycolytic metabolism creates free NADH, and oxphos metabolism requires the binding of NADH, the $\tau_m$ parameter can be calculated and used as a metabolic snapshot or to characterize a metabolic profile. Shorter mean lifetimes correspond to a higher concentration of free NADH and thus may be associated with glycolysis. Likewise, longer mean lifetimes correspond to a higher concentration of protein-bound NADH and thus may be associated with more oxphos.

To properly analyze lifetime images, first, one must first store the IRF in the B&H software as the "default condition". To do so, first, import the raw urea image under File →

Import. A dialogue box displaying the parameters of the image file will pop up; hit OK to continue. Adjust the vertical bars located in the photon trace panel to be as close to the rise of the photon counting peak and at the end of the reflections as shown below in figure 3.2.7B.

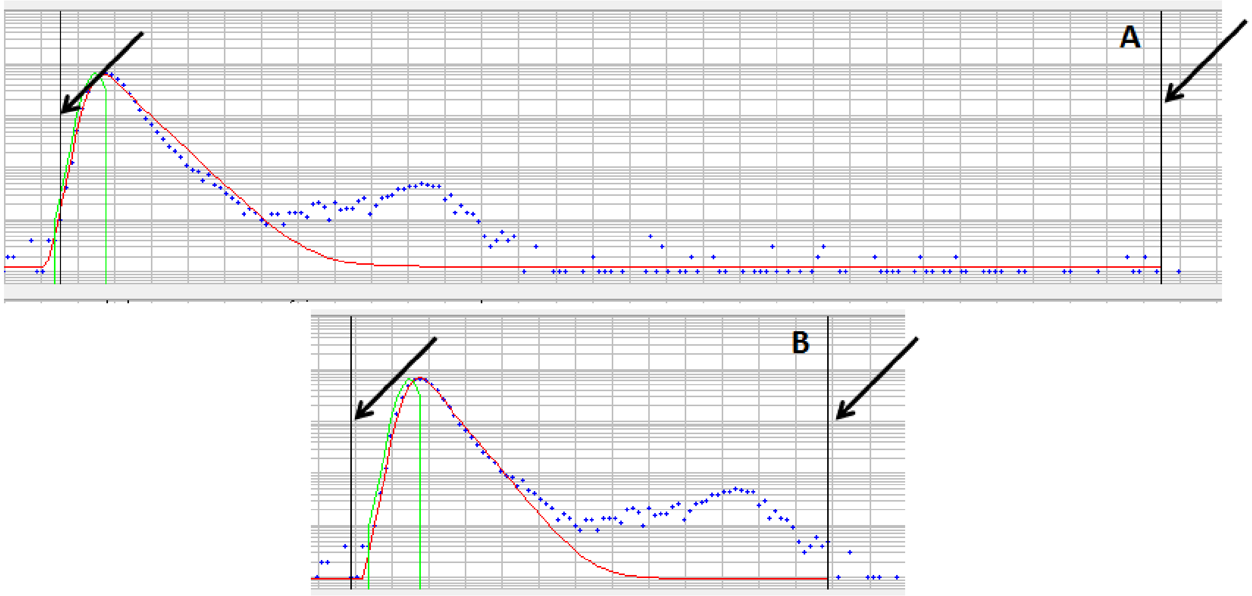

**Figure 3.2.7: Capturing the Instrument Response Function**: Panel 3.2.7A shows the photon count trace before bar adjustment, and panel 3.2.7B shows the proper placement of temporal sliders. The second "peak" is due to reflections in the collection optics.

Once the temporal sliders are appropriately placed, press the "peak adjust" button shown in panel A of figure 3.2.8. This will adjust the green "default conditions" curve to fit as the blue, photon-counting data points. Then press the "store conditions" button, shaped like a camera highlighted in panel B of figure 3.2.8 after which a dialogue box will pop up; click "Yes." Now the IRF is stored as the default conditions which can be loaded after importing an image from a biological sample by using the yellow arrow-shaped button depicted in panel C of figure 3.2.8.

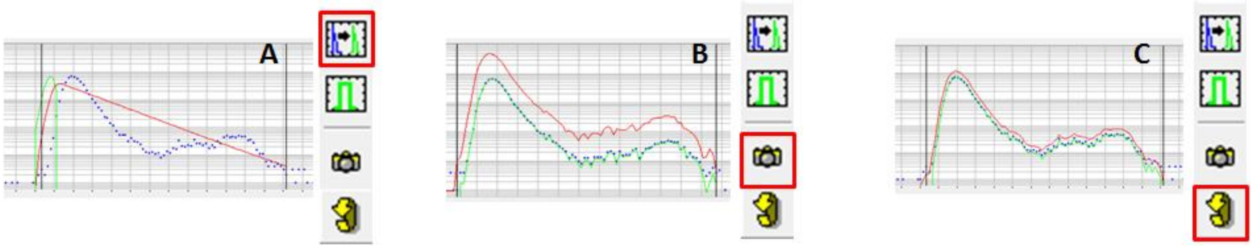

**Figure 3.2.8: Setting the Instrument Response Function**: This figure depicts the workflow of storing and loading an instrument response function (IRF). The button highlighted in panel A is for "peak adjust;" the button highlighted in panel B is the "store conditions," and the button highlighted in C loads the stored conditions to account for the photon counting delay of a biological sample.

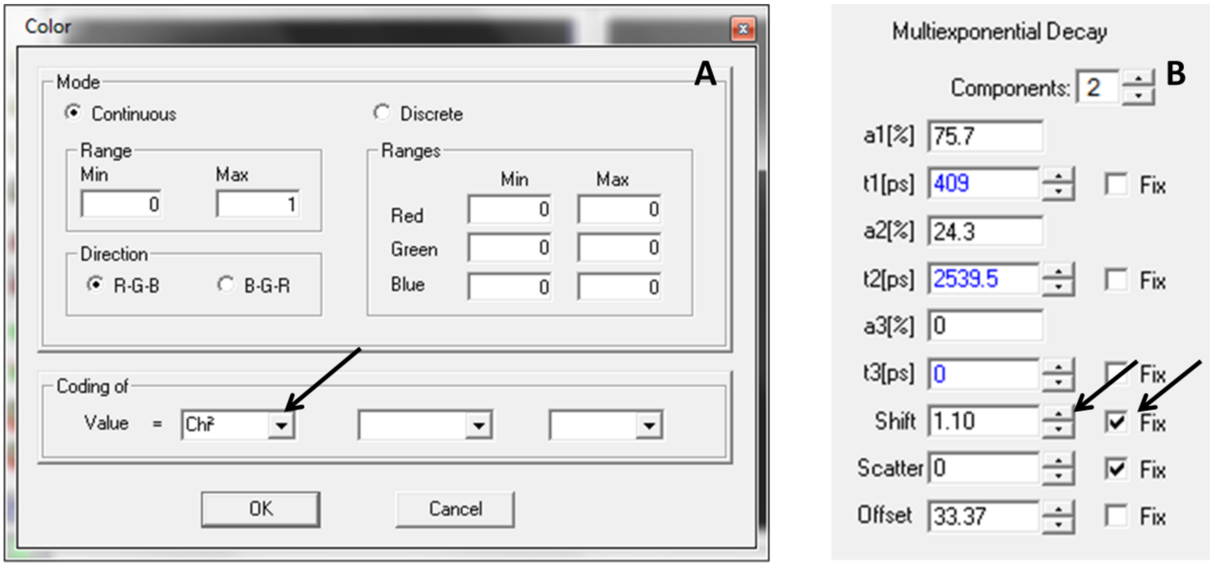

Mode
● Continuous ○ Discrete
Range: Min 0, Max 1
Direction: ● R-G-B ○ B-G-R
Ranges (Min / Max): Red 0 / 0, Green 0 / 0, Blue 0 / 0
Coding of Value = Chi²

Components: 2
a1[%] 75.7
t1[ps] 409 ☐ Fix
a2[%] 24.3
t2[ps] 2539.5 ☐ Fix
a3[%] 0
t3[ps] 0 ☐ Fix
Shift 1.10 ☑ Fix
Scatter 0 ☑ Fix
Offset 33.37 ☐ Fix

**Figure 3.2.9: The SPCImage analysis panels**: Panel A depicts the Color menu under Options in SPCImage. This menu allows the selection of various parameters that can be calculated by the software for color map overlay as indicated by the arrow. For the purposes of this data analysis, the parameters of particular interest are: $\tau_m$, $\tau_1$, $\tau_2$, $a_1$, $a_2$, Chi$^2$. The first five parameters are defined in Eqs. 3.2.1 and 3.2.2 in this section. Panel B displays the parameter frame zoomed in from image 3.2.6E. After selecting "Fix" for shift, it is possible to add slight adjustments in the timing of photon counting to achieve better (closer to 1.00) Chi$^2$ values.

With a sample and instrument response loaded, it is possible to overlay a decay matrix upon each pixel. This function is located in the Calculate → Decay Matrix which applies a color map of the selected parameter to the image which appears in panel 3.2.9B. The fit of the decay data is unlikely to be optimal on the first attempt, so it is then necessary to adjust the shift parameter. To accomplish this, it is suggested that the user select the $Chi^2$ color map, and adjust the shift parameter following fixation (figure 3.2.9B) of the shift parameter to achieve a minimum value for $Chi^2$. This function is located under Options → Color and is shown above in figure 3.2.9A. $Chi^2$ values as low as 1.07 are indicative of excellent fits, but values as high as 1.20 are acceptable as found through analysis of fluorescence lifetimes of known fluorophores.

### 3.2.5. Seahorse XF Analyzer

Metabolism was also monitored using the Seahorse XFe96 Analyzer to measure oxygen consumption rate (OCR) for assessment of respiratory activity in cells. Cells were plated on two separate 96-well plates (8 rows 12 columns): one unirradiated, and one irradiated to 10 Gy. On each plate, six columns were plated with NOK cells and the other six were plated with T24 cells. Each cell group had three control columns and three columns where the mito stress kit was administered. For the mito stress kits, each cell group had 24 replicates, whereas the controls had 22 replicates. This difference is due to the fact that each corner well was left blank to give baseline oxygen consumption measurements. The plate map is shown below in figure 3.2.10.

The mito stress kit consists of a series of three injections into the wells of oligomycin, carbonyl cyanide-p-trifluoromethoxyphenylhydrazone (FCCP) and rotenone/antimycin. Basal respiration was measured before injections under each treatment condition to assess normal oxygen consumption under each condition. Error bars shown in figure 3.6.3 are the standard deviations of the measurements at each respective time point. More information on the function of each injection can be found below. Relative well-to-well cell counts were measured using crystal violet staining followed by resolubilizing with acetic acid per the protocol set forth by Kueng *et al* (*37*).

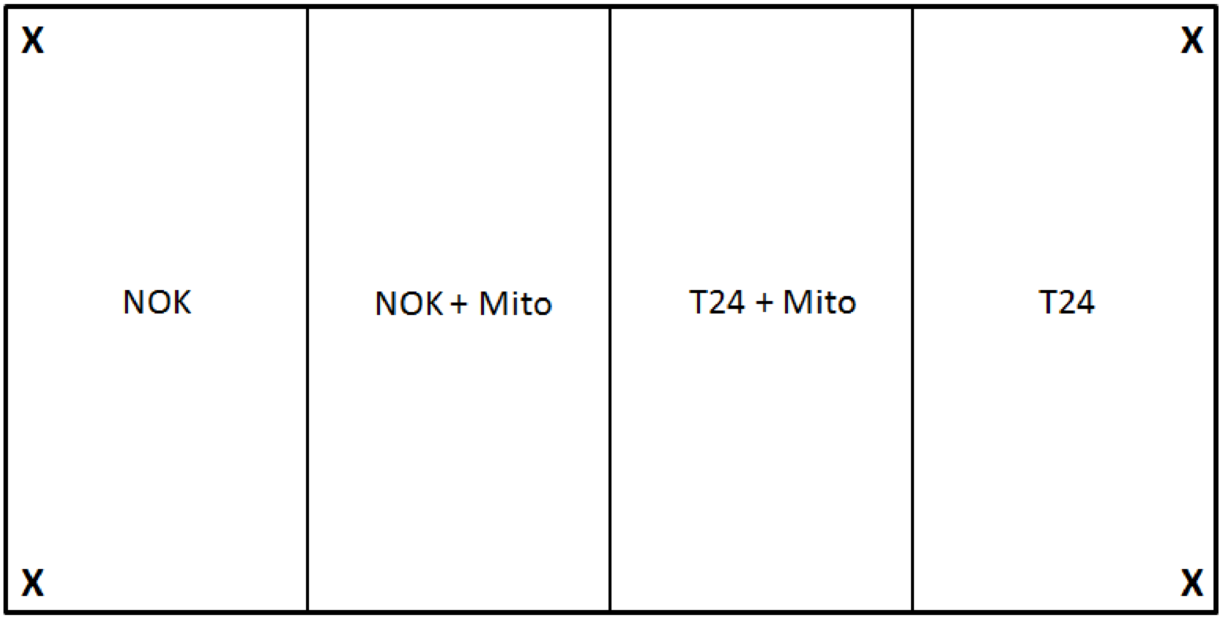

**Figure 3.2.10: Plate map for Seahorse XF Assay**: A schematic of the plate layout for mitochondrial assessment. The X's in each corner correspond to blank wells for baseline fluorescence. The Seahorse plate is an 8 row by 12 column; for these experiments, the 12 columns are divided into groups of 3 (24 wells for Mito kit and 22 for control) to provide sufficient statistical power. This experimental grouping allows for the drug injections to be sequential between columns 4-9. Because there are four injection ports to load for each well, it is vital to simplify the drug-loading to avoid errors that could waste an entire cell plate.

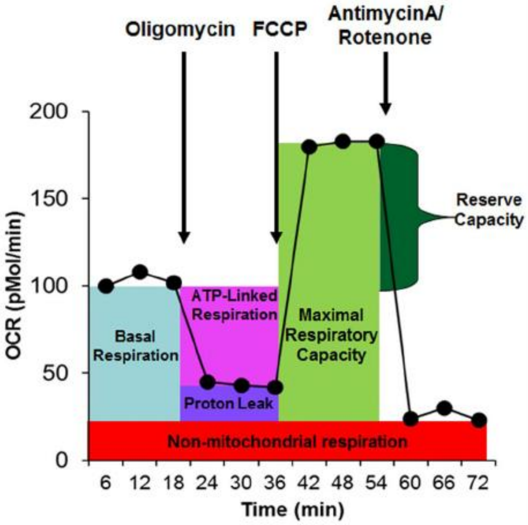

**Figure 3.2.11: Mitochondrial perturbations from the Seahorse Mitochondrial Stress Kit**. Oligomycin is used to separate ATP-linked respiration from proton leak. FCCP stimulates maximal respiration, and the antimycin A/rotenone cocktail gives non-mitochondrial oxygen consumption.

The Seahorse XF Analyzer reads specialized 96-well plates and quantifies oxygen concentration within cellular media. For this series of experiments, mitochondrial perturbation injections were administered at 20-minute intervals. It should be noted that this baseline measurement's timer started *after* the transit time between irradiator and start of the readout, which takes approximately ten minutes: five minutes to take the elevator from the WIMR basement to the sixth floor, and another five minutes to load the sample into the plate reader.

First, a baseline OCR measurement is obtained with no drug injection. 20 minutes after the start of the baseline measurement, an injection of mitochondrial complex III oligomycin is administered to obtain a measurement of ATP-coupled oxygen consumption and proton leak. Subsequently, an FCCP (carbonyl cyanide-4-triofluoromethoxy-phenylhydrazone) injection is administered to decouple oxygen consumption from ATP production. This decoupling allows the measurement of maximal respiratory capacity. Finally, an antimycin A/rotenone cocktail is administered (mitochondrial complex V and I inhibitor respectively) to provide a measurement of non-respirational oxygen consumption. A schematic of the effects of these drugs on OCR is depicted above in Figure 3.2.11.

### 3.2.6. Immunohistochemical staining

To measure HIF-1α expression, cells were plated in two separate eight-well chamber slides to have both a negative control and a 10 Gy dose of radiation. Thirty minutes following irradiation, the slides were washed three times with cold PBS and subsequently fixed in a 10-minute, cold acetone bath. Cells were then administered stain with Rabbit anti HIF-1α (ab2185, Abcam, Cambridge, UK), dilution 1:500 and Cy3 conjugated Goat-anti-Rabbit IgG (H+L) (111-167-003 Jackson ImmunoResearch Laboratories Inc., West Grove, PA, USA) 1:400 was the secondary antibody (red). Hoechst 33342, Sigma (3.75 mg/ml) dilution 1:3000 was used for nuclear staining (blue). Images were quantified using the FIJI (Fiji Is Just ImageJ) image analysis software package(*38*) to integrate HIF-1α intensity normalized to the number of nuclei in each field of view. The color channels in RGB images were split to allow for the application of intensity thresholds, and an intensity threshold also removed artifacts from the images. In all images, there were no counts observed in the green channel. Objects on the edges of images were excluded from quantification, and only objects 25 pixels in size or larger were considered in order to eliminate extracellular speckle.

To assess HIF-1 expression, HIF-1α concentration was used as a surrogate measurement. Cells were plated at 50-60% confluency in eight-well glass slides with four wells containing NOK cells and four wells containing T24 cells. Two such slides were plated (schematic shown in Figure 2.7.1), with one remaining untreated as a negative control, and the other receiving 10 Gy radiation. 30 minutes following radiation, cells were rinsed three times using cold Phosphate-Buffered Saline (PBS) to dilute and wash away excess cell media and subsequently fixed by submersion in an ice-cold acetone bath. *Note: it is absolutely essential to remove the slide walls prior to inundation in acetone because the acetone may deposit dissolved plastic on the slides as "coverslip" thus preventing antibody staining, and making imaging impossible.* Cells were then administered stain with Rabbit anti HIF-1α (ab2185, Abcam, Cambridge, UK), dilution 1:500 and Cy3 conjugated Goat-anti-Rabbit IgG (H+L) (111-167-003 Jackson ImmunoResearch Laboratories Inc., West Grove, PA, USA) 1:400 was the secondary antibody (red). Hoechst 33342, Sigma (3.75 mg/ml) dilution 1:3000 was used for nuclear staining (blue).

For image quantification, the Fiji (Fiji Is Just ImageJ) software package was employed to measure the HIF-1α intensity as a function of the number of nuclei in a field of view. An image of the Fiji software is depicted below in figure 3.2.12. An RGB is opened using File → Open and is subsequently split into three separate images (one for each color channel) under Image → Color → Split Channels so that intensity thresholding is possible. In the case of all the images for these experiments, the green channel remains blank, because the antibody stain fluoresces red, and the nuclear stain fluoresces blue. In this way, nuclei and HIF-1α in a given field of view may be visualized and distinguished.

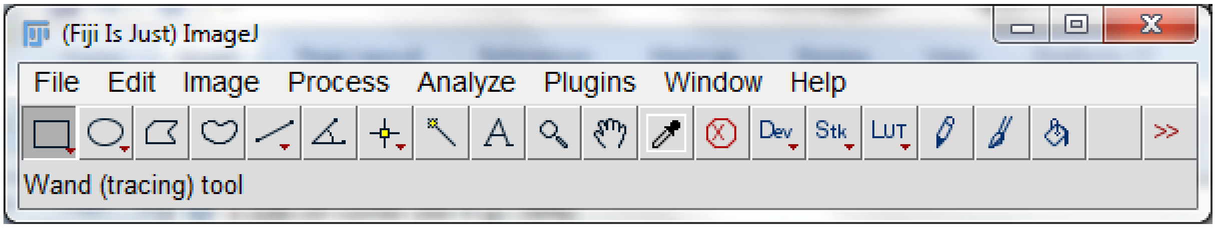

Wand (tracing) tool

**Figure 3.2.12: FIJI main panel**. All image analysis and manipulation tools can be accessed via the drop-down menus and the buttons on this simple panel. A search function for the directory of all functions can also be accessed via pressing Ctrl + L.

Following image splitting, an intensity threshold can be applied and adjusted to filter out speckle of the image as needed. A schematic of channel splitting is shown below in figure 3.2.13. This tool is located under Image → Adjust → Threshold. Careful thresholding is important, particularly for the nuclear counting, because of the close proximity of some cells, which may cause two nuclei to be counted as one when using the analyze particles function. Unfortunately, it is sometimes necessary to manually count nuclei; however, using a minimum size threshold in the analyze particles function may be utilized to locate nuclei that were "stuck together" efficiently thus preventing considerable tedium.

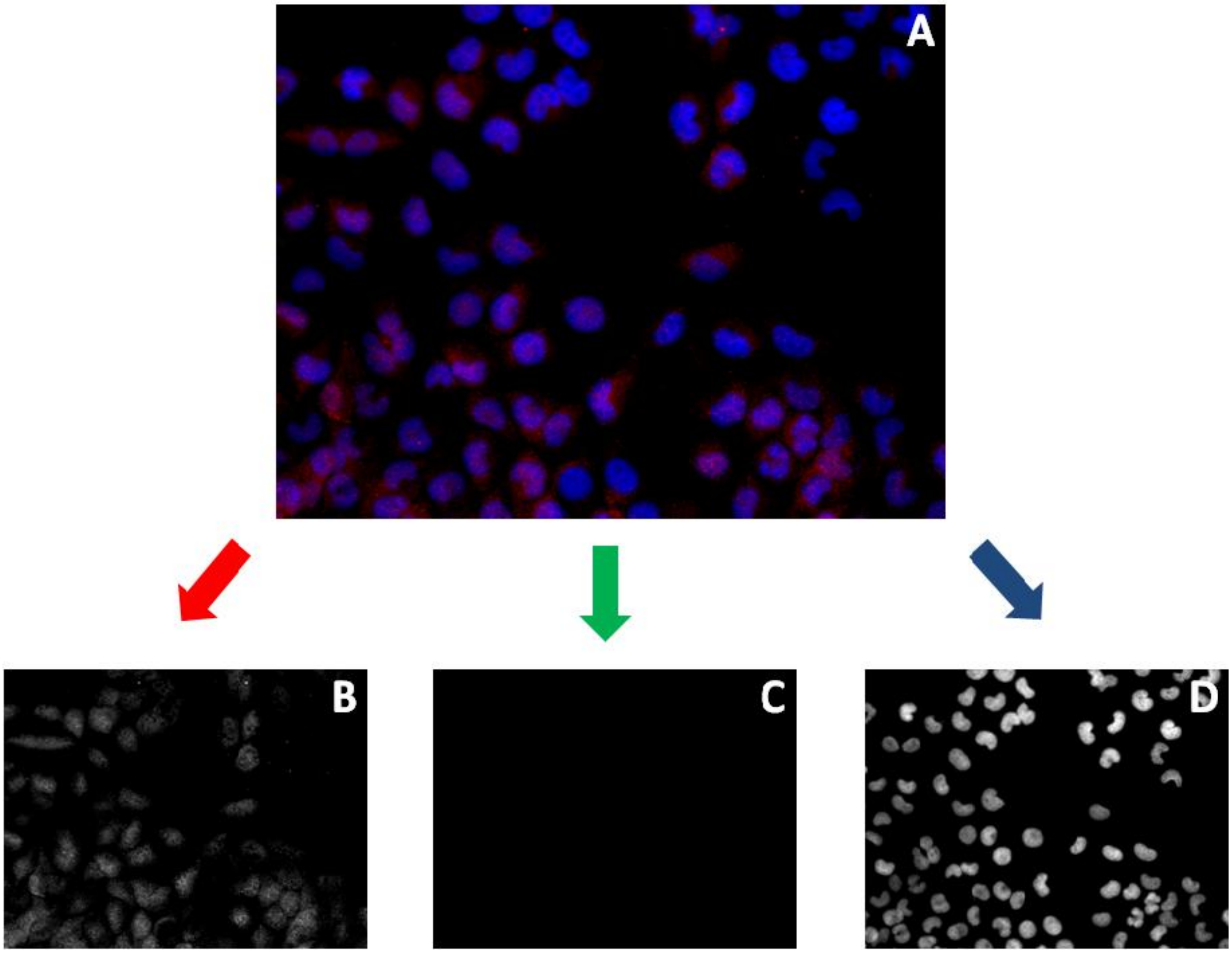

**Figure 3.2.13: Split-channel images**: An example image split into 3 channels; the color-coded arrows correspond to the respective color channels: B, red; C, green; D, blue. Note that the green channel (C) is empty because there is no green fluorescence.

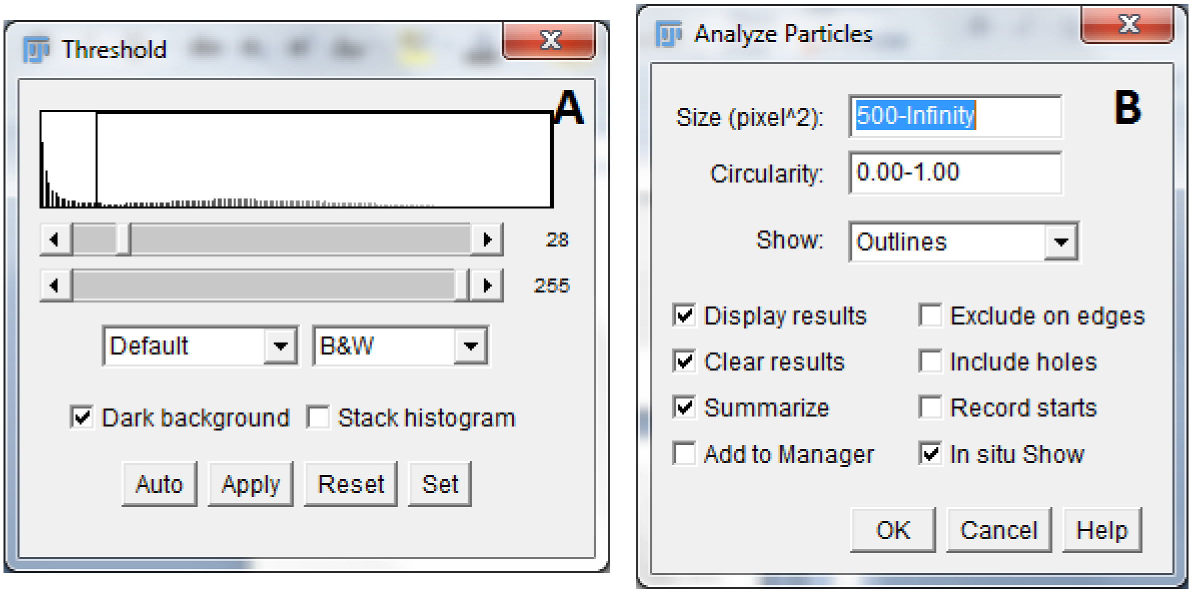

28

255

Default

B&W

☑ Dark background ☐ Stack histogram

Size (pixel^2): 500-Infinity

Circularity: 0.00-1.00

Show: Outlines

☑ Display results ☐ Exclude on edges

☑ Clear results ☐ Include holes

☑ Summarize ☐ Record starts

☐ Add to Manager ☑ In situ Show

**Figure 3.2.14: The Threshold and Analyze Particles tools**: The Threshold (A) and Analyze Particles tools (B) pictured. The threshold tool can be applied to create a mask of an image which filters out a minimum or maximum value denoted by the slides. The Analyze Particles tool allows for objects in an image mask to be measured by area which is tremendously useful while excluding objects of a minimum size. These functions are particularly useful for counting HIF-1α expression while excluding speckle via a minimum intensity and object size threshold.

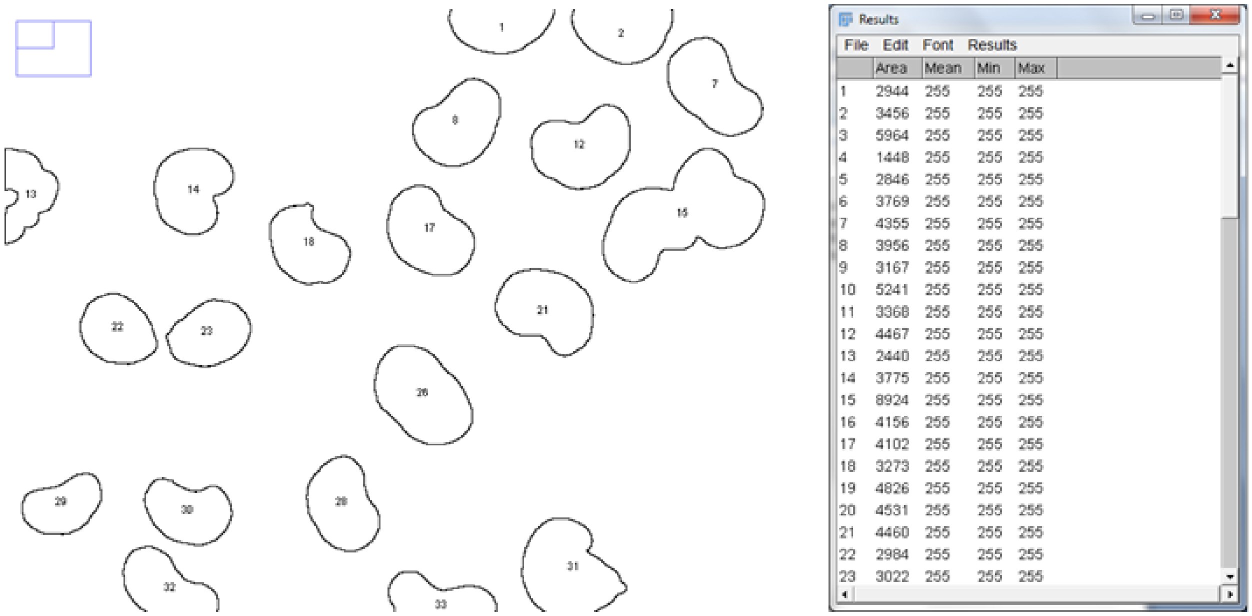

| | Area | Mean | Min | Max |
|---|---|---|---|---|
| 1 | 2944 | 255 | 255 | 255 |
| 2 | 3456 | 255 | 255 | 255 |
| 3 | 5964 | 255 | 255 | 255 |
| 4 | 1448 | 255 | 255 | 255 |
| 5 | 2846 | 255 | 255 | 255 |
| 6 | 3769 | 255 | 255 | 255 |
| 7 | 4355 | 255 | 255 | 255 |
| 8 | 3956 | 255 | 255 | 255 |
| 9 | 3167 | 255 | 255 | 255 |
| 10 | 5241 | 255 | 255 | 255 |
| 11 | 3368 | 255 | 255 | 255 |
| 12 | 4467 | 255 | 255 | 255 |
| 13 | 2440 | 255 | 255 | 255 |
| 14 | 3775 | 255 | 255 | 255 |
| 15 | 8924 | 255 | 255 | 255 |
| 16 | 4156 | 255 | 255 | 255 |
| 17 | 4102 | 255 | 255 | 255 |
| 18 | 3273 | 255 | 255 | 255 |
| 19 | 4826 | 255 | 255 | 255 |
| 20 | 4531 | 255 | 255 | 255 |
| 21 | 4460 | 255 | 255 | 255 |
| 22 | 2984 | 255 | 255 | 255 |
| 23 | 3022 | 255 | 255 | 255 |

**Figure 3.2.15: Example of counting in FIJI**: To the left is a zoomed in image with thresholding applied, and "show outlines" enabled. For reference, it is also the upper left hand corner of Figure 3.2.13D. To the right is the corresponding results of "Analyze Particles". Under "results" is the area of each particle as well as the mean, minimum, and maximum intensity. Because threshold post-processing was applied, the intensity was adjusted to saturation for every pixel, and therefore each pixel's intensity is set to be the maximum of 8-bit (255).

By enabling "Show: Outlines" in the Analyze Particles tool, each quantified particle is assigned a number which corresponds to the number shown in the image mask. This allows for rapid identification of the so-called "stuck together" particles. The threshold and analyze particle dialogue windows are pictured above in Figure 3.2.14A and B respectively. Similarly, for counting HIF-1α, thresholding and counting of the red channel are necessary. An intensity threshold of 25 and an object size threshold of 50 pixels$^2$ work well for images without excessive. 50 pixels$^2$ works well because it filters out objects with a radius of fewer than four pixels, thus removing extracellular speckle. Then the total area of the red pixels is summed and divided by the number of nuclei in the field of view. In this way, a HIF-1α metric is created: ΔHIF/nucleus which forms a basis for comparison. It is important to note that procedural consistency is critical because the measurements of HIF-1α expression are relative; therefore, it is theoretically possible to use "any" value, but filtering out the bottom 20% seemed to work well.

### 3.2.7. Clonogenic survival assay

Clonogenic survival of cells following radiation was conducted as previously described using a JL Shepherd Cesium-137 irradiator delivering a dose rate of approximately 400 cGy/min (*39*). Briefly, cells were plated at low density, irradiated, and after 10-15 days colonies containing more than 50 cells were counted and the surviving fraction calculated. Resulting data points were fit to a linear quadratic model. Each point represents the mean surviving fraction calculated from 6 replicates for each condition. Errors bars represent the standard deviation.

### 3.2.8. Statistical Analysis

Changes in $\tau_m$ from fluorescence lifetime imaging were assessed for statistical significance using an unpaired, two sample t-test in MATLAB software (The Mathworks, Inc., Natick, MA, USA). Differences in HIF-1α expression between irradiated and unirradiated cells were normalized to cell count in each field of view and were assessed for significance using an unpaired two-sample two-tailed t-test also in MATLAB. For assessment of clonogenic survival following irradiation, the curves were compared using the extra sum-of-squares F-test in GraphPad Prism version 6.0f (GraphPad Software Company, La Jolla, CA, USA).

## 3.3 Experimental Results

To characterize and demonstrate the metabolic effects of radiation on these representative cancerous and non-cancerous cells, we divided the two cell lines: the highly proliferative stable T24, and highly stable NOK into three experimental groups: untreated cells, control group cells treated with the mitochondrial inhibitor potassium cyanide (KCN), and cells treated with radiation. All cells were imaged using FLIM acquisition integrated over 120 seconds. We used mean fluorescence lifetime ($\tau_m$) as an indicator of metabolic shifts both before and after treatments and also assessed metabolism by measuring oxygen consumption rates utilizing the Seahorse assay. We also examined HIF-1α expression dynamics in response to radiation.

As expected, cells subjected to known mitochondrial inhibitors had significantly lower values for $\tau_m$ ($p < 0.001$). Figure 3.3.1 shows three sample images of T24 cells that were untreated (left), cyanide treated (center) or irradiated (right). When averaged over 35 different fields of view, T24 cells demonstrated a decrease in $\tau_m$ from 711.50 ± 52.65 ps ($n = 45$ for control group) to 638.08 ± 15.22 ps ($n = 40$, $p < 0.001$) when treated with the control drug KCN. This drop occurs because cyanide inhibits mitochondrial complex IV, and this inhibition results in a significant metabolic shift. When NOK cells were subjected to the same treatment with KCN, they showed a similar drop in $\tau_m$ from 789.57 ± 40.66 ps ($n = 45$ for control group) to 638.96 ± 31.92 ps ($n = 40$, $p < 0.001$).

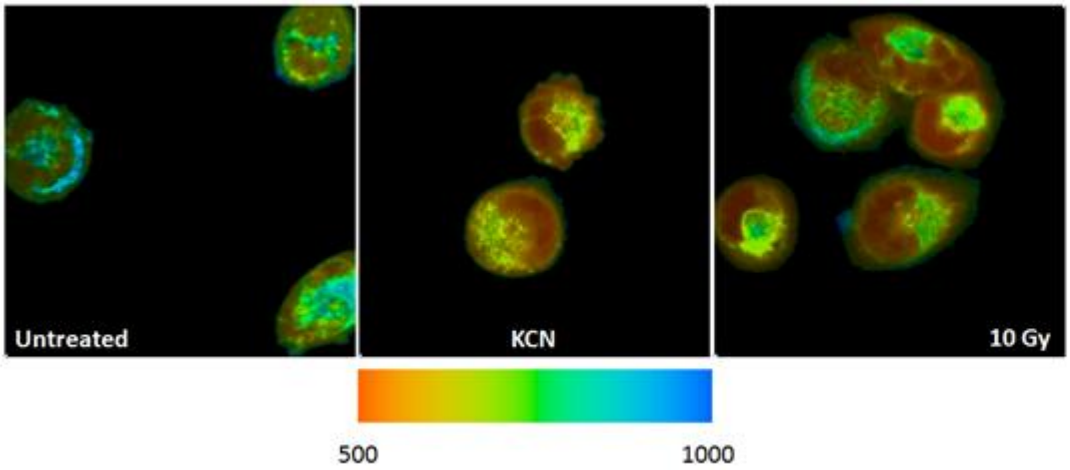

**Figure 3.3.1: Sample T24 FLIM images**: Sample FLIM images of T24 with $\tau_m$ in ps overlaid on each pixel in the field of view. Blue pixels represent longer $\tau_m$ values whereas red pixels represent shorter $\tau_m$. Mean lifetime decreases following either treatment of KCN or 10 Gy for the cancer cells.

We then measured the metabolic shift due to a large dose (as compared to standard clinical fraction dose) of radiation (10 Gy). T24 cells responded to radiation with a drop in $\tau_m$ from 711.50 ± 52.65 ps to 617.76 ± 13.68 ps similar to the mitochondrial inhibition therapy (see figure 3.3.2 and table 3.3.1). Conversely, NOK cells treated with 10 Gy of radiation demonstrated a change in $\tau_m$ from 789.57 ± 40.66 ps to 823.02 ± 38.26 ps ($n = 40$, $p < 0.001$). The non-cancerous NOK cells exhibit a small, but statistically significant, increase in $\tau_m$ metabolic signature as measured by FLIM resultant from radiation; whereas, the cancerous T24 cells show a much larger and directionally-opposite change in metabolic signature.

To understand local changes in oxygenation, we measured oxygen consumption rate (OCR) via the Seahorse XFe96 Analyzer of both irradiated and untreated cells. These data are presented in figure 3.3.3. The OCR dropped for both cells lines, as expected, following irradiation (*3*). From the oxygen consumption rates, it was clear that T24 cells were much more energetic than the comparatively less proliferative NOK cells. Furthermore, the resulting changes in oxygen consumption from radiation in T24 were much more dramatic. The first three points in the OCR curves are the measurements of basal respiration. Approximately 35 minutes following irradiation, mitochondrial complex V inhibitor oligomycin was added to halt oxygen consumption due to respiration. The rise in OCR at approximately 55 minutes is due to the administration of FCCP, which permeabilizes the mitochondrial membranes to stimulate maximal respiration. Finally, at approximately 80 minutes, rotenone (mitochondrial complex I inhibitor) was administered to shut down all mitochondrial activity. This allowed a measurement of oxygen consumption due to non-mitochondrial respiration.

It is particularly interesting to explore the OCR curves for T24. With no radiation, oxygen consumption dropped 573 pmol/min from 949 pmol/min 376 pmol/min (above 225

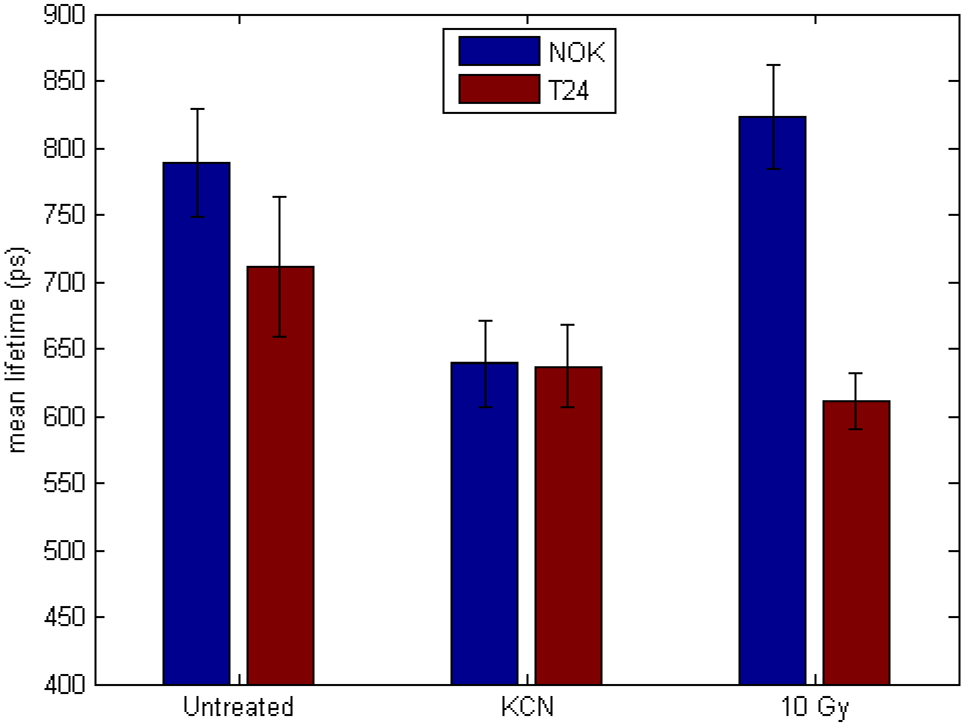

**Figure 3.3.2: T24 metabolism shifts following 10Gy radiation**: A graph comparing the mean lifetimes of NADH in NOK (blue) and T24 (maroon) cells before and after various treatments. Error bars are the standard deviations for each treatment group. Note the significant drop in $\tau_m$ for T24 cells following radiation. Again, of note are the trends within cell lines as opposed to baseline measurements.

| **Cell Line** | **untreated** | **KCN** | **10 Gy** |
|---|---|---|---|
| T24 | 711.50 ± 52.65 | 636.94 ± 30.40 | 610.95 ± 21.33 |
| NOK | 789.19 ± 40.57 | 638.96 ± 31.92 | 823.32 ± 38.26 |

**Table 3.3.1: Radiation affects T24 metabolic signature promptly**: The values for $\tau_m$ tabulated for T24 and NOK cells following treatment with KCN and radiation along with each distribution's standard deviation. There is a clear contrast in the cell lines' respective response to radiation. The intra-cell line trends are the key result as opposed to the different baseline $\tau_m$ values.

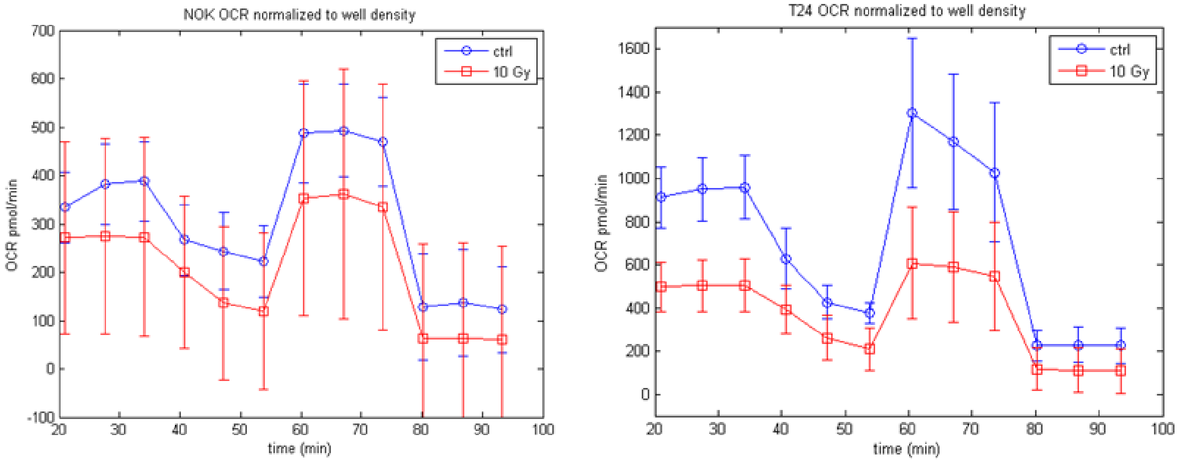

**Figure 3.3.3: Oxygen Consumption drops globally following irradiation**: Oxygen consumption rates for each cell group with control (blue line, circles), and irradiated (red line, squares). The vertical dashed lines indicate injection of a Mito Stress Kit reagents (i) oligomycin, (ii) FCCP and (iii) rotenone/antimycin A respectively. Note the difference in OCR scale between NOK and T24. This suggests that T24 cells are much more energetic as one might expect with more proliferative cells. Irradiation took place at t = 0, the intervening time was due to transport of the samples, and the mixing of solutions for each injection port.

pmol/min of non-mitochondrial respiration) when treated with oligomycin (ATP synthase inhibitor). When irradiated, oxygen consumption dropped 294 pmol/min from 502 pmol/min to 208 pmol/min (above 112 pmol/min of non-mitochondrial respiration). For NOK, with no irradiation, the drop in oxygen consumption was 145 pmol/min from 368 pmol/min to 223 pmol/min. With radiation, the drop was 154 pmol/min from 273 pmol/min to 119 pmol/min. This suggests that, for the cancer cells, there is a larger decrease in ATP production from respiration resultant from radiation when compared to the normal cells.

Ionizing radiation creates biological effect by creating reactive oxygen species and free radicals through the radiolysis of water molecules within the cells. These radicals and reactive oxygen species damage DNA by creating single-strand and double-strand breaks. Because previous studies (*40, 41*) have shown that free radicals stabilize HIF-1α and the key role HIF-1 plays in regulating metabolism, we measured the expression of HIF-1α in both NOK and T24 cells employing immunohistochemical staining via a HIF-1α antibody stain. Moreover, we observed metabolic signatures in response to radiation via FLIM of both cell lines when treated with radical scavenger glutathione (GSH), and HIF-1α inhibitor chrysin.

For the immunohistochemical staining, HIF-1α fluorescence is red in the images, and the nuclei are blue. From the sample images below, following radiation, it appears that HIF-1α expression increases for the T24 cells; however, no such increase is apparent in the NOK cells. It should be noted that the images in figure 3.3.4 account for considerably less than 0.1% of the total area analyzed.

The raw values for image quantification are given in the supplemental data. After averaging over four fields of view for each case, (NOK: untreated and 10 Gy, and T24: untreated

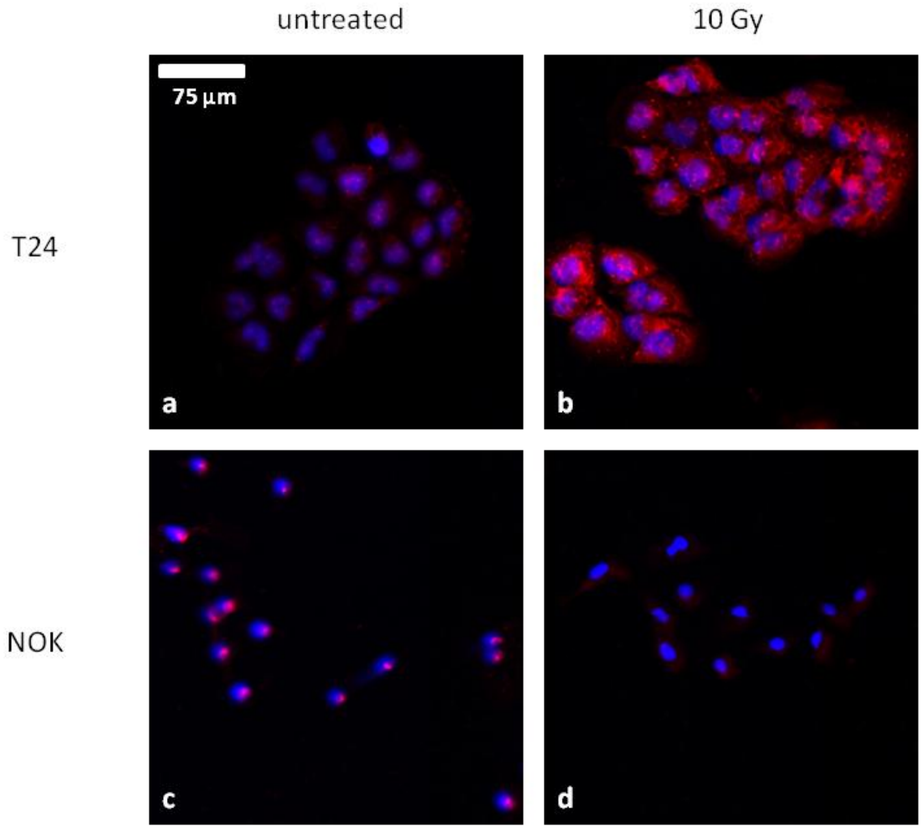

**Figure 3.3.4: Radiation increases HIF-1α expression drastically for T24**: A mosaic of slides stained for HIF-1α (red) and nuclei (blue) images *in vitro* of NOK and T24 both treated with 10 Gy of radiation and untreated. These images do not represent the same field of view. A minimum size threshold for objects of interest removed the speckle from image quantification.

and 10 Gy) the difference in HIF-1α expression following irradiation was found to be statistically significant between the cell lines ($p < 0.05$). NOK cells showed a decrease in HIF-1α expressions by approximately 40% following irradiation; conversely, for T24 cells, their HIF-1α expression per nucleus increased by 200% (see supplemental material). It was important to normalize raw HIF-1α pixel counts to the number of nuclei present in the field of view to account for variations in cell count in each field of view. For irradiated T24 malignant cells, metabolic signatures with decreased $\tau_m$ corresponded to an increase in HIF-1α expression, but in the NOK cells, a comparatively slight decrease in HIF-1α corresponded to little change in metabolic signature.

In the parallel FLIM study shown in figure 3.3.5, NOK cells treated with GSH only had an observed $\tau_m$ of $830.64 \pm 23.13$ ps, and NOK cells treated with GSH and 10 Gy had an observed $\tau_m$ of $821.67 \pm 37.26$ ps. This represents no statistically significant change ($n = 30$, $p > 0.05$). When treated with chrysin, only NOK cells had an observed $\tau_m$ of $722.38 \pm 21.77$ ps, and following irradiation, $\tau_m$ was observed to be $746.15 \pm 30.42$ ps (see figure 3.3.5a). For T24 cells treated with GSH only $754.73 \pm 28.63$ ps; following irradiation, $\tau_m$ was observed to be $753.43 \pm 23.66$ ps. When treated with chrysin only, T24 cells had an observed $\tau_m$ of $732.24 \pm 48.97$ ps; following irradiation, $\tau_m$ was observed to be $719.64 \pm 45.45$ ps. It should be noted that for T24 cells each paired treatment groups (control drug versus radiation and drug), the observed variations were not found to be statistically significant ($n = 30$, $p > 0.05$). However, the slight increase in $\tau_m$ for NOK following radiation was preserved in the case of control chrysin versus chrysin with concomitant radiation ($n = 30$, $p < 0.001$). Table 3.6.2 below gives a concise summary of all these values.

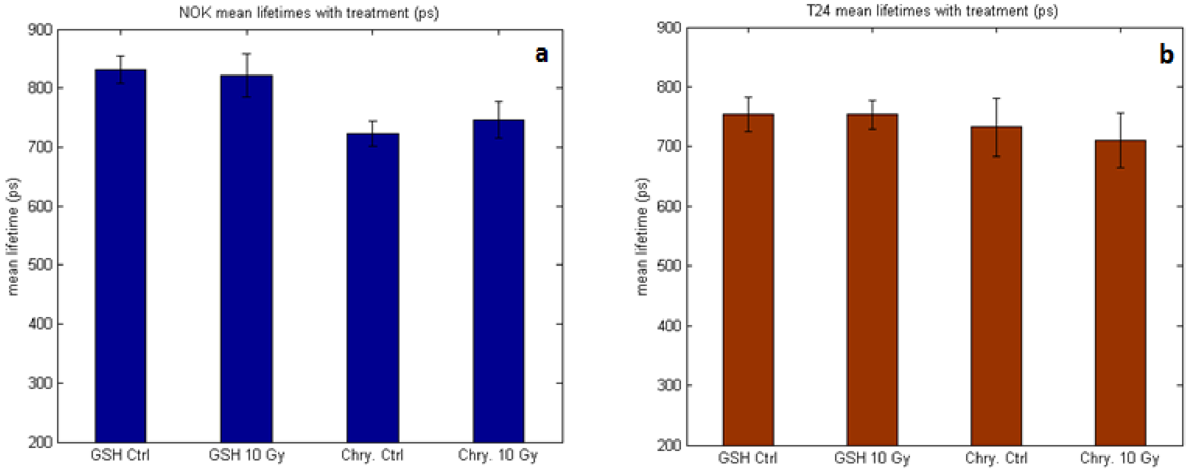

**Figure 3.3.5: Radical scavenging and HIF-1α inhibition suppress metabolic responses**: Shows the collected $\tau_m$ values for NOK cells (a in blue) and T24 cells (b in maroon) with control treatments, and treatments plus radiation (n = 30). Error bars shown are standard deviations of each treatment group. Note the consistency of the values between each treatment group.

| | NOK | | T24 | |
|---|---|---|---|---|
| | ctrl | 10 Gy | ctrl | 10 Gy |
| GSH | 830.64 ± 37.26 | 821.67 ± 37.26 | 754.64 ± 28.63 | 753.43 ± 23.66 |
| Chrysin | 722.38 ± 21.77 | 746.15 ± 30.42 | 732.24 ± 48.97 | 719.64 ± 45.45 |

**Table 3.3.2: GSH and Chrysin suppress metabolic response to radiation**: A list of each cell group's mean lifetime value reported with each population's standard deviation. Note that the only change that is statistically significant is for the 10 Gy + chrysin NOK cell group from its chrysin control ($p > 0 .05$).

Clonogenic survival was also evaluated for NOK and T24 cells in response to radiation to quantify radiosensitivity. These survival curves are given in figure 3.3.6. T24 cells are relatively radioresistant (approximately two decades of survival percentage) at high dose levels when compared to NOK cells ($p < 0.0001$).

## 3.4 Discussion & Conclusion

The present study demonstrates that these particular cell lines, NOK and T24, each exhibit distinct and prompt responses to radiation. The T24 cells showed a large change in metabolic signature whereas the NOK cells showed little metabolic response as measured by FLIM, and each within 30 minutes of treatment. The T24 cells' response to radiation when treated with a radical scavenger GSH was considerably muted. Moreover, when a HIF-1α inhibitor was administered, change in metabolic signature was similarly muted. Based on the evidence presented here, we suggest that an increase in HIF-1α expression in the T24 cells may be at least partially responsible for the observed changes in metabolic signatures.

Previous studies have shown that free radical creation from irradiation causes abnormal interactions with cellular signaling pathways (*42-44*). Note that ionizing radiation would induce a short-lived but spatially global spike in charges and free radicals to the tumor or cellular microenvironment. One of these interactions takes place with the protein Hypoxia-Inducible Factor 1 (HIF-1) (*40*). HIF-1 is a heterodimer consisting of HIF-1α and HIF-1β subunits; the HIF-1β subunit is independent of oxygen concentration. Under normoxia, the HIF-1α subunit is hydroxylated and subsequently degraded by the von Hippel-Lindau tumor suppressor protein (*45*). Consequently, the HIF-1 heterodimer does not form due to an insufficient concentration of HIF-1α.

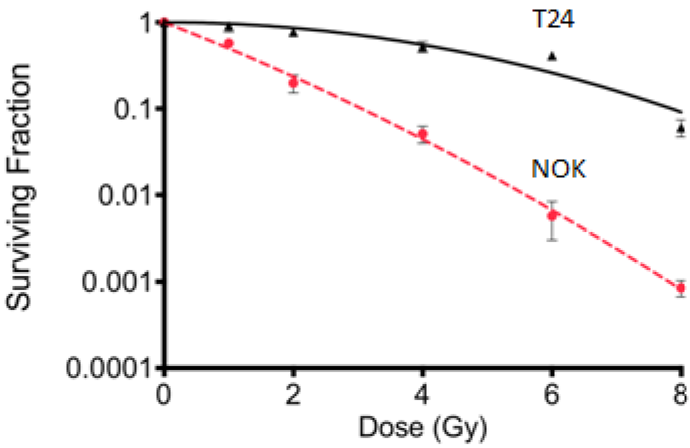

**Figure 3.3.6: NOK and T24 have significant radiosensitivity contrast**: Clonogenic survival over a range of radiation doses for immortalized keratinocyte (NOK, dashed line, circles) and head and neck squamous cell carcinoma (T24, solid line, triangles) cell lines (n = 6 per condition).

Chandel *et al.* (*40*) observed that reactive oxygen species and free radicals can stabilize HIF-1α allow the HIF-1 complex to form. Under these conditions, HIF-1 subsequently regulates a multitude of processes downstream. These processes include stimulation of angiogenesis and erythropoietin production, as well the regulation of glucose transport enzymes (*40, 43, 46-51*). The nature of HIF-1α gives it a key role in sensing cellular oxygen levels (*40, 52*). The free radicals produced by radiation can affect the cells in a multitude of ways including confounding cellular oxygen sensing and changing oxygen consumption rates.

As HIF-1 regulates glycolytic enzymes and glucose transport enzymes, it is reasonable to suggest that an increase in HIF-1α, and thus HIF-1, might result in metabolic switching. Indeed, the cells with stronger HIF-1 response to radiation (T24) showed a larger decrease in oxygen consumption when compared to NOK cells. This suggests that there may be an increase in aerobic glycolysis following irradiation for T24 cells that is not present in the NOK cells resultant from upregulated HIF-1 complex-driven signaling pathways. While the mechanism for this is outside the scope of this study, we show a clear correlation between metabolic switching and HIF-1α signaling. This correlation is particularly significant because tumors with upregulated HIF-1α have been associated with more aggressive phenotypes; these tumors are sometimes more metastatic (*50, 53-55*), and at times more radioresistant (*48*).

As shown in figure 3.3.6, the T24 cell line is relatively radioresistant when compared to the NOK cell line *in vitro* (*56, 57*). Interestingly, the more radioresistant cells were found to have changes in metabolic signature as measured by FLIM and also were found to have a great increase in HIF-1α expression following irradiation. It is possible that this increase in HIF-1α expression is a driving factor in the contrast in radiosensitivity between these two cell lines.

The correlation between HIF-1α expression and these FLIM-measured metabolic signatures shows FLIM's potential as a tool for assessing tumors' overall radiosensitivity and/or aggression of tumors. Moreover, these measurements show metabolic fluctuations that occur within thirty minutes, i.e. the timescale of a radiotherapy treatment. These metabolic fluctuations may be indicative of modulations in radiosensitivity *during* treatment or potentially for predicting radiosensitivity for the subsequent treatments. These types of measurements could be impactful, particularly for hypofractionated radiotherapy regimens which can be more sensitive to intrafraction dynamics (*58*). Future studies should focus on developing a deeper understanding of the mechanistic underpinning of these changes in metabolism such as incorporating FAD (Flavin Adenine Dinucleotide) fluorescence intensity imaging coupled to NADH intensity to measure potential fluxes in cellular redox ratio. Also, while *in vitro* models provide a tractable system in which it is possible to establish these changes, future studies should employ *in vivo* animal models to ensure the same trends are observed because other factors may influence metabolism during and after irradiation. Studies of this nature could grant a deeper understanding of the prompt biological effects of radiation on the tissue microenvironment and could be valuable in improving therapeutic regimens.

With the reported data and future studies to examine changes in metabolism due to radiation from a mechanistic and *in vivo* perspective, there also comes the great opportunity to consider future clinical ramification. Recently, there have been efforts to consider the role of dose both spatially and temporally and in the in context of the cellular response (*51, 59*). This study complements previously reported studies (*60-62*) by asserting that clinical use of radiation could be guided and improved by monitoring key cellular processes such as metabolism. Metabolism plays an important role of in cancer invasion and progression (*63-65*); therefore, metabolic profiling may have potential for guiding radiation therapy treatments in the future.

## 3.5 Supplemental Information

Table S3.5.1 shows the raw data used for immunohistochemical analysis of HIF-1α expression in NOK and T24. Because cells were fixed, it was necessary to collect data from each experimental group. These data do *not* represent "before and after" treatment. HIF-1α was quantified by counting objects with a minimum size of 25 pixels in the red channel. Nuclei were counted by summing the total number of discrete bodies in the blue channel. The number of red pixels was normalized to the number of nuclei to determine the change in HIF-1α per cell. These values were then averaged to make the statistical comparison. Propagation of uncertainty was used to calculate the error value for the ΔHIF/nucleus metric listed in the supplemental table.

## 3.6 Disclosure

Originally, this study was designed to have the following head and neck cell lines: UM-SCC-22B and NOK. These cell lines were initially chosen because head and neck cancer is a major research target of radiotherapy research. The cell lines were specifically chosen to have a high contrast of radiosensitivity, NOK being radiosensitive and UM-SCC-22B being radioresistant. Unfortunately, a year after the original paper was published, it has come to our attention that the cells our collaborators received were unintentionally mislabeled as 22B cells but were found, through genotyping, to be urothelial carcinoma cell line T24. While this is disappointing, due to the importance of head and neck cancer research, the specific findings of this study remain unchanged. The target of this study was to investigate differences in metabolic changes following irradiation between radiosensitive and radioresistant cells. The T24 cell line retains the study's high contrast of radiosensitivity with the T24 being radioresistant and NOK being radiosensitive. Furthermore, this study remains impactful because urothelial cancers are also important targets for radiotherapy.

| | NOK | | T24 | |
|---|---|---|---|---|
| | No RT | RT | No RT | RT |
| red pixels | 74855.5 | 70353 | 60323 | 262169.5 |
| Nuclei | 565 | 922.5 | 419 | 622 |
| Rp/Nuc | 129.71 ± 25.11 | 72.02 ± 23.42 | 144.39 ± 35.31 | 439.56 ± 68.29 |
| **ΔHIF/Nuc** | **0.56 ± 0.21** | | **3.04 ± 0.88** | |

**Table S3.5.1: T24 has a large increase in HIF-1α fluorescence following irradiation**: This table lists the average values for the image parameters for each field of view including the amount of number of red pixels (HIF-1α expression), etc. Statistical comparison was based on Rp/Nuc measure which is HIF-1α signal normalized to cell count. The error value for ΔHIF/Nuc was calculated by using propagation of uncertainty for a ratio.

## 3.7 References

*1.* Shaikh M, Burmeister J, Joiner M, Pandya S, Zhao B, Liu Q, Biological effect of different IMRT delivery techniques: SMLC, DMLC, and helical tomotherapy. Medical Physics 2010; 37, 762-70.

*2.* Hall EJ, Giaccia AJ, *Radiobiology for the Radiologist*. 7th ed. Philadelphia, PA: Wolters Kluwer Health; 2012.

*3.* Olive PL, Radiation-Induced Reoxygenation in the SCCVII Murine Tumor- Evidence for a Decrease in Oxygen-Consumption and an Increase in Tumor Perfusion. Radiotherapy and Oncology 1994; 32, 37-46.

*4.* Bussink J, Kaanders J, Rijken P, Raleigh JA, Van der Kogel AJ, Changes in blood perfusion and hypoxia after irradiation of a human squamous cell carcinoma xenograft tumor line. Radiation Research 2000; 153, 398-404.

*5.* Ljungkvist ASE, Bussink J, Kaanders J, Wiedenmann NE, Vlasman R, van der Kogel AJ, Dynamics of hypoxia, proliferation and apoptosis after irradiation in a murine tumor model. Radiation Research 2006; 165, 326-36.

*6.* Carlson DJ, Stewart RD, Semenenko VA, Effects of oxygen on intrinsic radiation sensitivity: A test of the relationship between aerobic and hypoxic linear-quadratic (LQ) model parameters. Medical Physics 2006; 33, 3105-15.

*7.* Palcic B, Skarsgard LD, Reduced Oxygen Enhancement Ratio at Low-Doses of Ionizing-Radiation. Radiation Research 1984; 100, 328-39.

*8.* Kim JW, Dang CV, Cancer's molecular sweet tooth and the Warburg effect. Cancer Research 2006; 66, 8927-30.

*9*. Lopez-Lazaro M, The Warburg effect: Why and how do cancer cells activate glycolysis in the presence of oxygen? Anti-Cancer Agents in Medicinal Chemistry 2008; 8, 305-12.

*10*. Upadhyay M, Samal J, Kandpal M, Singh OV, Vivekanandan P, The Warburg effect: Insights from the past decade. Pharmacology & Therapeutics 2013; 137, 318-30.

*11*. Warburg O, On the origin of cancer cells. Science 1956; 123, 309-14.

*12*. Guaragnella N, Giannattasio S, Moro L, Mitochondrial dysfunction in cancer chemoresistance. Biochemical Pharmacology 2014; 92, 62-72.

*13*. Suh DH, Kim HS, Kim B, Song YS, Metabolic orchestration between cancer cells and tumor microenvironment as a co-evolutionary source of chemoresistance in ovarian cancer: A therapeutic implication. Biochemical Pharmacology 2014; 92, 43-54.

*14*. Warmoes MO, Locasale JW, Heterogeneity of glycolysis in cancers and therapeutic opportunities. Biochemical Pharmacology 2014; 92, 12-21.

*15*. Blacker TS, Mann ZF, Gale JE, Ziegler M, Bain AJ, Szabadkai G, et al., Separating NADH and NADPH fluorescence in live cells and tissues using FLIM. Nat Commun 2014; 5, 9.

*16*. Digman MA, Caiolfa VR, Zamai M, Gratton E, The phasor approach to fluorescence lifetime imaging analysis. Biophysical Journal 2008; 94, L14-L16.

*17*. Schneckenburger H, Wagner M, Weber P, Strauss WSL, Sailer R, Autofluorescence lifetime imaging of cultivated cells using a UV picosecond laser diode. Journal of Fluorescence 2004; 14, 649-54.

*18*. Skala MC, Fontanella A, Lan L, Izatt JA, Dewhirst MW, Longitudinal optical imaging of tumor metabolism and hemodynamics. Journal of Biomedical Optics 2010; 15.

*19*. Stringari C, Geyfman M, Wang H, Crosignani V, Kumar V, Takahashi JS, et al., Circadian Metabolic Oscillations in the Epidermis Stem Cells by Fluorescence Lifetime Microscopy of NADH in Vivo. Biophysical Journal 2014; 106, 24A-24A.

*20*. Stringari C, Pate KT, Edwards RA, Waterman ML, Gratton E, Metabolic Imaging of Colon Cancer Tumors In Vivo by Phasor Fluorescence Lifetime Microscopy of NADH. Biophysical Journal 2013; 104, 342A-43A.

*21*. Conklin MW, Provenzano PP, Eliceiri KW, Sullivan R, Keely PJ, Fluorescence Lifetime Imaging of Endogenous Fluorophores in Histopathology Sections Reveals Differences Between Normal and Tumor Epithelium in Carcinoma In Situ of the Breast. Cell Biochemistry and Biophysics 2009; 53, 145-57.

*22*. Provenzano PP, Eliceiri KW, Keely PJ, Multiphoton microscopy and fluorescence lifetime imaging microscopy (FLIM) to monitor metastasis and the tumor microenvironment. Clin Exp Metastasis 2009; 26, 357-70.

*23*. Becker W, Fluorescence lifetime imaging - techniques and applications. Journal of Microscopy 2012; 247, 119-36.

*24*. Chance B, Metabolic Heterogeneities in Rapidly Metabolizing Tissues. Journal of Applied Cardiology 1989; 4, 207-21.

*25*. Lakowicz JR, Szmacinski H, Nowaczyk K, Johnson ML, Fluorescence Lifetime Imaging of Free and Protein-Bound NADH. Proceedings of the National Academy of Sciences of the United States of America 1992; 89, 1271-75.

*26*. Skala MC, Riching KM, Bird DK, Gendron-Fitzpatrick A, Eickhoff J, Eliceiri KW, et al., In vivo multiphoton fluorescence lifetime imaging of protein-bound and free nicotinamide adenine dinucleotide in normal and precancerous epithelia. Journal of Biomedical Optics 2007; 12.

27. Skala MC, Riching KM, Gendron-Fitzpatrick A, Eickhoff J, Eliceiri KW, White JG, et al., In vivo multiphoton microscopy of NADH and FAD redox states, fluorescence lifetimes, and cellular morphology in precancerous epithelia. Proceedings of the National Academy of Sciences of the United States of America 2007; 104, 19494-99.

28. Bird DK, Yan L, Vrotsos KM, Eliceiri KW, Vaughan EM, Keely PJ, et al., Metabolic mapping of MCF10A human breast cells via multiphoton fluorescence lifetime imaging of the coenzyme NADH. Cancer Research 2005; 65, 8766-73.

29. Wakita M, Nishimura G, Tamura M, Some Characteristics of the Fluorescence Lifetime of Reduced Pyridine-Nucleotides in Isolated Mitochondria, Isolated Hepatocytes, and Perfused Rat Liver In-Situ. Journal of Biochemistry 1995; 118, 1151-60.

30. Yaseen MA, Sakadzic S, Wu W, Becker W, Kasischke KA, Boas DA, In vivo imaging of cerebral energy metabolism with two-photon fluorescence lifetime microscopy of NADH. Biomedical Optics Express 2013; 4, 307-21.

31. Leppert J, Krajewski J, Kantelhardt SR, Schlaffer S, Petkus N, Reusche E, et al., Multiphoton excitation of autofluorescence for microscopy of glioma tissue. Neurosurgery 2006; 58, 759-+.

32. Walsh AJ, Cook RS, Manning HC, Hicks DJ, Lafontant A, Arteaga CL, et al., Optical metabolic imaging identifies glycolytic levels, subtypes, and early-treatment response in breast cancer. Cancer Res 2013; 73, 6164-74.

33. Sun Y, Phipps JE, Meier J, Hatami N, Poirier B, Elson DS, et al., Endoscopic Fluorescence Lifetime Imaging for In Vivo Intraoperative Diagnosis of Oral Carcinoma. Microscopy and Microanalysis 2013; 19, 791-98.

34. Schaue D, Ratikan JA, Iwamoto KS, Cellular Autofluorescence following Ionizing Radiation. Plos One 2012; 7, 7.

35. Brenner JC, Graham MP, Kumar B, Saunders LM, Kupfer R, Lyons RH, et al., Genotyping of 73 UM-SCC Head and Neck Squamous Cell Carcinoma Cell Lines. Head and Neck-Journal for the Sciences and Specialties of the Head and Neck 2010; 32, 417-26.

36. Wokosin DL, Squirrell JM, Eliceiri KW, White JG, Optical workstation with concurrent, independent multiphoton imaging and experimental laser microbeam capabilities. Rev Sci Instrum 2003; 74, 193-201.

37. Kueng W, Silber E, Eppenberger U, Quantification of  Cells Cultured on 96-Well Plates. Analytical Biochemistry 1989; 182, 16-19.

38. Schindelin J, Arganda-Carreras I, Frise E, Kaynig V, Longair M, Pietzsch T, et al., Fiji: an open-source platform for biological-image analysis. Nature Methods 2012; 9, 676-82.

39. Kimple RJ, Vaseva AV, Cox AD, Baerman KM, Calvo BF, Tepper JE, et al., Radiosensitization of Epidermal Growth Factor Receptor/HER2-Positive Pancreatic Cancer Is Mediated by Inhibition of Akt Independent of Ras Mutational Status. Clinical Cancer Research 2010; 16, 912-23.

40. Chandel NS, McClintock DS, Feliciano CE, Wood TM, Melendez JA, Rodriguez AM, et al., Reactive oxygen species generated at mitochondrial complex III stabilize hypoxia-

inducible factor-1 alpha during hypoxia - A mechanism of O-2 sensing. Journal of Biological Chemistry 2000; 275, 25130-38.

*41.* Guzy RD, Hoyos B, Robin E, Chen H, Liu LP, Mansfield KD, et al., Mitochondrial complex III is required for hypoxia-induced ROS production and cellular oxygen sensing. Cell Metabolism 2005; 1, 401-08.

*42.* Hirayama R, Ito A, Noguchi M, Matsumoto Y, Uzawa A, Kobashi G, et al., OH Radicals from the Indirect Actions of X-Rays Induce Cell Lethality and Mediate the Majority of the Oxygen Enhancement Effect. Radiation Research 2013; 180, 514-23.

*43.* Dewhirst MW, Relationships between Cycling Hypoxia, HIF-1, Angiogenesis and Oxidative Stress. Radiation research 2009; 172, 653-65.

*44.* Hernansanz-Agustin P, Izquierdo-Alvarez A, Sanchez-Gomez FJ, Ramos E, Villa-Pina T, Lamas S, et al., Acute hypoxia produces a superoxide burst in cells. Free Radic Biol Med 2014; 71, 146-56.

*45.* Ivan M, Kondo K, Yang HF, Kim W, Valiando J, Ohh M, et al., HIF alpha targeted for VHL-mediated destruction by proline hydroxylation: Implications for O-2 sensing. Science 2001; 292, 464-68.

*46.* Semenza GL, Expression of hypoxia-inducible factor 1: Mechanisms and consequences. Biochemical Pharmacology 2000; 59, 47-53.

*47.* Han Z-B, Ren H, Zhao H, Chi Y, Chen K, Zhou B, et al., Hypoxia-inducible factor (HIF)-1 alpha directly enhances the transcriptional activity of stem cell factor (SCF) in response to hypoxia and epidermal growth factor (EGF). Carcinogenesis 2008; 29, 1853-61.

48. Moeller BJ, Cao YT, Li CY, Dewhirst MW, Radiation activates HIF-1 to regulate vascular radiosensitivity in tumors: Role of reoxygenation, free radicals, and stress granules. Cancer Cell 2004; 5, 429-41.

49. Semenza GL, HIF-1 and tumor progression: pathophysiology and therapeutics. Trends Mol Med 2002; 8, S62-S67.

50. Vleugel MM, Greijer AE, Shvarts A, van der Groep P, van Berkel M, Aarbodem Y, et al., Differential prognostic impact of hypoxia induced and diffuse HIF-1 alpha expression in invasive breast cancer. Journal of Clinical Pathology 2005; 58, 172-77.

51. Meijer TWH, Kaanders JHAM, Span PN, Bussink J, Targeting Hypoxia, HIF-1, and Tumor Glucose Metabolism to Improve Radiotherapy Efficacy. Clinical Cancer Research 2012; 18, 5585-94.

52. Semenza GL, Hypoxia-inducible factor 1: Control of oxygen homeostasis in health and disease. Pediatric Research 2001; 49, 614-17.

53. Zhong H, De Marzo AM, Laughner E, Lim M, Hilton DA, Zagzag D, et al., Overexpression of hypoxia-inducible factor 1 alpha in common human cancers and their metastases. Cancer Research 1999; 59, 5830-35.

54. Halle C, Aarnes E-K, Holm R, Kristensen GB, Lyng H, HIF1 alpha signaling contributes to an aggressive hypoxic phenotype in cervical cancer. Cancer Research 2013; 73.

55. Lu X, Kang Y, Hypoxia and Hypoxia-Inducible Factors: Master Regulators of Metastasis. Clinical Cancer Research 2010; 16, 5928-35.

56. Kimple RJ, Smith MA, Blitzer GC, Torres AD, Martin JA, Yang RZ, et al., Enhanced Radiation Sensitivity in HPV-Positive Head and Neck Cancer. Cancer Research 2013; 73, 4791-800.

*57.* Park JW, Nickel KP, Torres AD, Lee D, Lambert PF, Kimple RJ, Human papillomavirus type 16 E7 oncoprotein causes a delay in repair of DNA damage. Radiotherapy and Oncology 2014; 113, 337-44.

*58.* Kirkpatrick JP, Cardenas-Navia LI, Dewhirst MW, Predicting the effect of temporal variations in Po-2 on tumor radiosensitivity. Int J Radiat Oncol Biol Phys 2004; 59, 822-33.

*59.* McCall KC, Barbee DL, Kissick MW, Jeraj R, PET imaging for the quantification of biologically heterogeneous tumours: measuring the effect of relative position on image-based quantification of dose-painting targets. Physics in Medicine and Biology 2010; 55, 2789-806.

*60.* Kissick MW, Campos D, Van Der Kogel A, Kimple RJ, On the importance of prompt oxygen changes for hypofractionated radiation treatments. Physics of Medicine and Biology 2013; 58, N279-85.

*61.* Crokart N, Jordan BF, Baudelet C, Ansiaux R, Sonveaux P, Gregoire V, et al., Early reoxygenation in tumors after irradiation: Determining factors and consequences for radiotherapy regimens using daily multiple fractions. Int J Radiat Oncol Biol Phys 2005; 63, 901-10.

*62.* Schoenfeld JD, Harris JR, Abbreviated course of radiotherapy (RT) for breast cancer. Breast 2011; 20, S116-S27.

*63.* Bredfeldt JS, Liu Y, Conklin MW, Keely PJ, Mackie TR, Eliceiri KW, Automated quantification of aligned collagen for human breast carcinoma prognosis. Journal of pathology informatics 2014; 5, 28-28.

*64*. Conklin MW, Eickhoff JC, Riching KM, Pehlke CA, Eliceiri KW, Provenzano PP, et al., Aligned Collagen Is a Prognostic Signature for Survival in Human Breast Carcinoma. American Journal of Pathology 2011; 178, 1221-32.

*65*. Glunde K, Imaging of collagen I fibers in primary breast cancer to predict metastasis. Amino Acids 2013; 45, 589-89.

# Chapter 4: Radiation affects cancer cell metabolism via ROS production and interaction with mitochondria *in vitro*

## 4.1 Introduction

Therapeutic strategies for treating cancers vary widely based on many factors like site or known genetic mutations. Surgery to remove tumor mass in tandem with adjuvant chemotherapy and radiation therapy are all considered standard practice. Radiation therapy is prescribed in over half of cancer therapeutic regimens (*1*), and many technological efforts to improve radiation therapy have been implemented. Intensity modulated radiotherapy (IMRT) has been instrumental in increasing dose uniformity as well as improving normal tissue sparing by allowing irradiation from multiple beam angles at different intensities. Conventional radiotherapy regimens involve daily dose "fractions" administered once per day, five days per week, to accumulate a total dose equal to the dose prescription. Technologies like RapidArc, TomoTherapy, TrueBeam, and stereotactic radiosurgery have greatly diversified the delivery techniques in the radiation therapy war chest for oncology practice (*2-5*). However, much of the effort in the advancement of radiation therapy has been limited to these aforementioned innovations improving dose distribution and exotic delivery techniques. Because radiation therapy plays such an important role cancer treatment, it is essential to gain an understanding of how radiation therapy impacts cell signaling and cellular organelles to gain a more fundamental understanding of radiosensitivity.

The classical treatment for radiation therapy is empirical fits to cell survival curves using the linear quadratic model (*6*). The model is simple but has been effective in describing radiation effects. The linear quadratic model assumes that deoxyribonucleic acid (DNA) damage takes place in single-hit events which are proportional to the dose delivered and multi-hit events are proportional to the dose delivered squared.

$$S = exp(-\alpha D - \beta D^2). \tag{4.1}$$

The most concise form of the linear quadratic equation upon which the linear quadratic model is based is shown in equation 4.1 where S is the surviving fraction of cells, D is the dose delivered and $\alpha$ and $\beta$ are coefficients of the curve fit. No simple model would be sufficient to characterize the complex interactions between radiation therapy and the microenvironment of a cell either normal or cancerous (*7-14*).

Chapter 3 describes a study which demonstrated that radiation has strong effects on metabolism, as measured by fluorescence lifetime imaging microscopy, that occur promptly within 30 minutes following irradiation *in vitro* (*15*). These changes occur well ahead of the time scale of any of the classical radiation effects described by the four 'R's of radiation therapy: repair, redistribution, reoxygenation and regrowth or cell death induced by replicative failure (*16*). These effects take place on a time scales from several hours to days after irradiation unlike the prompt effects observed in a recent study (*6*).

It is well known that available oxygen is a key modulator in the effectiveness of radiation therapy. Cell survival assays have determined that radiation is up to three times more effective at killing cells in well-oxygenated conditions versus hypoxic conditions. This effect, known as the oxygen enhancement effect, was quantified decades ago (*17, 18*) but recognized a century ago in the context of radium skin applicators. Oxygen is also a key player in cellular metabolic processes as the primary electron acceptor in the electron transport chain for ATP production via mitochondrial respiration. Metabolism and oxygen have a clear linkage which may have interplay with radiosensitivity concerns as pertaining to oxygen enhancement. Oxygen also impacts the availability of the HIF-1$\alpha$ subunit, and its ability to dimerize with HIF-1$\beta$ and regulate glycolytic and glucose transport enzymes down-stream (*19-21*). Therefore, it is useful to gain a deeper understanding of changes in cells following radiation, particularly in the context of metabolic changes.

Considering the potential relationship between metabolism, the HIF-1 complex, and radiosensitivity for radiotherapy, it makes sense to investigate potential consequences of radiation therapy on cellular metabolic infrastructure (*7, 10, 22, 23*). Of particular interest are changes in intrinsic mitochondrial ROS production from respiration, as well as signs of mitochondrial activity or inactivity, which can be measured via mitochondrial membrane polarization as a proxy. Therefore, in this study we present phasor analysis of Nicotinamide Adenosine Dinucleotide (NADH) fluorescence lifetime both before and following irradiation by a large dose of radiation (10 Gy) in both Normal Oral Keratinocytes (NOK) and urothelial carcinoma cells (T24). These cells were chosen because they have large contrast in intrinsic radiosensitivity with NOK being approximately 100-fold greater radiosensitivity as compared to T24 at large doses. Furthermore, we present comparative measurements of cellular ROS production for these cell lines. Quantification of cellular ROS production in these normal and cancer cells is supplemented with measurements of mitochondrial membrane potential to probe the function of mitochondria. Finally, expression of glycolytic enzyme Hexokinase II is quantified.

## 4.2 Methods and Materials

### 4.2.1. Cell Culture

Two human cell lines with significant differences radiosensitivity were selected from a panel of cell lines. T24 urothelial carcinoma cells were cultured in DMEM with 4.5 g/dl glucose, 10% FBS, 1% hydrocortisone, penicillin (100 units/ml), streptomycin (100 mg/ml). Normal oral keratinocytes (NOK) cells were a kind gift of Dr. Karl Munger of Tufts University, and cultured in keratinocyte serum-free media supplemented with both EGF and Bovine Pituitary Extract. Cells were maintained as monolayer cultures at 37°C in a humidified atmosphere with 5% $CO_2$.

### 4.2.2. Cellular Irradiation

Cells were irradiated to 10 Gy using a 320 kVp small animal and cell culture irradiator XRAD 320 (Precision X-ray Inc). The XRAD 320 has a metal ceramic anode with 1.5 mm Al + 0.25 mm Cu + 0.75 mm Sn of beam filtration. Each well was plated with 200 µL of cellular media. For negative controls, all 96 well plates were read out with no treatment drug or irradiation. Cells were plated to be 50% and 90% confluent on a 96-well (8 rows, 12 columns) black-walled plate to prevent fluorescence leakage between wells.

### 4.2.3. Fluorescence Lifetime Imaging of Cellular NADH

Time-correlated Fluorescence Lifetime Imaging Microscopy (FLIM) was performed using a custom multiphoton laser-scanning microscope with SPC-830 Becker Hickl FLIM hardware (*24*, *25*) at the Laboratory for Optical and Computational Instrumentation LOCI, University of Wisconsin – Madison, USA. Fluorescence of cellular NADH was excited using multiphoton excitation at a wavelength of 740 nm utilizing a Spectra Physics MaiTai Ti:Sapphire laser. FLIM was employed to map the NADH-based metabolism of cell lines *in vitro* subjected to different treatment conditions. Five regions of interest per dish were imaged 30 minutes following radiation, and during imaging, cells were maintained at 37°C and 5% $CO_2$ in a LiveCell™ stage top incubator. A 450/70 nm emission bandpass filter (Semrock) was utilized to isolate the NADH autofluorescence. See section 2.2.3 for more detailed information.

### 4.2.4. Cellular Reactive Oxygen Species Production

**Figure 4.2.1: Plate map for ROS fluorescence measurement**: A map for how this series of ROS measurements was conducted. Two plates were read out to obtain a sham and an irradiated condition. It is standard for cell plates to be lettered by row and numbered by column. Rows A-D are plated with NOK cells and rows E-H are plated with T24 cells. Not depicted in the map is that columns 11 and 12 are left unplated, to get background measurements without cells, whereas rows C, D, G and H are plated from columns 1-10 but not administered dye.

To measure the cellular production of ROS, NOK and T24 cells were plated as shown in Figure 4.2.1 to 90% confluency in clear-bottomed, black-wall 96-well plates. DCFDA (dichlorofluorescein-diacetate) dye is commonly used to monitor cellular ROS because cellular esterases remove the acetyl groups and allow the activation of fluorescent capability of DCF by oxidation reactions with cellular ROS. Immediately before use, chloromethyl-$H_2$DCFDA (Abcam, San Francisco, CA, USA) was dissolved in dimethyl sulfoxide (DMSO) to a 1 mM stock concentration. The dye was further diluted in PBS to yield a final cell loading concentration of 5 μM. Cells were incubated at 37°C and 5% $CO_2$ with the DCFDA dye loaded dye for 10 minutes for cellular update per the protocol included.

Before treatment, cellular media was removed via aspiration and each well was rinsed with warm PBS to remove excess dye and administered 100 µL of phenol-red free media. One plate was subjected to sham irradiation and the other was dosed to 10 Gy radiation. After radiation exposure, the cells were immediately placed on a fluorescent plate reader (SpectraMax i3, Molecular Devices, CA, USA) and total well fluorescence determined using excitation 495 nm (bandwidth 9 nM) and emission 525 nm (bandwidth 15 nM). Fluorescence intensity was read before and immediately after irradiation (approximately 2 minutes for transit time between the irradiator and the plate reader), and at 15, 30, 45, 60, 75 and 90 minutes following irradiation. These measurements were then plotted using MATLAB (The Mathworks, Inc., Natick, MA, USA) and compared between plates and cell groups.

### 4.2.5. Cellular Mitochondrial Membrane Potential

Mitochondrial membrane potential (MMP) was measured using a TMRE (tetramethylrhodamine ethyl ester) MMP measuring kit (Abcam - ab113852). TMRE dye is an effective method to measure mitochondrial membrane polarization because it is positively charged and therefore is readily taken up by active mitochondria which have a negative electric potential. The TMRE was diluted to 1 µM in DMSO per manufacturer suggestion for well-plate readout. 50 µM FCCP (carbonyl cyanide 4-trifluoromethoxyphenylhydrazone) was administered as a control drug because it uncouples ATP production from respiration and prevents mitochondrial accumulation of fluorophores. Cells were incubated with TMRE for 20 minutes at 37 °C and read out using a multi-well plate reader (SpectraMax i3, Molecular Devices, CA, USA) at 549 nm excitation and 575 emission. Cells were again plated to 90% confluency in clear-bottomed, black-walled 96-well plates as shown below in Figure 4.2.2.

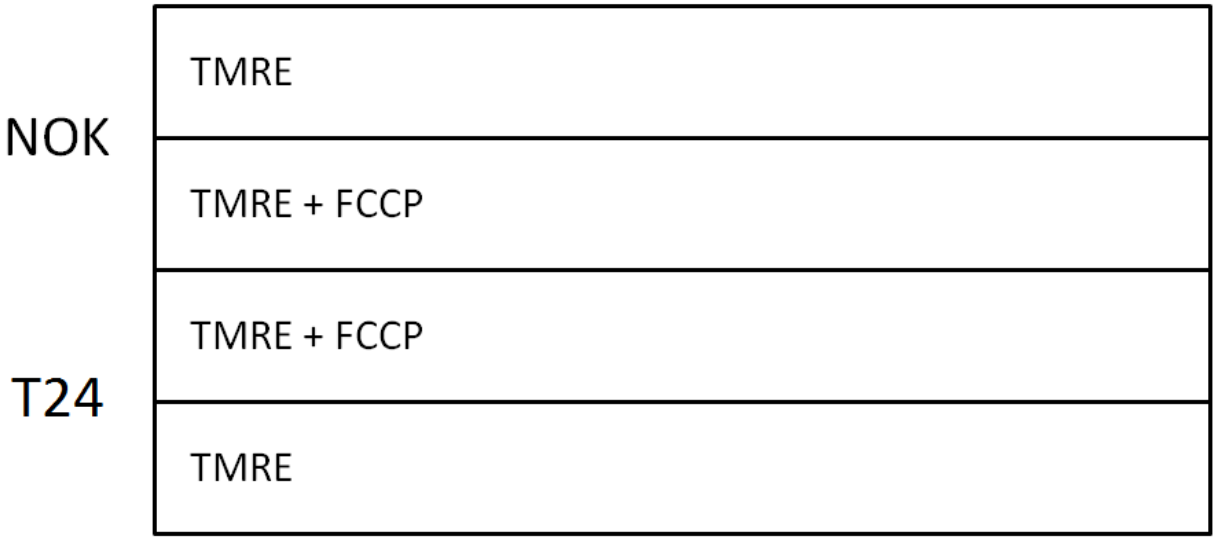

**Figure 4.2.2: Plate map for mitochondrial membrane polarization fluorescence measurement**: A map for how this series of mitochondrial membrane potential measurements was conducted. Two plates were read out to obtain a sham and an irradiated condition. It is standard for cell plates to be lettered by row and numbered by column. Rows A-D are plated with NOK cells and rows E-H are plated with T24 cells. Not depicted in the map is that columns 11 and 12 are left unplated, to obtain background fluorescence measurements.

FCCP was added to rows C-F (the rows annotated with TMRE+FCCP in figure 4.2.2) to a final concentration of 10 µM and incubated at 37°C and 5% $CO_2$ for 10 minutes. Then TMRE was added to the media to a final concentration of 1 µM and FCCP coctail and incubated for 15 minutes again at 37°C and 5% $CO_2$. After incubation, the drug and dye coctail was removed via aspiration and cells were subsequently washed with warm PBS, and given 100 µL of phenol red-free media. After radiation exposure, the cells were immediately placed on a fluorescent plate reader (SpectraMax i3, Molecular Devices, CA, USA) and total well fluorescence determined using excitation 549 nm (bandwidth 9 nM) and emission 575 nm (bandwidth 15 nM).

Similar to the ROS experiments, two plates were necessary: one sham and one for irradiation to evaluate the radiation response. Again, fluorescence intensity was assessed immediately following radiation, and then at time points of 15, 30, 45, 60, 75 and 90 minutes after the radiation dose.  These measurements were also plotted using MATLAB (The Mathworks, Inc., Natick, MA, USA) and compared between plates and cell groups.

### 4.2.6. Cellular Expression of Hexokinase-II

Expression of cellular hexokinase-II was quantified using the Western Blot technique. NOK and T24 cells were plated to 90% confluency in eight separate 6 cm culture dishes: four for NOK and four for T24.  Cell media was removed via aspiration before freezing to remove all liquid from the dishes to avoid ice crystals.  These fixations were performed before irradiation, and then at 30 minutes, 6 hours and 24 hours following irradiation to track the accumulation of HK-II.

Following treatment, cells were lysed with RIPA lysis buffer (10 mM Tris-Cl (pH 8.0), 1 mM EDTA, 1% Triton X-100, 0.1% sodium deoxycholate, 0.1% SDS, 140 mM NaCl, 1 mM PMSF) and were sonicated. Equal amounts of protein were analyzed by SDS-PAGE (35 mg), and then the proteins were transferred to polyvinylidene difluoride (PVDF) membranes, analyzed by specific primary antibodies, and detected via incubation with IRDye® secondary antibodies and subsequent imaging on the Odyssey Fc (LI-COR).

The primary antibodies used were:

Control 1: GAPDH (D16H11) XP® Rabbit mAb #5174 Cell signaling technologies

Control 2: α-Tubulin (DM1A) Mouse mAb #CP06 Calbiochem

HK-II: polyclonal Anti-Hexokinase II Picoband$^{TM}$ #A01389 BOSTER biological technology.

The secondary antibodies used were:

IRDye 800CW Goat anti-Rabbit LI-COR

IRDye 800RD Goat anti-mouse LI-COR.

## 4.3 Experimental Results

To investigate changes in metabolism, we performed phasor analysis of NADH FLIM of NOK and T24 as depicted in figure 4.3.1. No appreciable change in metabolism was observed following irradiation for NOK cells. This is in contrast with T24 cells which do show a significant metabolic impact. Both cell types responded similarly to mitochondrial perturbation by mitochondrial complex IV blocker, potassium cyanide. It should be noted that the metabolic signature of T24 cells do not lie on the line between negative control and mitochondrial control (KCN). This lack of co-linearity suggests that the metabolic change in T24 cells may not be due to changes in oxidative phosphorylation.

To quantify changes in cellular ROS production, we measured fluorescence of DCFDA, which is plotted in figure 4.3.2. NOK cells showed a significant uptick in ROS production following irradiation. This increase in ROS production was not observed for T24 cells, which remained relatively constant. There was no statistically significant change in ROS concentration for T24 following irradiation. It should be noted that NOK has a less predictable growth rate than T24 cells, and therefore differences in confluency may manifest after cell growth over two nights. This may account for the increased variance in fluorescence intensity of NOK ROS. Furthermore, radiation had only a small impact on mitochondrial membrane polarization dropping only by approximately 10% as pictured in figure 4.3.3. However, when subjected to control drug FCCP, NOK mitochondrial showed a marked decrease in fluorescence intensity of

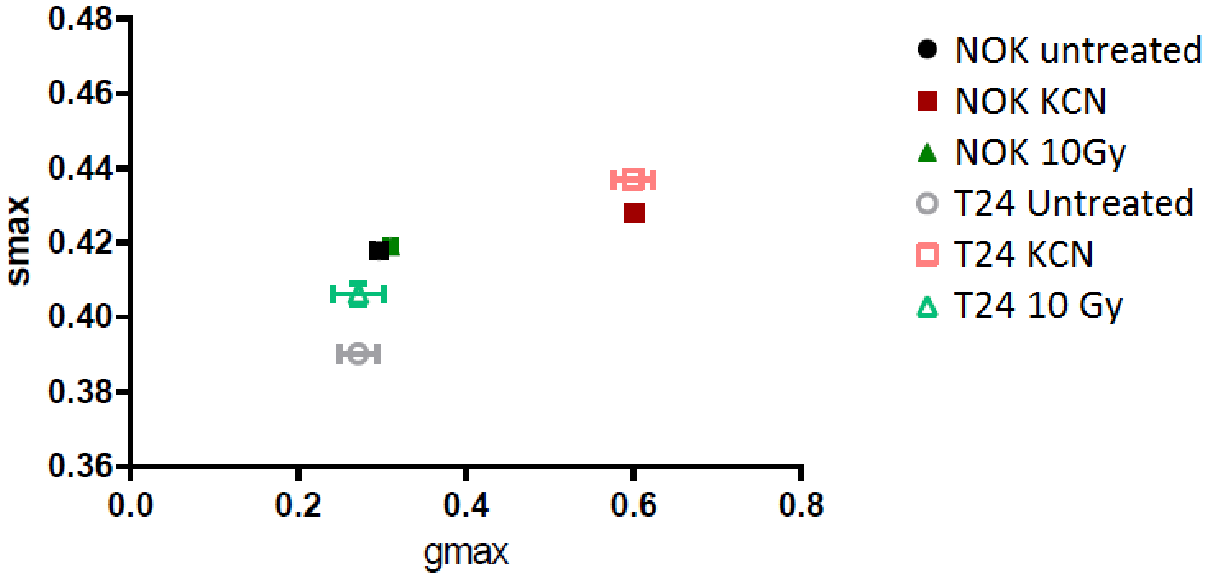

**Figure 4.3.1: Radiation-induced metabolic changes in T24 are non-mitochondrial**: A plot of gmax vs smax as determined by phasor analysis of NADH FLIM data for NOK and T24. KCN, a mitochondrial complex IV inhibitor is used as a metabolic control drug. Interestingly, the data does not show mitochondrial inhibition as the likely effect of irradiation for either cell line.

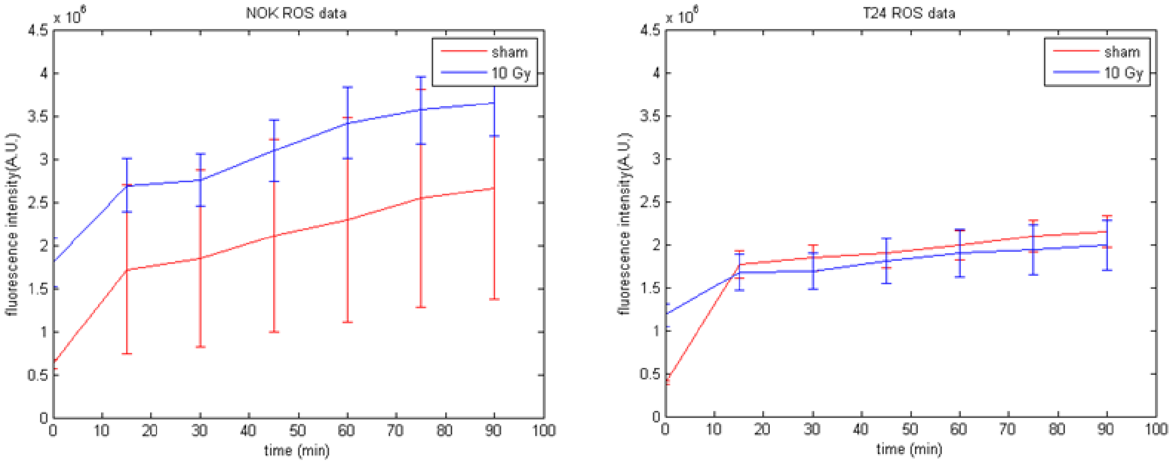

**Figure 4.3.2: NOK has increased ROS production following irradiation**: Cellular ROS production as measured by fluorescence intensity of DCFDA plotted against time following sham irradiation (red) and a 10 Gy dose of irradiation (blue).

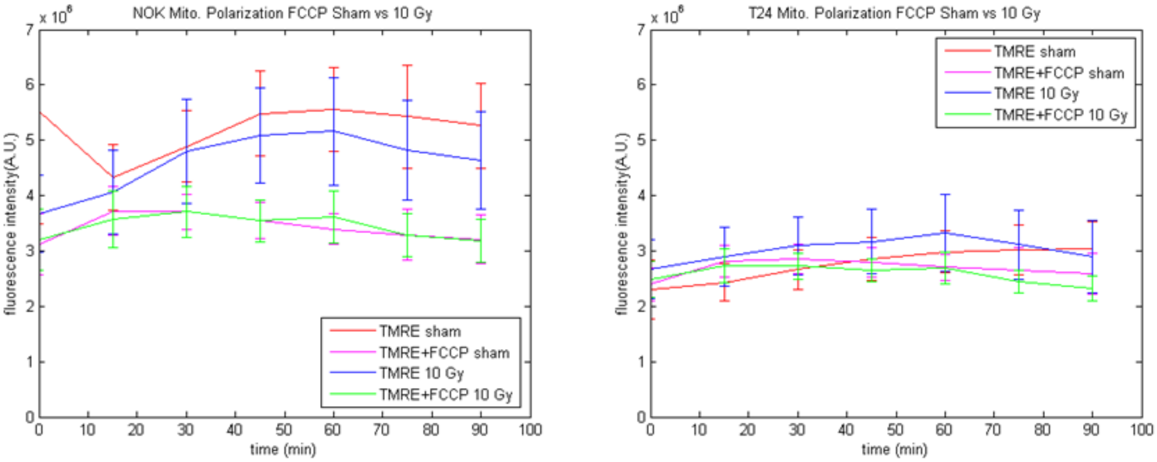

**Figure 4.3.3: T24 mitochondrial membrane polarization unchanged by radiation**: Mitochondrial membrane polarization as measured by fluorescence intensity of TMRE sequestered by active mitochondria. These data are plotted against time following sham irradiation (red) and a 10 Gy dose of irradiation (blue).

TMRE. The behavior of T24 is strikingly different; there is no statistically significant change in mitochondrial membrane polarization for either the irradiated cells or the sham cells.

Finally, expression of HK-II was quantified via Western Blot before irradiation and then 0.5, 6 and 24 hrs following irradiation. Figure 4.3.4 compares HK-II expression in the NOK and T24 cells. It was observed that HK-II expression was significantly lower in the case of NOK cells than in T24 cells as shown in Figure 4.3.4. The original Western Blot image is included in the supplemental material, (figure S4.5.1).

## 4.4 Discussion

Incident ionizing radiation induces a flood of free radicals that create reactive oxygen species (ROS) such as: superoxide, hydroxyl and peroxyl radicals when interacting with water in cells. It is these ROS that inflict biological damage rather than the paltry amount of energy absorption imparted by incident radiation. For a dose prescription of 60 Gy to a tumor with a mass of two grams, the energy deposited is mere 0.12 J -- an insignificant amount of energy. Therefore, radiation therapy may be perhaps more correctly regarded as free radical therapy. These ROS and free radical species generated by interactions between water molecules and organic fragments with energetic electrons chemically interact with the entire cell, damaging organelles such as mitochondria (*9, 26*). These ROS also break DNA strands which require the activation of DNA repair machinery, which in cancers may be faulty. Moreover, other damage to genetic information may occur such as alkylation of DNA strands. Upon accumulation, these epigenetic changes may eventually lead to replicative failure upon serial cell division. In addition to DNA damage, oxidative stress causes many changes in normal cellular processes, which can lead to the activation of apoptotic pathways (*8, 9, 14, 27*). However, particularly in

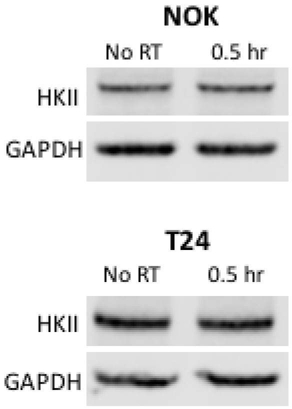

**Figure 4.3.4: T24 expresses significantly more HK-II than NOK**: Western blot data for Hexokinase-II expression in NOK and T24 cells. It is interesting to note that the concentration of HK-II is much higher for T24 cells versus NOK.

cancers, these prolonged stresses can result in the selection for adaptive responses, such as metabolic reprogramming and circumvention of cell-death machinery (*8*, *28*-*30*).

Indeed, phasor data of NADH fluorescence lifetime data in Figure 4.3.1 indicate that a prompt change is induced by irradiation of the cancerous, radioresistant T24 cells within 30 minutes, but not in benign, radiosensitive NOK cells. The data indicate that in T24 cells, free NADH concentration is increased. This effect is somewhat surprising because one might expect that the radiosensitive cells would show a response; however, the opposite effect is observed. However, one of the consequences of HK-II upregulation is the bolstering of cellular radical-scavenging defenses via pentose phosphate pathway production of NADPH (*31*). It is possible that the initial spike of radiation-induced ROS was mitigated by elevated concentrations of NADPH in the radioresistant T24 cells. It is important to note that the metabolic signature observed for T24 following irradiation does not lie on the line between negative control and mitochondrial perturbation using KCN, which indicates that the change in metabolic signature may not be mitochondrial in origin (*32*).

The net products of glycolysis of one molecule of glucose are shown in Equation 4.2.

$$Glucose + \ 2NAD^{+} \ \rightarrow 2\,Pyruvate + 2\,ATP + 2\,NADH. \qquad (4.2)$$

In this reaction, two units of ATP are expended (not shown on left-hand side) to generate four ATP molecules for a *net* gain of two molecules of ATP. Also important is the generation of two pyruvate molecules by lactase dehydrogenase as the principle reactant for the Tricarboxylic Acid Cycle (TCA) or Krebs cycle for oxidative phosphorylation. Finally, it should be noted that two molecules of NAD$^{+}$ are reduced to two equivalents of free NADH. Therefore, it stands to reason that in the case of T24 cells, the origin of the change in metabolic signature to higher free NADH population lies in increased glycolytic activity.

TMRE fluorescence measurements of mitochondrial membrane polarization also showed a very interesting effect. In the case of NOK cells, a slight decrease in polarization following irradiation was observed, but not a down to the level of FCCP control achieved in both the irradiated and sham cases. Conversely, TMRE fluorescence of T24 mitochondria was not changed for cells irradiated cells, or for either case when treated with FCCP. The lack of change in mitochondrial membrane polarization indicates that the effect of radiation on these cells' metabolic signature as measured by FLIM in T24 are non-mitochondrial in origin.

A previous study by our group demonstrated that HIF-1α expression increased by 300% in T24 cells following irradiation. Conversely, NOK cells showed a slight decrease in HIF-1α expression (*15*). It is somewhat counter-intuitive, then, that NOK cells demonstrate a significant increase in ROS production in NOK cells, whereas their cancerous T24 counterparts show no statistically significant change in cellular ROS levels. This is surprising because ROS and free radicals produced by irradiation have been previously linked to stabilization of HIF-1α, which plays a key role in cellular responses to hypoxia (*33*). However, it should be noted that oxygen concentration and ROS levels are not the only mechanisms by which HIF-1α may be stabilized, loss-of-function of the VHL being an obvious one mechanism. Another example an oxygen-independent stabilizer of HIF-1α is the accumulation of TCA cycle intermediates, which interfere with the function of HIF prolyl hydroxylases thus preventing the "flagging" of HIF-1α for ubiquitination and subsequent destruction (*34-36*). When the HIF-1 heterodimer forms, it serves as a transcription factor for glucose transport enzymes, the hexokinase family of glycolytic enzymes, and pro-angiogenic signaling as well (*37-39*).

Hexokinase-II is a transcription target of HIF-1 and is found to be over-expressed in many cancers (*40, 41*). Moreover, in these two cell lines, there is a higher concentration of HK-II present in T24 cells as compared to NOK cells. HK-II is advantageous for cells that are actively proliferating because it has two active catalytic binding sites for glucose-phosphorylation which improves its glucose turnover potential (*42-44*). This is particularly advantageous because it allows for energy production without the loss of carbon skeletal components needed for proliferation and anaplerosis. Moreover, HK-II activation has been correlated with protection against injury and death because of its ability to associate with the outer mitochondrial membrane as well as its antioxidant defense bolstering properties (*31, 41, 45, 46*).

These data all fit together to suggest that the comparatively radioresistant T24 cells promptly respond with a measureable shift in metabolic signature indicating an increase in free NADH population. The increase in HK-II expression in concert with the lack of change in mitochondrial ROS or mitochondrial membrane potential suggests that this increase in free NADH may be the result of an increase in glycolysis. Indeed, HK-II's role in cell death machinery, as well as antioxidant defense, further suggests that the capacity for prompt response may modulate treatment response. Most critically, the response occurs on the same time scale as the duration of a hypofractionated or stereotactic radiotherapy treatment. These effects occur well ahead of cell death and may play a role in modulating treatment efficacy *during* treatment.

## 4.5 Conclusion

Radiation therapy has been a crucial tool in the practice of oncology and is prescribed in therapeutic regimens for a multitude of cancer types and applications. Because of its prevalence, it is important to gain a deeper understanding of the host of biological effects induced. These effects are manifold and much more complex than can be accounted for in the simplistic linear quadratic model (*47*). Sublethal damage to DNA and cell kill are merely a subset of the effects created by radiation therapy: these other effects include changes in perfusion and oxygenation (*16, 48*, *49*), changes in vasculature and angiogenesis (*50*), and even prolonged injuries to organelles due to oxidative stress (*8, 9, 19*). Radiation therapy is also not subject to interstitial fluid pressures and perfusion issues that affect drug-based cancer treatments (*51*).

A deeper understanding of metabolic changes induced by irradiation and their mechanistic underpinnings provides an opportunity to enhance our grasp on what factors impact and modulate radiosensitivity. Furthermore, aberrant metabolism is known to play a key role in both cancer progression and metastatic aggression. It is the authors' opinion that to advance radiotherapy efficacy, it is desirable to understand its impact on cellular signaling and metabolic changes that may occur not only between fractions, but also during fractions. The timescale of these effects is particularly important in the context of hypofractionated treatment regimens which limit therapeutic opportunity to average over dynamic effects due to fewer fractions (*47, 52*, *53*). A deeper understanding of interplay between these phenomena may provide opportunities to tailor therapeutic regimens to be more patient-specific based on their cancer metabolic profiles and improve its adaptability in future treatment regimens.

## 4.6 Supplemental material

The original image of the Western Blot for HK-II is provided below in figure S4.6.1. The figure was cropped so that data for HK-II expression from NOK was above data from T24. This was done so that the figure 4.3.4 would be consistent in the order of listing the cell lines with NOK being first and T24 being second. Also, figure 4.3.4 lists the expression following 30 minutes because it is the most relevant timescale to the rest of the data presented in this work.

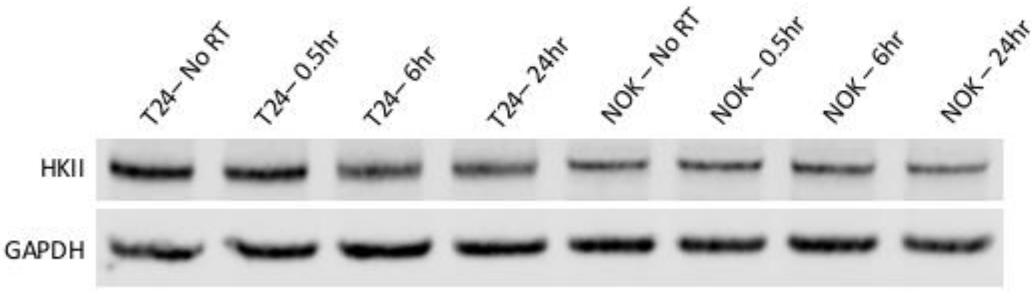

**Figure S4.6.1: Full Western Blot image of HK-II for T24 and NOK**: The full image of the Western blot of Hexokinase-II expression in NOK and T24 cells. Figure 4.4 is comprised of the data for NOK - NO RT, NOK - 0.5 hr, T24 - No RT, and T24 - 0.5 hr. These data are rearranged to follow the format of other figures where NOK cells are listed first.

## 4.7 References

1. Society AC, Cancer Facts & Figures 2016. Place American Cancer Society: American Cancer Society; 2016.
2. Mackie TR, Holmes T, Swerdloff S, Reckwerdt P, Deasy JO, Yang J, et al., Tomotherapy - A New Concept for the Delivery of Dynamice Conformal Radiotherapy. Medical Physics 1993; 20, 1709-19.
3. Mackie TR, Holmes TW, Reckwerdt PJ, Yang J, Tomotherapy - Optimized Planning and Delivery of Radiation-Therapy. Int J Imaging Syst Technol 1995; 6, 43-55.
4. Lagerwaard FJ, Verbakel W, van der Hoom E, Slotman BJ, Senan S, Volumetric modulated arc therapy (RapidArc) for rapid, non-invasive stereotactic radiosurgery of multiple brain metastases. Int J Radiat Oncol Biol Phys 2008; 72, S530-S30.
5. Otto K, Volumetric modulated arc therapy: IMRT in a single gantry arc. Medical Physics 2008; 35, 310-17.
6. Hall EJ, Giaccia AJ, *Radiobiology for the Radiologist*. 7th ed. Philadelphia, PA: Wolters Kluwer Health; 2012.
7. Alexandrou AT, Li JJ, Cell Cycle Regulators Guide Mitochondrial Activity in Radiation-Induced Adaptive Response. Antioxid Redox Signal 2014; 20, 1463-80.
8. Azzam EI, Jay-Gerin JP, Pain D, Ionizing radiation-induced metabolic oxidative stress and prolonged cell injury. Cancer Lett 2012; 327, 48-60.
9. Morales A, Miranda M, Sanchez-Reyes A, Biete A, Fernandez-Checa JC, Oxidative damage of mitochondrial and nuclear DNA induced by ionizing radiation in human hepatoblastoma cells. Int J Radiat Oncol Biol Phys 1998; 42, 191-203.

*10.* Nguyen V, Gaber MW, Sontag MR, Kiani MF, Late effects of ionizing radiation on the microvascular networks in normal tissue. Radiation Research 2000; 154, 531-36.

*11.* Roth NM, Sontag MR, Kiani MF, Early effects of ionizing radiation on the microvascular networks in normal tissue. Radiation Research 1999; 151, 270-77.

*12.* Sunar U, Makonnen S, Zhou C, Durduran T, Yu G, Wang H-W, et al., Hemodynamic responses to antivascular therapy and ionizing radiation assessed by diffuse optical spectroscopies. Optics Express 2007; 15, 15507-16.

*13.* Yamamori T, Yasui H, Yamazumi M, Wada Y, Nakamura Y, Nakamura H, et al., Ionizing radiation induces mitochondrial reactive oxygen species production accompanied by upregulation of mitochondrial electron transport chain function and mitochondrial content under control of the cell cycle checkpoint. Free Radic Biol Med 2012; 53, 260-70.

*14.* Yoshida T, Goto S, Kawakatsu M, Urata Y, Li T-S, Mitochondrial dysfunction, a probable cause of persistent oxidative stress after exposure to ionizing radiation. Free Radical Research 2012; 46, 147-53.

*15.* Campos D, Peeters W, Nickel K, Burkel B, Bussink J, Kimple RJ, et al., Radiation Promptly Alters Cancer Live Cell Metabolic Fluxes: An In Vitro Demonstration. Radiation Research 2016; 185, 496-504.

*16.* Bussink J, Kaanders J, Rijken P, Raleigh JA, Van der Kogel AJ, Changes in blood perfusion and hypoxia after irradiation of a human squamous cell carcinoma xenograft tumor line. Radiation Research 2000; 153, 398-404.

*17.* Palcic B, Skarsgard LD, Reduced Oxygen Enhancement Ratio at Low-Doses of Ionizing-Radiation. Radiation Research 1984; 100, 328-39.

*18.* Gray LH, Conger AD, Ebert M, Hornsey S, Scott OCA, The Concentration of Oxygen Dissolved in Tissues at the Time of Irradiation as a Factor in Radiotherapy. The British Journal of Radiology 1953; 26, 638-48.

*19.* Dewhirst MW, Relationships between Cycling Hypoxia, HIF-1, Angiogenesis and Oxidative Stress. Radiation research 2009; 172, 653-65.

*20.* Stroefer M, Jelkmann W, Metzen E, Brockmeier U, Dunst J, Depping R, Stabilisation and Knockdown of HIF - Two Distinct Ways Comparably Important in Radiotherapy. Cellular Physiology and Biochemistry 2011; 28, 805-12.

*21.* Dewhirst MW, Cao Y, Moeller B, Cycling hypoxia and free radicals regulate angiogenesis and radiotherapy response. Nat Rev Cancer 2008; 8, 425-37.

*22.* D. Campos WP, K. Nickel, B. Burkel, J. Bussink, R. Kimple, A. Van Der Kogel, K. Eliceiri, M. Kissick, Radiation Induces Live-Cell Metabolic Fluxes: an in-vitro Demonstration. AAPM Annual Meeting. Place Medical Physics: Medical Physics; 2016.

*23.* Fenton BM, Lord EM, Paoni SF, Effects of radiation on tumor intravascular oxygenation, vascular configuration, development of hypoxia, and clonogenic survival. Radiation Research 2001; 155, 360-68.

*24.* Provenzano PP, Eliceiri KW, Keely PJ, Multiphoton microscopy and fluorescence lifetime imaging microscopy (FLIM) to monitor metastasis and the tumor microenvironment. Clin Exp Metastasis 2009; 26, 357-70.

*25.* Wokosin DL, Squirrell JM, Eliceiri KW, White JG, Optical workstation with concurrent, independent multiphoton imaging and experimental laser microbeam capabilities. Rev Sci Instrum 2003; 74, 193-201.

*26.* Yakes FM, VanHouten B, Mitochondrial DNA damage is more extensive and persists longer than nuclear DNA damage in human cells following oxidative stress. Proceedings of the National Academy of Sciences of the United States of America 1997; 94, 514-19.

*27.* Assaly R, d'Anglemont de Tassigny A, Paradis S, Jacquin S, Berdeaux A, Morin D, Oxidative stress, mitochondrial permeability transition pore opening and cell death during hypoxia-reoxygenation in adult cardiomyocytes. European Journal of Pharmacology 2012; 675, 6-14.

*28.* Chandel NS, McClintock DS, Feliciano CE, Wood TM, Melendez JA, Rodriguez AM, et al., Reactive oxygen species generated at mitochondrial complex III stabilize hypoxia-inducible factor-1 alpha during hypoxia - A mechanism of O-2 sensing. Journal of Biological Chemistry 2000; 275, 25130-38.

*29.* Chen S, Sang N, Hypoxia-Inducible Factor-1: A Critical Player in the Survival Strategy of Stressed Cells. Journal of Cellular Biochemistry 2016; 117, 267-78.

*30.* Gramaglia D, Gentile A, Battaglia M, Ranzato L, Petronilli V, Fassetta M, et al., Apoptosis to necrosis switching downstream of apoptosome formation requires inhibition of both glycolysis and oxidative phosphorylation in a BCL-X-L- and PKB/AKT-independent fashion. Cell Death Differ 2004; 11, 342-53.

*31.* McCommis KS, Douglas DL, Krenz M, Baines CP, Cardiac-specific Hexokinase 2 Overexpression Attenuates Hypertrophy by Increasing Pentose Phosphate Pathway Flux. Journal of the American Heart Association 2013; 2.

*32.* Ma N, Digman MA, Malacrida L, Gratton E, Measurements of absolute concentrations of NADH in cells using the phasor FLIM method. Biomedical Optics Express 2016; 7, 2441-52.

*33*. Hervouet E, Cizkova A, Demont J, Vojtiskova A, Pecina P, Hal N, et al., HIF and reactive oxygen species regulate oxidative phosphorylation in cancer. Carcinogenesis 2008; 29, 1528-37.

*34*. Hewitson KS, Lienard BMR, McDonough MA, Clifton IJ, Butler D, Soares AS, et al., Structural and mechanistic studies on the inhibition of the hypoxia-inducible transcription factor hydroxylases by tricarboxylic acid cycle intermediates. Journal of Biological Chemistry 2007; 282, 3293-301.

*35*. Koivunen P, Hirsila M, Remes AM, Hassinen IE, Kivirikko KI, Myllyharju J, Inhibition of hypoxia-inducible factor (HIF) hydroxylases by citric acid cycle intermediates - Possible links between cell metabolism and stabilization of HIF. Journal of Biological Chemistry 2007; 282, 4524-32.

*36*. Selak MA, Armour SM, MacKenzie ED, Boulahbel H, Watson DG, Mansfield KD, et al., Succinate links TCA cycle dysfunction to oncogenesis by inhibiting HIF-alpha prolyl hydroxylase. Cancer Cell 2005; 7, 77-85.

*37*. Semenza GL, Expression of hypoxia-inducible factor 1: Mechanisms and consequences. Biochemical Pharmacology 2000; 59, 47-53.

*38*. Semenza GL, HIF-1: upstream and downstream of cancer metabolism. Current Opinion in Genetics & Development 2010; 20, 51-56.

*39*. Semenza GL, HIF-1 and tumor progression: pathophysiology and therapeutics. Trends Mol Med 2002; 8, S62-S67.

*40*. Marin-Hernandez A, Gallardo-Perez JC, Ralph SJ, Rodriguez-Enriquez S, Moreno-Sanchez R, HIF-1 alpha Modulates Energy Metabolism in Cancer Cells by Inducing

Over-Expression of Specific Glycolytic Isoforms. Mini-Rev Med Chem 2009; 9, 1084-101.

41. Suh DH, Kim MA, Kim H, Kim M-K, Kim HS, Chung HH, et al., Association of overexpression of hexokinase II with chemoresistance in epithelial ovarian cancer. Clinical and Experimental Medicine 2014; 14, 345-53.

42. Roberts DJ, Miyamoto S, Hexokinase II integrates energy metabolism and cellular protection: Akting on mitochondria and TORCing to autophagy. Cell Death Differ 2015; 22, 248-57.

43. Tsai HJ, Wilson JE, Functional organization of mammalian hexokinases: Both N- and C-terminal halves of the rat type II isozyme possess catalytic sites. Archives of Biochemistry and Biophysics 1996; 329, 17-23.

44. Wilson JE, Isozymes of mammalian hexokinase: structure, subcellular localization and metabolic function. Journal of Experimental Biology 2003; 206, 2049-57.

45. Sun L, Shukair S, Naik TJ, Moazed F, Ardehali H, Glucose phosphorylation and mitochondrial binding are required for the protective effects of hexokinases I and II. Mol Cell Biol 2008; 28, 1007-17.

46. Rasola A, Bernardi P, The mitochondrial permeability transition pore and its adaptive responses in tumor cells. Cell Calcium 2014; 56, 437-45.

47. Kissick MW, Campos D, Van Der Kogel A, Kimple RJ, On the importance of prompt oxygen changes for hypofractionated radiation treatments. Physics of Medicine and Biology 2013; 58, N279-85.

*48*. Olive PL, Radiation-Induced Reoxygenation in the SCCVII Murine Tumor- Evidence for a Decrease in Oxygen-Consumption and an Increase in Tumor Perfusion. Radiotherapy and Oncology 1994; 32, 37-46.

*49*. Orlowski K, Rohrer Bley C, Zimmermann M, Vuong V, Hug D, Soltermann A, et al., Dynamics of tumor hypoxia in response to patupilone and ionizing radiation. PloS one 2012; 7, e51476-e76.

*50*. Moeller BJ, Cao YT, Li CY, Dewhirst MW, Radiation activates HIF-1 to regulate vascular radiosensitivity in tumors: Role of reoxygenation, free radicals, and stress granules. Cancer Cell 2004; 5, 429-41.

*51*. Multhoff G, Vaupel P, Radiation-induced changes in microcirculation and interstitial fluid pressure affecting the delivery of macromolecules and nanotherapeutics to tumors. Frontiers in oncology 2012; 2, 165-65.

*52*. Kirkpatrick JP, Brenner DJ, Orton CG, The linear-quadratic model is inappropriate to model high dose per fraction effects in radiosurgery. Medical Physics 2009; 36, 3381-84.

*53*. Kirkpatrick JP, Cardenas-Navia LI, Dewhirst MW, Predicting the effect of temporal variations in Po-2 on tumor radiosensitivity. Int J Radiat Oncol Biol Phys 2004; 59, 822-33.

# Chapter 5:  Conclusions and Future Work

## 5.1 General conclusions

### 5.1.1. Restatement of specific aims

The aim of this work was to gain a deeper understanding of how radiation therapy affects the biological system and how those effects may impact the efficacy of radiation therapy itself. Oxygen is a key modulator of radiosensitivity, and clearly, metabolism plays an important role in oxygen consumption and availability. To evaluate these effects, **we quantified changes in cellular metabolism and HIF-1 signaling following irradiation** in both a radiosensitive (NOK) and radioresistant (T24) cell line. To probe the mechanistic underpinning of these metabolic changes in these two cell lines following irradiation, we **assessed changes in mitochondrial membrane polarization and ROS production as well as expression of HK-II**, a HIF-1 transcription target.

### 5.1.2. Radiation affects cellular metabolism *promptly*

One of the key findings of this work is that radiation induces detectable and quantifiable metabolic changes within thirty minutes of irradiation. It should be noted that the thirty minute time window was imposed on the study because of the physical distance between the cabinet irradiator in the small animal facility of the Wisconsin Institute for Medical Research and the microscopy facility at Laboratory for Optical and Computational Instrumentation. Indeed, the changes observed may well have occurred faster than the thirty minutes elapsed. Therefore, these prompt changes in metabolism occur on timescales well before the effects of the 4 R's of radiobiology: repair, redistribution, reoxygenation, and repopulation. Moreover, these effects are classically be attributed to the impact of cell death and how that death affects the consumption of oxygen. The data presented show that these effects also depend on cell type, and may instead be related to a fifth 'R,' intrinsic radiosensitivity.

In particular, this work investigates how two distinct cell lines – one cancerous (T24) and one non-cancerous (NOK) -- respond metabolically to a large dose of radiation. These two cell lines possess significantly different radiosensitivities with T24 cells have a two decade survival advantage over NOK cells at 10 Gy. Interestingly, the data presented in this work show that the radioresistant T24 cell line that shows a strong metabolic response. This is in stark contrast to the non-cancerous NOK cells where there is no statistically significant observable change in metabolic signature following irradiation. Again, it is important to note that the changes observed in the cancerous T24 cells manifest themselves within thirty minutes of irradiation. This is a critical observation because the changes manifest themselves within a timescales similar to the duration of a typical hypofractionated treatment.

### 5.1.3. Metabolic signatures indicate increased glycolysis in cancerous cell line

While there is no statistically significant observable metabolic change in the non-cancerous cells as measured by fluorescence lifetime of NADH, a strong shift in the NADH lifetime signature of the cancerous T24 cells clearly manifests itself. The data presented here also show that these changes are not related to mitochondrial metabolism. This evidence includes measurements of cellular ROS and mitochondrial membrane polarization which are not sensitive to radiation. Cellular ROS production remains unchanged in the case of T24 cells. Moreover, the T24 fluorescence of mitochondrial membrane polarization was found to be unchanged following radiation or by the addition of FCCP which decouples ATP production from mitochondrial respiration.

We hypothesize that these changes are related to the increased expression of HIF-1α observed in the cancerous T24 cells that was conspicuously absent in the non-cancerous NOK cells. HIF-1 is a critical protein factor particularly in cancer cells because it has been implicated in therapeutic resistance as well as the role it plays in tumor progression via growth and proliferation as well as angiogenic signaling. Moreover, its upregulation has been implicated in the development of metastatic phenotypes in many cancers. HIF-1 acts as a transcription factor to the hexokinase family of enzymes, as well as glucose transporters which allow for greatly increased glucose turnover not only for energy production, but also for the production and retention of biomass for proliferation.

### 5.1.4. Importance of genotyping cell lines for *in vitro* studies

Our collaborator is in the process of writing a perspective on the importance of genotyping cell lines prior to research studies. It is not uncommon for the identity of a particular cells line to be taken at face value. As we learned in this study, it was very easy to receive a cell line mislabeled as a head and neck cancer cell line and proceed with the work without knowing. Fortunately, for the purposes of this work, which was to assess how metabolic changes manifest differently in response to radiation for a radioresistant and a radiosensitive cell line, the site of the cell lines was not as important as the metabolic findings. After genotyping for identification, and further testing for verification, it was found that the same cell line (T24) was used throughout the entirety of this work. However, in the future, we recommend that genotyping be performed for *in vitro* work.

## 5.2 Future Work

### 5.2.1. Extension of metabolic profiling to various cell lines in-vitro:

This work seeks to explore the changes in metabolism resultant from radiation therapy in an *in vitro* cellular model. However, this work has been limited to the comparison of two head and neck cell lines, one cancerous (T24) and one non-cancerous (NOK). These two models were chosen because they have distinct radiosensitivities where NOK is radiosensitive and T24 is radioresistant. A logical next step would be to evaluate shifts in metabolic profile following irradiation for a battery of cell lines of varying radiosensitivity. In this way, it may be possible to characterize a potential relationship between metabolism and radiosensitivity. This would be an excellent starting point for implementing metabolic profiling for intervention in radiation therapy treatment regimens.

### 5.2.2. Metabolic profiling of radiation response of different primary tumor sites

The cell lines in this work were chosen because they lie on opposite sides of the radiosensitivity spectrum, and also because urothelial cancers may be treated with radiation. As radiation therapy is an important component of head and neck cancer treatments, it would be valuable to perform this study on UM-SCC-22B head and neck cancer cells as the study had originally intended. It would also be interesting to perform similar *in vitro* metabolic and mitochondrial profiling studies on human cell lines derived from other primary tumor sites. It would be particularly interesting to perform these studies on cell lines derived from sites that are not typically treated with radiation therapy. Studies of this nature may provide different avenues into exploring the mechanism underlying contrast in radiosensitivities.

### 5.2.3. Extension of metabolic profiling to 3d culture and animal models:

*In vitro* work with cell lines makes logical sense as a starting point because it cell culture provides a tractable system which allows the separation of metabolism from confounding effects like perfusion or matrix stiffness. However, these advantages that in-vitro work present are also limitations; while cell culture is tractable, it is also unrealistic. Changes in vasculature and fluid pressures have significant impact on the delivery of oxygen and other nutrients, which significantly impacts metabolism.

Extension of metabolic profiling to 3d culture in collagen gels is reasonable as a next step for quantification of metabolism in response to radiation. Changes in matrix stiffness can be simulated by altering collagen density in the gels to examine the effect on metabolism. Moreover, as "tumor microenvironment on a chip" technology becomes more sophisticated, it is possible to build mock blood vessels to simulate metabolite delivery. Therefore, 3d culture on collagen gels may be a viable bridge to animal models.

Finally, extension of metabolic profiling to animal models is a crucial step because animal models allow the observation of the effects of radiation on metabolism in an even more realistic environment. Study of animal models allows for metabolic profiling while the effects of angiogenesis manifest themselves. Moreover, the effects of acute and chronic hypoxia which arise from torturous vasculature on metabolism may be observed and quantified. Clearly, moving towards more realistic models for metabolic profiling is an important step if such profiling were to ever be implemented for therapeutic adaptation.

### 5.2.4. Further exploration of mechanism of radiosensitivity/protection:

It is also important to develop a more robust understanding of the mechanistic underpinnings of the radiosensitivity contrast between different cell lines. As stated previously in this work, HK-II plays a role in cellular protection by preventing apoptotic cell death. A thorough study of HK-II knockdown and its impact on cell survival as a function of radiation dose is needed. A study of this nature would be useful to elucidate the potential role of HK-II in the radiosensitivity signaling cascade. It would also be valuable to explore other targets of the HIF-1 complex in the context of radiosensitivity. Studies which examine the effects of glucose transport enzymes or monocarboxylate transferases inhibition and how they impact radiosensitivity may be tremendously impactful for future targeted intervention.

Finally, an exploration of lactate production following radiation would provide deeper insight into the metabolic changes underlying the changes in NADH lifetime signature. The catalytic cleaving of glucose into two pyruvate molecules is the first step of glycolysis. Pyruvate molecules are then converted to a stoichiometric equivalent of lactate. Exploration of lactate conversion would be further evidence that the NADH lifetime signature observed the radiosensitive cells are indeed due to an induction of the Warburg Effect.

### 5.2.5. Multiscale study of metabolism integrating different modalities:

As shown in this study, metabolic profiling employing NADH FLIM is a powerful tool for investigating changes in cells following irradiation; however, NADH FLIM is not without limitations. Firstly, while NADH is the dominant fluorescence emitter, there is also non-negligible fluorescence emission from NADPH, the phosphorylated form of NADH. These emissions from the NAD(P)H species are very difficult if not impossible to distinguish from each other. Moreover, visible light has very poor penetration depth into tissue because it is heavily scattered.  This property of tissue presents significant challenges with regards to FLIM studies in live animals without endoscopic or window approaches.

Furthermore, while this study explored mitochondrial activity with fluorescence measurements of ROS, polarization and oxygen consumption, these modalities are even more strictly limited to *in vitro* studies.  Therefore, it is necessary to integrate other experimental techniques to advance to *in vivo* studies.  Functional magnetic resonance imaging (fMRI) utilizing hyperpolarized Carbon-13 is a promising method to characterize metabolism on the tissue level because it can be integrated organic molecules in the metabolic chain such as glucose or pyruvate.  Using MR spectroscopy, it is possible to identify the molecule species containing the hyperpolarized Carbon-13 atoms.  In this way, the conversion of glucose to lactate can be quantified, and this can help determine if energy production is indeed from glycolysis.  This allows metabolic profiling at the tissue level.  Positron emission tomography (PET) is another tool which allows for systemic monitoring of a whole animal.  PET imaging with $F^{18}$-2-deoxy-glucose is an extremely powerful tool for localizing metastases clinically because glucose is taken up by tumor sites and thus appear brighter on a PET image.  Monitoring glucose uptake following radiation with PET, and lactate conversion with fMRI could shed light on shifts in metabolic demands and pathways induced by treatment.